A time-slice experiment with the ECHAM4 A-GCM at high resolution: The experimental design and the assessment of climate change as compared to a greenhouse gas experiment with ECHAM4/OPYC at low resolution

Wilhelm May
Danish Meteorological Institute
Lyngbyvej 100
DK-2100 Copenhagen Ø, Denmark
E-mail: may@dmi.dk

DMI Scientific Report 99-2

ISBN 87-7478-389-0
ISSN 0905-3263
ISSN 1399-1949 (ON-LINE)

Abstract

The experimental design of a time-slice experiment, which has been performed with the ECHAM4 A-GCM at a horizontal resolution of T106, is outlined and a description of the external forcing that has been prescribed during the time-slice experiment is given. Further, the climate statistics and the change in climate inferred from the time-slice experiment for a variety of meteorological variables are discussed. In order to investigate, to which extent the assessment of anthropogenic climate change depends on the horizontal resolution of the A-GCM, the results inferred from the time-slice experiment are compared to those obtained from the climate change simulation with the ECHAM4/OPYC coupled model at a horizontal resolution of T42 that has provided the lower boundary forcing for the time-slice experiment.

The time-slice experiment reveals a distinct change in climate caused by the anticipated increase in the atmospheric concentrations of the important greenhouse gases. The assessment of the anthropogenic climate change depends, however, on the horizontal resolution of the A-GCM employed. These differences in the climate change signals, which result mainly from deviations in the simulations of the present-day climate, are due to a different impact of the horizontal resolution on the simulation of the present-day than on the simulation of the future climate, which has been affected by the anticipated increase in the atmospheric concentrations of the important greenhouse gases. The differences in the simulations of the climate for the two periods of the experiments at the different horizontal resolutions, in turn, are related to various causes: firstly, the incorporation of the non-linear interactions with those scales that are not resolved at the low resolution and their impact on the dynamical characteristics of the model, and secondly, the different behaviour of the physical parameterizations at the different resolutions and their local impact on certain meteorological variables such as the near-surface temperature and precipitation and their remote impact on the large-scale circulation. Moreover, the more realistic representation of the topography at the high resolution effects the simulations of a number of processes and phenomena on local as well as on regional scales.

1. Introduction

The possibility of climate change caused by the ongoing rapid increase of various greenhouse gases, with carbon dioxide (CO_2) being considered the most important one, has been intensively investigated over the last decade. Though the question that an overall warming of the earth's atmosphere will take place is widely accepted within the scientific community, there is still some disagreement regarding the magnitude of the change and the question, how long it may take, before the change becomes indisputably noticeable (Houghton et al. 1990; 1996).

A widely used tool to assess the anticipated change in climate caused by the increase of greenhouse gases are global coupled atmosphere-ocean models, where the changes of the concentrations of various greenhouse gases have been prescribed according to typical scenarios provided by the Intergovernmental Panel on Climate Change (IPCC) (e.g., Cubasch et al. 1992; Mitchell et al. 1995). In the early stage this kind of computations aiming at the assessment of the anticipated change in climate included merely the radiative forcing of various greenhouse gases (e.g., Cubasch et al. 1992). Later on they also included the direct radiative effect of aerosols (e.g., Mitchell et al. 1995) or the indirect effect of aerosols by changes in the properties of clouds (e.g., Lohmann and Feichter 1997), but also the changes in the concentration of ozone distinguishing between the stratosphere and the troposphere, where the concentration of this important gas decreases and increases, respectively (e.g., Folland et al. 1998). Recently Roeckner et al. (1998) reported on a computation, where they also had included the tropospheric sulphur cycle into their climate model.

In order to allow for a robust estimate of the anticipated change in climate with its long time scale these global coupled models have to be integrated for several centuries. Due to the practical restrictions associated with the limited computing resources available these climate models typically have a horizontal resolution of about 360 km for the time being. As a result of this rather coarse horizontal resolution a variety of regional aspects of climate cannot be captured by these models. On the other hand there is, however, a strong demand for information about climate on a regional scale from the research community working on the assessment of the (local) impact of the anticipated change in climate on the society as well as on the economy. In order to overcome this dilemma we have performed a so-called time-slice experiment, where a global atmospheric general circulation model (A-GCM) with a horizontal resolution of circa 120 km has been employed. In two simulations of 30 years each, which cover the

present-day climate and the climate at a time when the atmospheric concentration of CO_2 has doubled as compared to the present-day values, the lower boundary forcing has been prescribed as obtained from a climate change simulation performed with a coupled atmosphere-ocean model with a lower horizontal resolution of 360 km.

It is obvious that climate variables such as temperatures near the ground as well as their daily minimum and maximum values or precipitation profit directly from the more realistic presentation of the topography at the high resolution (e.g., Stendel and Roeckner 1998). As a prominent example the precipitation patterns associated with the Indian summer monsoon, which heavily depend on the topography, should be mentioned. Severe weather events, which are regional in extent and, hence, not captured by the low resolution models, are somewhat unexpectedly reasonably well reproduced at a horizontal resolution of about 100 km. Bengtsson et al. (1995), for instance, found that this resolution was fine enough to reproduce both the structure and the frequency of the occurrence of tropical storms realistically. Later on Bengtsson et al. (1996) used data originating from a time-slice experiment to investigate changes in the intensity and the frequency of tropical cyclones in a warmer climate caused by the increase of the greenhouse gases. Different to previous studies (e.g., Broccoli and Manabe 1990) they found that the number of tropical cyclones decreased, in particular in the Southern Hemisphere, and that the strength of these storms was reduced in a warmer climate. Similarly Beersma et al. (1997) used data from the same time-slice experiment in order to investigate another kind of severe weather event, namely extratropical storms in the North Atlantic region. They found an increase of the overall frequency of deep depressions in that area along with a downstream extension of the Atlantic stormtrack in a warmer climate. Rider et al. (1996) went one step further and computed the change in the wave heights in the North Atlantic and North Sea caused by this change in the storminess in the North Atlantic region in a warmer climate. They found an increase of the wave height in the western part of the Atlantic, i.e., in the Bay of Biscay and in the North Sea, but an decrease in most of the rest of the North Atlantic.

The aforementioned studies as the other studies using data originating from a time-slice experiment at high resolution have been severely suffering from the relatively short period of data of about 5 years for each time-slice. Due to the strong natural variability in the atmosphere it is almost impossible to draw any firm conclusion on the change in climate from such a short period of data, in particular if one looks at individual weather events. Therefore Bengtsson et al. (1996) pointed out that their results regarding the decrease in the number of tropical storms

should be taken with some cautiousness. This has also to be seen in the context that the results derived from low resolution climate models have shown an increase in the frequency of tropical cyclones (e.g., Broccoli and Manabe 1990). In this case, however, one has to be aware of the fact that these models do not reproduce the structure of tropical storms reasonably well. With our time-slice experiment covering a period of 30 years for each period we overcome this severe shortcoming, and so we hope that the results to be obtained from it will lead to a number of (at least more) robust conclusions about the future change in climate including those on regional scales.

There is of course a variety of scientific questions that can be addressed on the basis of our time-slice experiment. In this paper, however, I want to focus on a very fundamental aspect of the experiment, that is whether the change in climate inferred from our time-slice experiment differs from the change obtained from the climate change simulation with the coupled atmosphere-ocean model at low horizontal resolution that has provided the lower boundary forcing for the time-slice experiment. This may set the conclusions that have been drawn from various climate change simulations with individual climate models at different resolution into a new perspective and add a valuable contribution to the very important question of the uncertainties of the results inferred from these simulations. My study has been motivated by the fact that the A-GCM employed in the time-slice experiment like other GCMs shows a number of characteristic differences in the statistics of the present-day climate at different horizontal resolutions (Stendel and Roeckner 1998). They found that some of these differences lead to a more realistic simulation of climate at the high resolution of about 120 km than at low resolution compared to the European re-analyses, others to a less realistic presentation of climate. It is, however, essential that the impacts of the horizontal resolution have been inferred for the present-day climate, and it is not known, whether the effects of the horizontal resolution are the same or at least similar for a future climate, which has been affected by the anticipated large increase of greenhouse gases and, hence, may be characterized by a modified pattern of the large-scale circulation. In this case, that is the horizontal resolution has a different influence on the simulation of the future than on the simulation of the present-day climate, the climate change inferred from the simulations at different resolutions will be different.

The paper is organized as follows: In section 2 I describe the models used in the time-slice experiment as well as in the climate change experiment. Subsequently I illustrate the experimental design of our time-slice experiment (section 3) and the external forcing pre-

scribed in the simulations (section 4). In section 5 I discuss the climate statistics and the change in climate inferred from the climate change experiment as well as from the time-slice experiment for a variety of climate variables. A summary and some concluding remarks will follow in section 6.

2. Model description

2.1 Time-slice experiment

The model employed in the time-slice experiment is the ECHAM4 A-GCM (e.g., Roeckner et al. 1996b). The model has been developed at the Max-Planck-Institute (MPI) for Meteorology for simulating the global present-day climate and a possible global change in climate due to enhanced emissions of greenhouse gases. It is based on the global forecasting system that is used at European Centre for Medium-Range Weather Forecasting (ECMWF), but several major changes have been made, in particular to the physical parameterizations in order to make the model suitable for climate simulations. Details on the climate statistics of ECHAM4 in its "standard" configuration with a horizontal resolution of T42 (corresponding to 64×128 gridpoints on a Gaussian grid) and 19 vertical levels can be found in Roeckner et al. (1996a).

In the time-slice experiment we have used ECHAM4 with a horizontal resolution of T106 (corresponding to 160×320 gridpoints on a Gaussian grid) and 19 vertical levels. In ECHAM4 most of the free parameters in the physical parameterizations are independent of resolution (but note they have been selected at a horizontal resolution of T42) instead of tuning the model by choosing an optimal set of parameters at the respective resolution. Only the parameterizations of a few processes, which have turned out to be extremely scale dependent, have been tuned individually at different horizontal resolutions, such as the parameterizations of gravity wave drag, horizontal diffusion or formation of precipitation in stratiform clouds (e.g., Stendel and Roeckner 1998). In consequence the high resolution does not automatically reduce all the systematic model errors, since some of the physical parameterizations, which have been tuned at the lower resolution, are possibly scale dependent. Nevertheless the high resolution leads to a more realistic simulation of the present-day climate by ECHAM4 due to the inclusion of a much wider spectrum of spatial scales and, hence, the non-linear interactions between them and a more realistic representation of the topography (Stendel and Roeckner

1998).

We have performed two simulations with ECHAM4 at the high resolution over a period of 30 years each. These two so-called time-slices have been chosen, so that one 30-year period represents the present-day climate and the other one the climate at a time when the atmospheric concentration of CO_2 has doubled. In each of them the lower boundary forcing has been prescribed as obtained from a climate change simulation performed with a coupled atmosphere-ocean model with low horizontal resolution, which will be further described in the following section. Moreover, the temporal evolution of the concentrations of the important greenhouse gases has been prescribed in the same way as in the climate change simulation (see section 2.2). The data from the time-slice experiment have been saved 4 times daily (00, 06, 12 and 18 UTC), but in order to ensure a proper comparison with the climate change experiment, where the data has been stored twice daily (00 and 12 UTC), I use the data for the time-slice experiment only twice daily for the dynamical meteorological variables, i.e., sea-level pressure as well as temperatures and winds in the free troposphere, but 4 times daily otherwise. For each time-slice a period of simulation of 1.5 years prior to the respective time-slice has been disregarded in order to avoid the spin-up problem.

2.2 Climate change experiment

The climate change experiment has been performed at MPI. The coupled atmosphere-ocean model consists of the ECHAM4 A-GCM at a horizontal resolution of T42 and 19 vertical levels (see section 2.1) and an extension (level 3) of the OPYC ocean model (Oberhuber 1993) including a sea-ice model. OPYC3 has 11 layers and a varying horizontal resolution: poleward of 36° latitude the resolution is identical to that of the low resolution A-GCM, that is circa 2.8°. At low latitudes, the meridional grid spacing is gradually decreased down to 0.5° at the equator in order to allow for a better representation of the equatorial wave guide in the model and, hence, the El Niño/Southern Oscillation (ENSO) phenomenon. Roeckner at al. (1996b) showed that this coupled atmosphere-ocean model actually is able to capture many features of the observed interannual variability of the sea surface temperatures (SSTs) in the tropical Pacific. This includes not only the amplitude, lifetime and frequency of occurrence of El Niño events, but also the phase-locking of the SST-anomalies and the annual cycle. The model components are coupled quasi-synchronously and exchange information once daily.

Annual mean flux-adjustments of heat and freshwater have been estimated from a 100-year spinup of the coupled model. For further details on the coupling technique and the performance of the model I refer to Roeckner at al. 1996b and Bacher et al. 1998.

This coupled model has been used for an control experiment and in the meantime for three different time-dependent forcing experiments, which are thoroughly described in Roeckner et al. (1998). At the time, when we decided to perform our time-slice experiment, only the greenhouse gas experiment covering the period 1860 through 2100 (referred to as "GHG" in Roeckner et al. (1998) and also herein) was available, so that we could only use this particular climate change experiment for extracting the boundary forcing for our time-slice experiment.

In GHG the concentrations of various gases have been prescribed as a function of time: the greenhouse gases CO_2, methane (CH_4), nitrous oxide (N_2O) and several industrial gases such as chlorofluorocarbons (CFC-11, 12, 113, 114, 115), hydrochlorofluorocarbons (HCFC-22, 123, 141b), hydrochlorocarbons (HFC-125, 134a, 152a), carbon tetrachloride (CCl_4) and methylchloroform (CH_3CCl_3). From 1860 to 1990 the annual mean concentrations of these gases have been prescribed as observed and after 1990 according to the scenario IS92a (Houghton et al. 1992). In case of the industrial gases the IS92a-scenario has been updated to be consistent with a "Copenhagen-like" emission scenario (Houghton et al. 1996). This time-dependent or "transient" forcing experiment has been initialized at year 100 of the control run of the coupled model, nominally year 1860 in the transient experiment. In the control run the concentrations of the greenhouse gases (CO_2, CH_4 and N_2O) have been prescribed as observed in 1990 rather than pre-industrial values, and present-day observations have been used for the ocean spinup and for deriving the flux adjustment (Bacher et al. 1998). In consequence the climate in the control run and, hence, the initial state of the transient experiment corresponds to modern rather than the pre-industrial times. Therefore in GHG the initial shift in the concentrations of the greenhouse gases had to be taken into account by enhancing the observed/anticipated concentrations in an appropriate way (see Roeckner at al. (1998) for further details on this procedure).

3. Experimental design

The first period of our time-slice experiment (to be referred to as "TSL-1") covering the

years 1970 to 1999 represents the present-day climate, whereas the second period ("TSL-2") including the years 2060 to 2089 represents the climate at a time when the atmospheric concentration of CO_2 has doubled compared to the present-day values.

In the time-slice experiment we have prescribed the lower boundary forcing, namely the SSTs, the sea-ice extent (i.e. the fraction of a grid box covered by sea-ice) and sea-ice thickness as obtained from the transient climate change experiment GHG for the corresponding periods (to be referred to as "GHG-1" and "GHG-2", respectively). Different to most of the previous time-slice experiments (e.g., Bengtsson et al. 1996) we have prescribed the actual monthly mean values of these variables instead of fixed annual cycles. By that we are not only able to retain the transient character of GHG, but also to include interannual variations of the lower boundary forcing, such as the variations of the SSTs in the tropical Pacific associated with the ENSO phenomenon into the simulations. Hence our time-slice experiment is characterized by a very realistic level of the internal variability inherent in the climate system. Moreover, our experiment takes the possible changes in the characteristics of the ENSO phenomenon (i.e. the amplitude, lifetime and frequency of occurrence of El Niño and La Niña events) in the anticipated future climate into account (see following section). In addition to the lower boundary forcing we have prescribed the concentrations os the greenhouse gases (CO_2, CH_4 and N_2O) and of various industrial gases in the same way as in GHG (see preceding section).

The low resolution of the coupled experiment of about 360 km allows only for a rather coarse representation of the geographical details in the climate change experiment. Although the land-sea mask used in the coupled model (Fig. 1a) shows the 6 continents unambiguously, the representation of the continental coast lines is rather unrealistic as compared to the high resolution of around 120 km (Fig. 1b), and a number of islands is missing. Moreover, the land-sea mask in the coupled model has been modified in order to allow for the exchange of water masses between the smaller and the larger ocean basins (Fig. 1a). The Iberian peninsula and Denmark/Northern Germany, for instance, have been removed to connect the Mediterranean and the Baltic Sea, respectively, with the Atlantic ocean. Furthermore, the large lakes such as the Caspian Sea or the Great Lakes in North America have been transformed into land areas, since the coupled model does not include a special lake model. In the time-slice experiment we also have transformed the big lakes into land areas for the purpose of consistency as indicated by the black areas in the land-sea mask used in the time-slice experiment (Fig. 1b).

In order to prescribe the boundary forcing in the time-slice experiment the SSTs and the sea-ice data had to be interpolated to the appropriate grid, that is the Gaussian grid associated with the horizontal resolution of T106. This has been done for all the grid points, where the land-areas of the coupled and the time-slice experiment shown in Figure 1a and Figure 1b, respectively, do not overlap. These areas are marked in white and black in Figure 1c.

To avoid inconsistencies between the state of the ocean and the land surface in the beginning of our time-slices we have initialized the parameters describing the soil processes in ECHAM4 (DKRZ 1992) with values obtained from GHG for the particular starting points of the simulations, that are July 1st in the nominal years 1968 and 2058, respectively. These parameters are the surface temperature, the snow temperature, the temperatures in the 5 different soil layers and the soil wetness. As for the parameters describing the ocean surface, the parameters describing the land surface had to be interpolated on the appropriate grid, but in this case the differences in the elevation had to be taken into account. That has been done for all points, where the two land-sea masks do overlap (indicated in grey in Figure 1c). For the other land points (marked in black in Figure 1c) the instantaneous values consistent with the atmospheric initial condition have been used.

In order to investigate, how the soil temperatures develop in the start of the simulations, I take a look at the temporal evolution of the soil temperatures in 5 different regions (Fig. 2). These regions have been chosen in order to represent different climate zones in different parts of the world and not to be affected by complex terrain. Figure 3 shows the temporal evolution of the soil temperature in a layer 6.5 cm below the surface (layer 2) and in the deepest layer more than 6 m below the surface (layer 5) in these regions for the first month of simulation of the first time-slice (July 1968). The values are given 4 times daily, and the initial values are marked by the dots. According to this, the temperatures in the upper layer exhibit a pronounced diurnal cycle and in most of the regions variations on intraseasonal timescales, but stay rather close to the initial values. Only in northeastern South America do the temperatures reveal an upward trend presumably due to the increase of the air temperatures near the ground typically occurring in this area during July (e.g., May et al. 1992). Not surprisingly the deep soil temperatures do not change in the course of the first month. In some areas, i.e., southwestern Australia and northwestern South America the temperatures in the deep layer reveal the tendency to rise relatively strong in the first two years of the simulation (Fig. 4), before a weaker positive trend associated with the steady rise of the air temperatures due to the

enhanced concentrations of the greenhouse gases can be seen. These examples show very nicely that by initializing the land surface in the time-slice experiment properly we are actually able to almost totally avoid an imbalance between the state of the ocean and the land surface and, hence, to prevent the spin-up problem for the land surface.

4. External forcing

In the time-slice experiment we have prescribed the SSTs, the sea-ice extent and the sea-ice thickness at the lower boundary as the external forcing (see previous section). In this section I therefore discuss the characteristics of these variables describing the state of the ocean surface.

Figure 5 shows the global distributions of the 30-year annual mean SSTs for the two time-slices TSL-1 and TSL-2 and Figure 6 the difference between the two. Those areas that are covered by sea-ice for an extensive part of the year are marked by the light shading. According to this, the distributions of the SSTs reveal a rather similar spatial structure during the two time-slices with a general tendency of higher temperatures in the range of several °C in TSL-2. Due to the effect of the sea-ice, the warming of the SSTs around Antarctica is much weaker than further north, so that the meridional SST gradients in the zonal band between 45 and 50° S in the ocean basins in the Southern Hemisphere are considerably sharper in TSL-2. The geographical distribution of the differences, which reveals a rich spatial structure, actually indicates a cooling of the SSTs around Antarctica in the regions southeast of South America and south of Australia, which is associated with the increase of the sea-ice extent in these areas in TSL-2 (see Fig. 14). Moreover, the warming is not symmetric for the two hemispheres: in the Northern Hemisphere the SSTs generally increase by more than 2 °C and in the Southern Hemisphere by less than 2 °C. The strongest warming (exceeding 3 °C) occurs in the North Pacific north of 45° N and in the North Atlantic in the region east of Labrador and in the areas north of 70° N. Between southern Greenland and Iceland the warming is reduced to values of about 1.5 °C, and the warming is relatively weak in the Norwegian Sea. This could be related to the efficient vertical mixing and, hence, large effective heat capacity of the ocean in these areas, which may even lead to the slight cooling in the southern oceans around Antarctica (e.g., Manabe et al. 1991). Relatively strong warming (circa 2.5 °C), on the other hand, also occurs in the eastern tropical Pacific, in the area southeast of South Africa and in the Tasmanian Sea.

I don’t want to compare the annual mean SSTs for the first time-slice with the observed SSTs s for the last 30 years here, but rather comment on the quality of the coupled model from a more general point of view. Due to the flux-adjustment (see section 2.2) the differences between the annual mean SSTs simulated by the coupled model (i.e., in the control run) and the observed values are generally smaller than 1 °C. Larger errors, however, occur in the regions of the western boundary currents, which are not sufficiently resolved by the ocean model. These large errors are confined to small areas and, hence, are not having a significant impact on the atmospheric climate statistics (Roeckner at al. 1996b). This is not only the case for the global mean values, but also for the regional distributions of various climate variables. But since the annual cycle is not modified by the flux-adjustment, the errors in the SSTs are larger for different seasons than for the annual mean values with, again, largest errors in the regions of the western boundary currents. During boreal winter, for example, individual gridpoints off Newfoundland and Japan show maximum errors of up to 5 °C.

Due to the transient character of the time-slice experiment (see section 3), the SSTs undergo interannual variations as well as variations on the very long timescales of the anticipated change in the concentrations of the important greenhouse gases. In Figure 7 I therefore show the linear trends of the SSTs within each period of the time-slice experiment. According to this, the SSTs reveal a general warming trend during both periods except for the high southern latitudes, where we find a cooling trend. In particular in TSL-2 a cooling of more than 1.5 °C over a period of 90 years occurs in the most southern part of the South Pacific. During this period also the South Pacific cools down in the area west of South America, whereas in TSL-1 the SSTs in the region west of North America cool off by approximately 0.5 °C. The warming trend is rather strong (circa 2 °C) in the western half of the North Pacific, and also in the region east of Labrador and in the Norwegian Sea with a much weaker warming between southern Greenland and Iceland. In TSL-2 a very strong warming trend of up to 6 °C over 90 years occurs in the eastern tropical Pacific, while in TSL-1 the SSTs in this area warm by about 2 °C.

The geographical distributions of the linear trends in the two time-slices are very similar (i.e., the pattern correlation is about 0.86 for each period) to the distribution of the difference between them (Fig. 6), indicating that for the SSTs the response to the increase of the atmospheric concentrations of the greenhouse gases is very consistent throughout the course of the transient climate change simulation GHG. Timmermann et al. (1999) found, for instance, a warming trend of the SSTs in the eastern tropical Pacific by 1.8 °C per century over the entire

240 years of simulation for GHG. They explained this warming trend, which resembles “permanent” El Niño conditions, by the cloud-albedo feedback leading to a differential surface warming centred in the equatorial eastern Pacific (e.g., Meehl and Washington 1996).

Very large interannual variations of the SSTs in both time-slices (Fig. 8) occur in the eastern tropical Pacific in association with ENSO. In the second time-slice the variations of the SSTs in this area are larger than in the first one with a maximum standard deviation of approximately 1.8 and 1 °C, respectively. Compared to observations, however, the maxima of variability are shifted westward by about 20° longitude leading to a substantial underestimation of the variations of the SSTs from year to year near the South American coast (see Timmermann et al. 1998). Other areas with strong interannual variations of the SSTs are the region off Newfoundland and some regions near the edge of the sea-ice, in particular for the North Atlantic and the South Pacific. The fluctuations of the SSTs in these regions are accompanied by short-term climate variations both in the particular regions and in remote areas (e.g., May and Bengtsson (1998) and references therein for the tropical Pacific and, e.g., Palmer and Sun (1985) for the northwest Atlantic), so that we can expect a realistic level of atmospheric interannual variability in the time-slice experiment.

In the following I take a look at time series of the annual mean SST-anomalies in different areas in the equatorial Pacific and the extratropical North Atlantic and North Pacific. In the case of the tropical Pacific I distinguish between an area off the South American coast (“Niño 1+2”: EQ-10° S, 90-80° W), the eastern (“Niño 3”: 5° N-5° S, 150-90° W) and the western half of the equatorial Pacific (“Niño 4”: 5° N-5° S, 160° E-150° W) and an area covering the central tropical Pacific (“Niño 3.4”: 5° N-5° S, 170-120° W). In both time-slices the SSTs in all the different areas vary considerably from year to year (Fig. 9). The fluctuations are stronger in the eastern than in western half of the equatorial Pacific. They are rather small near the South American coast except for the second half of the second time-slice (from approximately the year 2074), when we find SST-anomalies of up to 2 °C in Niño 1+2. Moreover, the variations are generally stronger in TSL-2 than in TSL-1. These characteristics can also be seen from Table 1, which contains the standard deviations of the individual annual mean SST-anomalies in the different regions. Here we can clearly see that the differences between the two time-slices regarding the interannual variability are much more pronounced in the eastern than in the western half of the equatorial Pacific. In Niño 1+2, for instance, the standard deviation is more than twice as large in TSL-2, whereas it is only increased by about 20% in Niño 3 and

Niño 3.4. Another interesting feature is the enhanced frequency of strong La Niña events in TSL-2 with negative SST-anomalies of up to 3 °C in Niño 3 (Fig. 9), while in TSL-1 strong cold ENSO-events occur considerably less frequently. According to Timmermann et al. (1999), this change in the statistics of ENSO events is typical for the first and the second half of GHG and not only for the two periods of the time-slice experiment. In order to obtain the time series shown before I have removed a linear trend from the data. In all the different areas a warming trend actually occurs in both time-slices (Tab. 1). The trends are generally stronger in TSL-2 than in TSL-1, especially in the eastern half of the tropical Pacific. In Niño 1+2, for instance, the trend has more than doubled in TSL-2, but in Niño 3 and Niño 3.4 it is only enhanced by about 10%. It is interesting to note, how closely the changes in the trends, that is in the mean state of the ocean are related to changes in the interannual variability, that is in the occurrence of ENSO events. That is the stronger the warming trend and, hence, the higher the mean SSTs are, the stronger are also the interannual variations of the SSTs.

In the extratropics I concentrate on two areas in the North Pacific (25-45° N, 175° E-140° W) and in the North Atlantic (40-60° N, 40-20° W), where pronounced variations of the SSTs typically occur (e.g., Lau and Nath (1994) for the North Pacific and, e.g., Deser and Blackmon (1993) for the North Atlantic). The SSTs vary to the same extent from year to year in the Pacific and the Atlantic (Fig. 10, Tab. 1). Moreover, the magnitude of the interannual variability is about the same in both time-slices. Only in the end of TSL-1 SST-anomalies reach values of up to 1 °C, in the North Atlantic, whereas the anomalies typically have a magnitude of 0.5 °C otherwise. There is a general warming trend in these areas in both time-slices (Tab. 1), which is almost doubled in TSL-2 in the North Atlantic, but reduced by about 20% in the North Pacific. Apparently the general enhancement of the trend in the second time-slice due to the stronger increase of the concentrations of the greenhouse gases in this period is counteracted by different kinds of processes such as a change in the atmospheric general circulation. This change is presumably associated with the El Niño-like strengthening of the trend of the SSTs in the equatorial Pacific (Fig. 7) leading to a relative cooling of the SSTs in the North Pacific (e.g., Lau and Nath 1994). In addition to the interannual variations, fluctuations on longer time scales of several (up to 10) years with an amplitude of several tenth of a °C are visible in the time series for the North Atlantic as well as for the North Pacific.

I now take a look at another parameter describing the state of the ocean surface, namely the sea-ice extent. Figure 11 shows the sea-ice extent in boreal winter (January to March) for

the two time-slices. I have marked those areas that are covered by sea-ice in all years by the dark shading, those areas that are covered more than half of the time but not permanently by the medium shading and those areas that are covered at least in one year but not more than half of the time by the light shading. According to this, the extension of the Arctic ice-shield is considerably smaller in the second time-slice than in the first one due to the warming in the Arctic oceans associated with the increased concentrations of the greenhouse gases (see Fig. 6). In TSL-1, for instance, the Tjukter Sea, the Hudson Bay and the Kara Sea are covered in all years with ice, whereas in TSL-2 these areas area covered only part of the time with ice. Further, large parts of the Baltic Sea and the Sea of Okhotsk are frequently ice-covered in the first, but not in the second time-slice. This can also be seen from Figure 12, which shows the differences between the two time-slices with respect to the permanent and the occasional (more than 50% of the time) coverage with sea-ice in boreal winter. The dark shading indicates the areas, where the sea-ice has vanished in TSL-2, the light shading the areas with additional sea-ice in TSL-2. We can clearly recognize the decline of the Arctic ice-sheet on all sides in the second time-slice and the disappearance of sea-ice in the Baltic and the Kara Sea. In austral winter (July to September) the Arctic ice-shield has declined in TSL-2 (Fig. 14) to such an extent that some areas close to the North Pole are not covered permanently with sea-ice any more (Fig. 13).

In the very high latitudes of the Southern Hemisphere, however, we do not notice such a drastic decline of the sea-ice extent associated with the general warming trend (Figs. 11, 13). In austral winter, when the extension of sea-ice is largest, sea-ice occurs in TSL-2 in the Weddell Sea, the area south of Australia and the Ross Sea in all years, whereas in TSL-1 these regions are only occasionally covered with ice (Fig. 14). This increase in the extension of the sea-ice in the second time-slice is associated with cooler SSTs in the areas located further north (Fig. 6). In other regions such as the area southwest of South America and the area southeast of Africa the sea-ice extent is reduced in TSL-2.

5. Climate statistics

In the following section I describe the climate statistics obtained from the time-slice experiment and compare them to the statistics based on the greenhouse gas experiment, that is the climate change simulation at low resolution for the corresponding periods. This includes a variety of meteorological variables such as pressure, temperature, wind or precipitation, and I

will discuss the geographical distributions as well as the zonal or global mean values. I will concentrate on the boreal winter season and present mean values for the period December to February for pressure, temperature and wind and annual mean values for screen temperature and daily precipitation.

5.1 Sea-level pressure

I first take a look at the sea-level pressure, a meteorological variable that comprises information on both the dynamical state and the thermal structure of the atmosphere. Figure 15 shows the geographical distributions of the seasonal mean sea-level pressure for the two time-slices TSL-1 (Fig. 15a) and TSL-2 (Fig. 15b) and also the differences between these two periods (Fig. 15c). These differences indicate the change in the sea-level pressure associated with the changes in the general circulation caused by the increase in the atmospheric concentrations of the important greenhouse gases. In addition to the differences themselves their significance at a certain level (see the respective figure captions) is indicated by the shading. Positive significant differences are indicated by the dark, negative ones by the light shading. The significance has been obtained via a two-sided t-test (e.g., Essenwanger 1986). In addition I present the zonal mean values for each time-slice (Fig. 15d). In this case the significance of the differences between the zonal mean values for the two periods is indicated by the bars at the bottom of the respective figure.

During both periods we see the typical distributions of low- and high-pressure areas (Figs. 15a, b). Areas with very low pressure are the Aleutian low over the northern Pacific and the Icelandic low centred between Greenland and Iceland and extending further downstream over the northern Atlantic. In the Southern Hemisphere areas with very low pressure can be found near Antarctica with two centres located southeast of South America and south of Africa. High-pressure areas, on the other hand, are located over the ocean basins of the Southern Hemisphere between 20 and 40° S and over the continents in the Northern Hemisphere extratropics, i.e., the United States (US), southwestern Europe and the Asian part of Russia. In the future climate the pressure is decreased over most of the Northern Hemisphere, in particular north of 50° N, whereas the pressure is increased in the zone between 40 and 70° S (Figs. 15c, d). As a consequence, the meridional pressure gradient in the Northern Hemisphere extratropics is considerably stronger in TSL-2, whereas in the Southern Hemisphere extratropics the

strength of the meridional pressure gradient is unchanged, but the location of the strongest gradient is shifted slightly poleward. As for the local change of pressure, we find, for instance, an intensification and a downstream extension of the Icelandic low in the future climate, whereas the Aleutian low is virtually unchanged. The changes in the pressure over the northern Atlantic lead to an intensification of the North Atlantic Oscillation (NAO) (e.g., Hurrell 1995). In the Southern Hemisphere the centres of high pressure over the ocean basins are extending somewhat further poleward in the future climate.

Figure 16 shows the distributions of the seasonal mean values of the sea-level pressure for the two periods as obtained from the greenhouse gas experiment at low resolution. In this case the distributions of the seasonal mean sea-level pressure (Figs. 16a, b) show the same general structure as in the time-slice experiment (Figs. 15a, b), that are high- and low-pressure centres in the same locations. There are, however, some differences with respect to the magnitude. These can be seen from Figure 17, where the differences between the time-slice and the greenhouse gas experiment for the two periods of simulation are given. The significance of the differences at a certain level (see the respective figure captions) according to a two-sided t-test is indicated by the shading. In addition I present the zonal mean values for each of the experiments for the two periods (Figs. 17b, d). In this case the significance of the differences between the zonal mean values for the two experiments is indicated by the bars at the bottom of the respective figures.

The Aleutian and the Icelandic low, for instance, are about 4 hPa stronger in TSL than in GHG during both periods (Figs. 17a, c), so that during the first period, which represents the present-day climate, the time-slice experiment is closer to observational data (Stendel and Roeckner 1998). Another characteristic difference between the two experiments are lower values of the pressure north of about 50° N in TSL during both periods (Figs. 17b, d), which is related to the fact that at the high horizontal resolution the extratropical cyclones tend to travel further downstream than at the low resolution. Also by this the time-slice experiment is closer to observational data than the greenhouse gas experiment (Stendel and Roeckner 1998). A shortcoming of the model at high resolution is, however, the zonal orientation of the flow over the eastern Atlantic and Europe (Figs. 15a, b), since the cyclones tend to continue to travel eastward instead of taking a northeastern route in the exit region of the Atlantic stormtrack. This effect can also be observed at the low resolution, but is not as severe (Figs. 16a, b). In the Southern Hemisphere the main difference between the two experiments is that in TSL the areas

with high pressure in the midlatitudes are extending further poleward (Figs. 17b, d).

The climate change signal obtained from the greenhouse gas experiment (Fig. 16c) reveals the same general structure as the signal we have found in the time-slice experiment (Fig. 15c), but the changes in the seasonal mean sea-level pressure appear to be stronger in GHG than in TSL over most of the globe. In the Atlantic/European region, for instance, the intensification of the NAO is about twice as large (circa 6 vs. 3 hPa), since both the decrease of the pressure over Iceland and the increase in the area west of the Iberian peninsula are more pronounced. Furthermore, the greenhouse gas experiment shows also an intensification of the Aleutian low in the future climate, while we don't find a change in the intensity of the Aleutian low in the time-slice experiment. In the area to the southeast of the Aleutian low the pressure is increased leading to a strengthening of the meridional pressure gradient over the eastern extra-tropical Pacific.

The climate change signals obtained from the two experiments (Fig. 18) reveal not only the aforementioned difference in the Atlantic/European area, but quite substantial departures in several areas, which occasionally have about the same magnitude as the climate change signals themselves. Relatively large differences appear, for instance, in the Northern Hemisphere extratropics exhibiting a wave-like pattern with zonal wave number 3 with considerable positive differences near the Aleutians, over eastern Canada and over Russia (Fig. 18a). In the areas further south, i.e., over the Pacific and the Atlantic basin between 30 and 50° N there are negative differences. These differences are related to the fact that both the reduction of the pressure near the Aleutians, over eastern Canada and over Russia and its increase over the Pacific and the Atlantic are more pronounced in GHG than in TSL.

Another area with considerable differences between the climate change signals is the zone between 40 and 60° S, where the intensification of the high-pressure systems in the future climate is less pronounced in TSL than in GHG (Fig. 18a). Furthermore, the area with the largest increases of the sea-level pressure is located about 5° further south in TSL (Fig. 18b). Different to the Northern Hemisphere the differences between the climate change signals are mainly zonally symmetric in the Southern Hemisphere extratropics, reflecting the importance of the stationary waves for the large-scale flow in the Northern Hemisphere extratropics.

A third area with significant differences is the tropical belt, where we find a wave-like pattern with zonal wave number 2 with positive deviations over the Atlantic and Indonesia and

negative ones over the Pacific and the Indian Ocean (Fig. 18a). These differences reflect mainly the climate change signal in the tropics that we have found in the greenhouse gas (Fig. 16c), which, however, is not visible in the time-slice experiment (Fig 15c).

The differences between the climate change signals obtained from the two experiments (see Figures 15c and 16c, respectively) reflect also the differences between the systematic deviations of the model at the different horizontal resolutions for the simulations of the future and the present-day climate, which are shown in Figures 17c and 17a, respectively. This can be written as

$$DIFF = (TSL_2 - TSL_1) - (GHG_2 - GHG_1) = (TSL_2 - GHG_2) - (TSL_1 - GHG_1)$$

Hence, the differences between the climate change signals, which I have described above, can also be interpreted as follows: The systematic differences between the time-slice and the greenhouse gas experiment in the Northern Hemisphere extratropics, which are characterized by lower sea-level pressure at the high latitudes and higher pressure in the areas further south, in particular over the Pacific and the Atlantic in TSL during both periods, are considerably smaller for the future than for the present-day climate (Figs. 17a, c). Apparently the simulation of the large-scale circulation in the Northern Hemisphere extratropics in the future climate, which is characterized by a strengthening of the zonal compared to the meridional component of the large-scale flow, does not depend as much on the resolution of the model as the simulation of the present-day climate. This appears also to be the case in the Southern Hemisphere extratropics, where the future climate is characterized by a strengthening of the meridional pressure gradient and stronger westerly winds at about 60° S. In the tropics, however, the differences between the climate change signals are primarily related to the systematic differences for the future climate as simulated by the two models (Fig. 17c) rather than for the simulations of the present-day climate (Fig. 17a).

Despite the differences described in the preceding paragraphs the climate change signals as derived from the two experiments reveal by and large the same structure, but the signal obtained from TSL is typically weaker than the signal in GHG. This can also be see from Figure 19, which shows the ratio of the climate change signals in the two experiments

$$RAT = (TSL_2 - TSL_1) / (GHG_2 - GHG_1)$$

For the seasonal mean sea-level pressure the ratio is positive over most of the globe, indicating that the climate change signals obtained from the two experiments have the same sign (Fig. 19a). But in most of these regions the values of the ratio are smaller than 1, indicating a weaker signal in TSL. We find also some areas with a negative ratio, meaning that the two climate change signals have opposite signs. This is, for instance, the area of the Azores high in the Atlantic/European region, but also the areas over the extratropical and the eastern tropical Pacific. As for the zonal mean values, the climate change signals have the same signs (as indicated by positive values of the ratio) at almost all latitudes, but opposite signs at about 30° S and at the edge of Antarctica (Fig. 19b).

5.2 Temperature

In the following I take a look at the temperature in the troposphere and stratosphere. This includes both the zonal mean values as a function of latitude and height and the geographical distribution in the lower troposphere, i.e., at 850 hPa.

5.2.1 Zonal mean crossection

Figure 20 shows the crossections of the zonal mean values of the seasonal mean temperature for the two time-slices TSL-1 (Fig. 20a) and TSL-2 (Fig. 20b) and the differences between the two (Fig. 20c). According to this, the increase of the concentrations of the important greenhouse gases leads to a warming in the troposphere and to a cooling in the stratosphere. The maximum warming can be found in the tropical upper troposphere and in the Arctic region, especially in the lower part of the troposphere. As a consequence, the meridional temperature gradient within the lower troposphere of the Northern Hemisphere is considerable weaker in the future (Fig. 20b) than in the present-day climate (Fig. 20a), whereas above 300 hPa the meridional temperature gradient is strengthened in both hemispheres in the future climate. These features are typical for transient climate change simulations, with or without the effect of aerosols included (e.g., Mitchell and Johns 1997).

The greenhouse gas experiment shows the same general structure of the changes in the zonal mean temperatures associated with the enhancement of the atmospheric concentrations of the greenhouse gases (Fig. 21). As the most obvious differences to the time-slice experiment

we find, however, a stronger warming in the tropical upper troposphere and a stronger cooling in the extratropical stratosphere in both hemispheres. Moreover, the warming in the Arctic region is weaker than in TSL. A closer look at the differences between the climate change signals obtained from the two experiments reveals a more detailed structure (Fig. 22c). At the high latitudes, for instance, the warming as obtained from the time-slice experiment is relatively strong throughout the troposphere, whereas the cooling in the stratosphere is not as pronounced. In the tropics and most of the extratropics, i.e., between 60° S and 70° N the warming is relatively weak in TSL at almost all heights shown, and the differences are most pronounced just above 100 hPa. An interesting feature appears in the lower troposphere of the Northern Hemisphere extratropics. South of 70° N the warming is stronger in GHG, but further north it is stronger in TSL (see section 5.2.2).

These differences in the climate change signals due to the different horizontal resolutions of ECHAM4 are, however, small compared to the differences in the climate change signals due to the effects of aerosols (both the direct and the indirect effects) and of the changes in the tropospheric ozone concentration (Roeckner et al. 1998). It is interesting to note that the impact of these effects on the climate change signals, that is a weaker warming in the troposphere and a stronger warming in the stratosphere, particularly in the extratropics, is rather similar to the impact of the horizontal resolution. The only major difference is the relatively weak warming of the tropospheric temperatures at the high latitudes due to the effects of aerosols, while the high horizontal resolution leads to a stronger warming in these areas.

As mentioned above, the differences in the climate change signals correspond to the differences between the systematic deviations of the two experiments for the two periods representing the future (Fig. 22b) and the present-day climate (Fig. 22a). During both periods the zonal mean values of the temperatures are higher in TSL than in GHG for most latitudes and levels except for the lower part of the troposphere in the zone between 10 and 60° S and the middle troposphere in the equatorial belt. Also near 100 hPa centred at about 30° S and 30° N, respectively, the time-slice experiment is characterized by lower temperatures, since the area with the lowest temperatures in the tropical stratosphere is extending further poleward than in GHG. The largest positive differences representing higher temperatures in TSL occur at about 300 hPa in the extratropics and in the lower parts of the troposphere in the Antarctic region as well as at the high northern latitudes, i.e., north of about 50° N. At the high latitudes the systematic deviations between the two experiments are larger in the simulations of the future cli-

mate than for the present-day climate within the troposphere, whereas in the areas between 60° S and 70° N the systematic deviations are more pronounced for the present-day climate at all levels. In particular in the lower part of the troposphere of the Northern Hemisphere extratropics the relatively large deviations in the simulations of the present-day climate lead to significant differences between the climate change signals in this area (Fig. 22c).

5.2.2 Geographical distribution

Figure 23 shows the geographical distributions of the seasonal mean temperatures in the lower troposphere, i.e., at 850 hPa, as obtained from the time-slice experiment. Different to the sea-level pressure (Fig. 15), in this case I also present the geographical distribution of the climate change signal with the zonal mean values removed (Fig. 23d). This part of the climate change signal reflects to a large extent the temperature changes caused by changes in the activity of the stationary waves. Apparently the enhancement of the atmospheric concentrations of the greenhouse gases leads to a significant warming over the entire globe (Fig. 23c). The strongest warming occurs in the Northern Hemisphere with a change of circa 5 °C in the zonal mean values north of 50° N and the weakest near Antarctica with a change of about 1.5 °C in the zonal mean values (Fig. 23e). The distributions reveal a contrast between the oceans and the land masses in the Northern Hemisphere extratropics, since the warming is relatively strong over the continents, in particular over the Asian part of Russia and relatively weak over the Atlantic and the Pacific (Fig. 23d). Other areas with rather strong warming are located over Australia, South America and the eastern tropical Pacific, the subtropical parts of Africa and the Atlantic or the Arabian peninsula. This feature, together with the general warming trend, is typical for transient climate change simulations and occurs with and without the effects of aerosols included (e.g., Houghton et al. 1996).

The greenhouse gas experiment (Fig. 24) shows by and large the same structure of the warming in the future climate than the time-slice experiment. A closer look at the climate change signals derived from the two experiments, however, reveals a number of differences. The relatively strong warming over northeastern Asia is, for instance, much stronger in the climate change simulation at the low resolution, and the relatively weak warming over the northern Atlantic and over the northeastern extratropical Pacific is more pronounced (Fig. 25). As a consequence the contrast between the ocean and the land areas with regard to the warming in

the Northern Hemsiphere extratropics is stronger in GHG than in TSL. In the Southern Hemisphere, on the other hand, we find a stronger warming in the greenhouse gas experiment north of about 50° S, but a weaker increase of the temperatures further south. Relatively strong differences occur in the regions southeast of South America and South Africa and south of Australia.

The stronger warming over northeastern Asia in the greenhouse gas experiment is related to the stronger change in the cyclone activity at the high latitudes in the climate change simulation at low resolution, which we have seen in the sea-level pressure field (see Fig. 18). Furthermore, the cyclone activity over northern parts of Europe and Asia is generally stronger in the high resolution model than at low resolution (see Fig. 17), leading to higher temperatures in the time-slice than in the greenhouse gas experiment in these regions during both periods of simulation (Fig. 26). But the differences between the two experiments are up to 1.5 °C larger for the simulations of the present-day climate. The relatively weak warming over the ocean basins in the greenhouse gas experiment, on the other hand, is related to a stronger change in the meridional, in this case southerly component of the large-scale flow in these areas. Especially for the present-day climate, the relatively strong northerly transports of sensible heat lead to higher temperatures over the northern Atlantic as well as over the northeastern Pacific in GHG.

5.3 Zonal wind component

As for the temperature, I investigate both the zonal mean values as a function of latitude and height and the geographical distributions of the zonal wind component. In this case we, however, take a look at the geographical distribution in the lower as well as in the upper troposphere, i.e., at 850 and 200 hPa.

5.3.1 Zonal mean crossection

The crossections of the seasonal mean wind component as obtained from the time-slice experiment (Fig. 27) reveal a considerable increase of the zonal wind speed in the upper troposphere and the stratosphere in the future climate. These changes in the wind field are related to the strengthening of the meridional temperature gradient at these levels (see Fig. 20c). As a

consequence, the jet streams are intensified, and the areas with relatively strong westerly winds are extending further upward. Within the middle and the lower troposphere we find an enhancement of the prevailing westerly winds in the subtropics as well as in parts of the extratropical regions in the zones between 55 and 75° S and between 50 and 70° N, respectively, while in the tropics the prevailing easterly winds (up to about 400 hPa) are strengthened in the future climate. In the other parts of the extratropical regions, namely in the zones between 40 and 55° S and between 30 and 50° N, respectively, the westerly winds are reduced.

The changes in the zonal mean wind component as inferred from the greenhouse gas experiment (Fig. 28) have the same general structure as the changes obtained from the time-slice experiment, but also some differences with respect to both the magnitude and the exact location of the changes. In the stratosphere, for instance, the enhancement of the westerly winds is considerably stronger in GHG, since the strengthening of the meridional temperature gradient is more pronounced (see Fig. 21). The enhancement of the westerly winds in the Southern Hemisphere extratropics and the poleward shift of the latitudes, where the strongest westerly winds occur, is relatively strong in GHG accounted for by the relatively strong increase of the meridional temperature gradient in this area. In addition, the strengthening of the westerly winds takes place south of about 51° S as compared to 56° S in the time-slice experiment. A direct look at the differences between the two experiments (Fig. 29) reveals these differences quite clearly. In the Southern Hemisphere extratropics, for instance, the difference between the climate change signals (Fig. 29c) shows a cell-like structure with rather strong positive differences in the zone between 30 and 50° S and negative differences further south, i.e., between 50 and 75° S. These deviations come mainly from the differences in the simulations of the present-day climate in the Southern Hemisphere extratropics (Fig. 29a). Only for the present-day climate the westerly winds as simulated at the high horizontal resolution are relatively strong on the poleward side of the jet stream and relatively weak on the equatorward side. The difference in the tropical stratosphere, on the other hand, is mainly accounted for by larger differences in the simulations of the future climate (Fig. 29b), when the westerly winds penetrate further upward into the stratosphere in GHG. In the Northern Hemisphere extratropics the differences in the climate change signals obtained from the two experiments are rather small, but in general the differences between the simulations of the present-day climate are somewhat stronger than the differences for the future climate.

5.3.2 Geographical distribution

The geographical distributions of the seasonal mean zonal wind component at 850 hPa as obtained from the time-slice experiment (Fig. 30) reveal a slight poleward shift of the areas with westerly winds in the extratropical regions of both hemispheres in the future climate. At the same time the easterly winds in the tropics are generally reduced. The greenhouse gas experiment (Fig. 31) shows in general the same change between the future and the present-day climate, but the changes are typically larger than in the time-slice experiment. In particular over the North Atlantic and northern Europe is the intensification of the westerly winds more pronounced than in TSL, as well as the reduction of the westerly winds over the southern North Atlantic and southern Europe is. These differences are related to the larger change in the sea-level pressure field, which I have discussed in further detail in section 5.1. In the Southern Hemisphere extratropics the poleward shift of the zone with the maximum westerly winds in the lower troposphere is stronger in GHG, and also the maximum values of the wind speed are relatively large in the greenhouse gas experiment.

This can clearly be seen from Figure 32, where the differences between the climate change signals derived from the two experiments are given. The zonal mean values (Fig. 32b) show, for instance, quite clearly that the change in the zonal wind component in the Southern Hemisphere extratropics, i.e., the reduction of the westerly winds in the zone between 30 and 55° S and the intensification between 55 and 75° S, is weaker in the time-slice experiment. Moreover, the strongest changes in the zonal wind component occur further poleward than in the greenhouse gas experiment, which is also the case in the Northern Hemisphere extratropics. We find also considerable differences between the two experiments over the extratropical North Pacific and over the extratropical North Atlantic in the vicinity of the Aleutian and the Icelandic low, respectively (Fig. 32a). These differences reflect a weaker enhancement of both the westerly winds on the southern sides of the low pressure systems and the easterly winds in the areas further south. The differences in the climate change signals, in particular those in the extratropical regions of both hemispheres result largely from deviations in the simulations of the present-day climate (Fig. 33a), when the systematic differences between the time-slice and the greenhouse gas experiment are considerably larger than for the simulations of the future climate (Fig. 33b).

In the upper troposphere (at 200 hPa) the time-slice experiment (Fig. 34) reveals an

intensification and southward shift of the areas with maximum westerly winds in the Northern Hemisphere extratropics in the future climate. On both the northern and the southern side of the Northern Hemisphere polar and subtropical jet streams, on the southern side particularly near their entrance regions, the westerly winds are reduced. In the Southern Hemisphere the area with the strongest westerly winds, which is located approximately between 40 and 70° S, is shifted slightly poleward, and the maximum wind speed is increased in the future climate. As in the Northern Hemisphere the strength of the zonal wind component is reduced on both sides of the jet stream.

Also in the upper troposphere the climate change signal obtained from the greenhouse gas experiment is generally similar to the change derived from TSL, but in most areas more pronounced (Fig. 35). Considerable differences between the two experiments (Fig. 36) occur in particular in the extratropics. At approximately the latitudes between 40 and 80° N and between 50 and 75° S the increase in the westerly winds is smaller in TSL than in GHG (Fig. 36b), and also the reduction of the westerly winds in the zone between 40 and 50° S is less pronounced. This can also be seen from the geographical distribution of the differences between the two experiments (Fig. 36a), since the differences in the Southern Hemisphere extratropics are zonally symmetric. In the Northern Hemisphere extratropics, on the other hand, the distribution of the differences shows large variations with longitude. Largest differences occur over the North Atlantic, where GHG shows a rather large enhancement of the westerly winds in a zonal band between 50 and 70° N. In the tropics and subtropics the differences have a bi- or tripolar structures in several areas. In the Pacific area we find, for instance, negative differences just south of the equator, positive ones just north of the equator and negative ones over the southern US, reflecting the smaller change in these areas in TSL. In the Atlantic region, on the other hand, the negative deviations off Northwestern Africa and the positive one off equatorial Africa indicate a quite different structure of the climate change in TSL than in GHG with an intensification of the westerly winds in the tropics and a relatively strong reduction of the westerly winds in the subtropical region (see Fig. 34c). The differences between the climate change signals obtained from the two experiments are generally mainly due to the differences in the simulations of the present-day climate (Figs. 35a, b). Different to the meteorological variables presented above, in this case also the differences between the simulations of the present-day climate in the tropics are larger than for the future climate (Figs. 35c, d), and the spatial structure of the deviations between the two experiments is quite similar for both periods.

5.4 Screen temperature

The most interesting meteorological variables regarding the impact of the changes in climate associated with the anticipated increase in the atmospheric concentrations of the important greenhouse gases are those that can be “felt” directly in the environment the human society lives in. In this section I therefore have a look at the temperature near the ground, i.e., in 2 m height, and in section 5.5 at precipitation.

5.4.1 Global and zonal means

Figure 38 shows area averages of the annual mean temperature in 2 m for both the time-slice and the greenhouse gas experiment. I distinguish between the global mean values and the values for land and ocean areas. According to this, the global mean temperatures are somewhat higher in TSL than in GHG for both periods of the experiment, whereas the change in the global mean temperature (about 2.5 °C in both experiments) is somewhat larger in GHG. These differences arise mainly from the land areas, since due to the same underlying SSTs the differences over the ocean areas are minor. The differences between the climate change signals obtained from the two experiments are, however, very small compared to the signals themselves.

The zonal mean values of the annual mean screen temperature (Fig. 39) reveal that the deviations between the two experiments (the temperatures in TSL exceed those for GHG) largely occur at the high latitudes of both hemispheres and in the Northern Hemisphere extratropics. The most pronounced differences between the climate change signals, on the other hand, occur in the Northern Hemisphere extratropics (Fig. 39c). Considering the ocean areas only (Fig. 40), we find the strongest warming in the Arctic region, which is covered to a lesser extent by sea-ice in the future climate (see Figs. 11, 13). It is also in the areas covered with sea-ice, where the temperatures in TSL typically exceed those for GHG. Considering the land areas only (Fig. 41), the temperatures in TSL are higher than those in GHG in the Northern Hemisphere extratropics, while they are lower in most of the Southern Hemisphere extratropics. It is over the land ares of the Northern Hemisphere extratropics and of the Southern Hemisphere midlatitudes, where the warming inferred from GHG exceeds the warming obtained from TSL. Further, the warming is generally stronger in the Northern than in the Southern

Hemisphere, since the Northern Hemisphere contains a relatively large part of the land masses, where the warming is typically stronger than for the oceans (see Fig. 42).

5.4.2 Geographical distribution

The geographical distributions of the annual mean temperatures in 2 m as obtained from the time-slice (Fig. 42) and from the greenhouse gas experiment (Fig. 43) reveal both a warming over most of the globe in the future climate. The warming is generally stronger over the land than over the ocean areas. This is the case for all continents, but the warming is relatively weak in northern and central Europe and over the northwestern part of North America. Overall, the Northern Hemisphere contributes more to the global warming than the Southern. Furthermore, the strongest warming occurs at the high northern latitudes due to the melting of the Arctic ice sheet.

Even though the climate signals obtained from the two experiments are rather similar, there are some differences following the results presented in the previous section, in particular over the continents (see Fig. 38c). According to Figure 44a, the largest differences in the climate change signals can be found in northeastern Asia, where the warming is more than 1.5 °C smaller in TSL than in GHG. This difference between the two experiments can also be identified in the lower troposphere (see Fig. 25a). Other areas, where the increase in temperature is significantly weaker in TSL than in GHG, are eastern Europe, the Himalaya, the southern central and northeastern parts of North America and Australia. The distributions of the systematic differences between the experiments for the two periods (Fig. 45) show that the deviations in the extratropics, i.e., over North America and Eurasia on the Northern and Australia on the Southern Hemisphere, are larger in the simulations of the present-day climate.

5.5 Precipitation

5.5.1 Global and zonal means

Considering the annual mean daily precipitation (Fig. 46), the time-slice experiment is characterized by a somewhat smaller amount of precipitation on a global scale during both

periods of the experiment. These differences are mainly related to the land areas, whereas over the ocean areas the precipitation actually is somewhat stronger in TSL for the future climate. As a result, the increase in precipitation over the ocean areas is considerably larger in TSL than in GHG. Even though over the land areas the increase in precipitation is more than twice as large in GHG than in TSL, on a global scale the increase of the amount of precipitation is larger in the time-slice than in the greenhouse gas experiment.

The zonal mean values of precipitation over the ocean areas (Fig. 47) reveal considerably more precipitation in TSL just north of the equator, where the convergence zones over the Pacific and Atlantic are located. South of the equator, where we find an area with strong convection over the Indian Ocean, there is less precipitation in TSL. According to both experiments, the future climate is characterized by more rainfall in the tropics and extratropics and less rainfall in the subtropics, especially in the Southern Hemisphere. The increase in the tropics is, however, much more pronounced in the time-slice experiment. Over the land areas (Fig. 48), on the other hand, there is generally more precipitation in GHG in the tropical regions between 25° S and 20° N. It is also at these latitudes, where the increase in precipitation is stronger in GHG than in TSL.

5.5.2 Geographical distribution

The geographical distributions of the annual mean daily precipitation as obtained from the time-slice experiment (Fig. 49) reveal an increase in precipitation at the high and mid-latitudes and in parts of the tropics. In particular over the northern Atlantic and northern Europe the climate will be wetter, but dryer over southern Europe, as in most of the subtropics. There will also be less rainfall in northeastern Brazil as well as in northwestern and southwestern Africa. A very strong increase in the amount of rainfall occurs over the tropical Pacific at the equator, whereas just north and south of this area the amount of precipitation is significantly reduced. This signal is very similar to the rainfall anomalies during an El Niño event and reflects that the change of the SSTs in the tropical Pacific is very similar to the SST-anomalies during an El Niño event. We find also a change in the precipitation over the Indian Ocean with more rainfall north of the equator and less rainfall south of it. This indicates both an intensification and a northward shift of the region with strong convection west of Indonesia. These changes go along with enhanced precipitation west of the Indian subcontinent and over the

Bay of Bengal, suggesting an intensification of the Indian summer monsoon in the future climate. The increase of precipitation in the tropics is related to the intensification of the large-scale convergence in these regions in the future climate. That is, the changes in the atmospheric transports of moisture lead to a stronger convergence of moisture and, hence, more convective rainfall in the tropics. This gives rise to a stronger upward motion in those areas and, as a consequence, a stronger sinking motion and less rainfall in the subtropics. Apparently the additional transports of moisture into the tropics initiate a self sustaining circulation cell similar to the Hadley-circulation with the aforementioned changes in the precipitation patterns as a consequence.

The climate change signal obtained from GHG (Fig. 50) shows in general the same spatial structure than the signal derived from TSL, but in the light of the differences to be seen in the area averages (see Fig. 46) there ought to be some differences. Firstly, the increase in rainfall over the land areas is larger in GHG than in TSL. According to Figure 51 this is the case for all continents except for the Middle East and Australia. This is presumably due to the fact that the soil is generally drier in TSL than in GHG, in particular during the warm season, so that the change in the locally produced rainfall is stronger in GHG than in TSL. Over the ocean areas, on the other hand, the increase in precipitation is generally stronger in TSL than in GHG. This is a combination of two different effects. Firstly, the increase in rainfall in the ITCZ is typically stronger in TSL, presumably due to the stronger convective activity in the time-slice experiment. In some areas, on the other hand, the reduction in precipitation is not as strong in TSL as in GHG. These areas are, for instance, the northern Pacific and the northern Atlantic between 20 and 50° N. At the same time the increase in the areas further north is reduced in the time-slice experiment. These differences are due to differences in the changes in the large-scale circulation in these areas (see section 5.1), namely the intensification of the stormtracks in the future climate, which is more pronounced in GHG than in TSL. Different to the meteorological variables discussed before the horizontal distributions of the systematic deviations between the two experiments for the two periods of the experiments (Fig. 52) do not give any clear indication of, whether the differences of the climate change signals arise from differences in the simulations of the present-day or of the future climate.

One phenomenon of particular interest, where one could expect a more realistic simulation at the high horizontal resolution, is the Indian summer monsoon. Figure 53 shows the geographical distributions of the daily precipitation averaged over the period June to September

for the simulations of the present-day climate by the two models. The time-slice experiment (Fig. 53a) reveals characteristic maxima of rainfall just south of the equator in the area west of Indonesia and further north over the Bay of Bengal as well as in northern Bangladesh at the foot of the Himalayas. A relatively large amount of precipitation appears also on the Indian southwest coast, while it is rather small over the western part of the Indian subcontinent and east of Sri Lanka. This distribution is in quite good agreement with observations (Annamalai et al. 1998). The only problems are the underestimation of the rainfall on the Indian west coast and the relatively strong precipitation in the region south of India. In the greenhouse gas experiment (Fig. 53b) the distribution of the precipitation in southeastern Asia looks quite different and, hence, reveals quite substantial discrepancies with observations. First of all, the maxima over the Bay of Bengal and in Bangladesh are hardly visible. Moreover, the maximum on the Indian southwest coast does not exist. Instead we find a quite unrealistic maximum near the equator, since the western part of the maximum in the area south of India can not be found in observations and the eastern part of the maximum in the area west of Indonesia is far too strong. The overestimation of the precipitation in this area in the low resolution model is so large that it is also visible in the zonal mean values over the whole globe in the zone between 10° S and the equator (Fig. 52b).

6. Summary and concluding remarks

In this paper I have investigated, to which extent the assessment of anthropogenic climate change depends on the horizontal resolution of the A-GCM employed. I have done that by comparing the change in climate inferred from a time-slice experiment with the ECHAM4 A-GCM at a horizontal resolution of T106 with the change obtained from the climate change simulation with the ECHAM4/OPYC coupled model at a horizontal resolution of T42 that has provided the lower boundary forcing for the time-slice experiment.

We have found that the changes in climate as obtained from the two experiments do depend on the horizontal resolution of the A-GCM. This is he case for both area averages and the local values of various meteorological variables. These differences in the climate change signals, which result mainly from deviations in the simulations of the present-day climate, are related to a different impact of the horizontal resolution on the simulation of the present-day than on the simulation of the future climate, which has been affected by the anticipated

increase in the atmospheric concentrations of the important greenhouse gases. As to be seen from Table 2, where the root-mean-square (rms) deviations between the two experiments for the simulations of the present-day and future climate as well as for the climate change signals are given, for all the meteorological variables except precipitation the rms deviations for the first period exceed the rms deviations for the second period of the experiments. The largest differences between the two periods are found for the zonal wind component in the lower troposphere and the sea-level pressure, while the differences for the temperature in the lower troposphere are considerably smaller, but still reflecting the general trend as described before. The rms deviations for the climate change signals are significantly smaller than the rms deviations for the present-day and future climate. The differences between the climate change signals and, hence, the uncertainties are smallest as compared to the rms deviations for the two time-slices for the temperatures near the surface and in the lower troposphere, but also for the zonal wind component in the higher troposphere, whereas the uncertainties are rather large for the zonal wind component in the lower troposphere.

The relative importance of the contributions from the simulations for the two periods of the experiments to the differences in the climate change signals varies, however, with latitude (Fig. 54). In case of the sea-level pressure, for instance, the rms deviations in the tropics are considerably larger for the future than for the present-day climate, while we find the opposite behaviour in the extratropical regions. This can also be seen from Figure 56c, where the rms deviations for the two periods of the experiments are shown. For the temperatures we find only slightly larger deviations for the future climate in the tropics, but larger deviations for the present-day climate only in the Northern Hemisphere extratropics, indicating the importance of the land areas (see Figs. 55a, b). While for the zonal wind components the deviations are generally larger for the present day climate (see Figs. 56a, b), the precipitation reveals only small differences between the rms deviations. The most pronounced differences occur in the tropics just north of the equator, where the deviations are somewhat larger for the future climate, and to the north between 10 and 20° N with larger deviations for the present-day climate (Fig. 55c).

These differences in the simulations of the climate for the two periods of the experiments at the different horizontal resolutions are related to two different causes. Firstly, the incorporation of the non-linear interactions with those scales that are not resolved at the low resolution and their impact on the dynamical characteristics of the model, and secondly, the different

behaviour of the physical parameterizations at the different resolutions and their local impact on certain meteorological variables such as the near-surface temperature and precipitation and their remote impact on the large-scale circulation. Moreover, the more realistic representation of the topography at the high resolution effects the simulations of a number of processes and phenomena on local as well as on regional scales.

A question, which has not been explicitly addressed in my paper, but certainly should be kept in mind is the general performance of the ECHAM4 A-GCM at horizontal resolutions of T106 and T42 compared to observational data. I therefore refer to the study by Stendel and Roeckner (1998), who have investigated the impact of the horizontal resolution on the simulated climate statistics in ECHAM4. They concluded that the higher horizontal resolution not automatically reduces the systematic model errors, because some of the physical parameterizations, which depend on resolution, have generally been tuned at the low horizontal resolution. While this is the case for the large-scale circulation, the simulation of the smaller-scale individual processes and of regional circulation patterns that are effected by the local topography is generally improved at the high resolution.

The motivation for performing the time-slice experiment has been to provide a global data set at a resolution that is fine enough to give information about climate on a regional scale and, hence, allow for an assessment of local impact of the anticipated change in climate including the impact on the society as well as on the economy. At the moment a number of studies are actually conducted, where data originating from the time-slice experiment are used to asses, a.o., the impact of climate change on storms, wave characteristics and storm surges in the northeastern Atlantic (e.g., WASA Group 1998) and the effect on the storm surges on the European coast lines. Considering the quite realistic simulation of the rainfall patterns associated with the Indian summer monsoon in the time-slice experiment I will investigate the characteristics of the Indian summer monsoon in further detail and assess the possible changes in the characteristics of this phenomenon in the future climate. Another area of research, where we currently work on, are the changes in the statistics of extreme events in temperature and precipitation or winds due to the anticipated increase in the atmospheric concentrations of the important greenhouse gases (see, e.g., Zwiers and Kharin 1998). This includes a study on the changes in the intensity and the frequency of tropical cyclones in a warmer climate similar to Bengtsson et al. (1996). The regional climate is, however, affected by - and feeding back into - the large-scale circulation. Hence, the assessment of the changes in the large-scale circulation -

as well as their uncertainties -, which I have undertaken in this study, needs to be considered, when interpreting the results to be obtained from the kind of studies mentioned above.

Acknowledgements

I would like to thank the Max-Planck-Institute for Meteorology for their collaboration and providing us with the ECHAM4 A-GCM, in particular Erich Roeckner for his help with the experimental design of the time-slice experiment and Ulrich Schlese as well as Uwe Schulzweida for their assistance with the model. My thanks go also to Henrik Feddersen for his comments on an earlier version of the manuscript. This work was in part supported by the Danish Ministry of Transport and by the “Environment and Climate Programme” under contract ENV4-CT97-0640, “An enhanced resolution modelling study on anthropogenic climate change”.

References

Annamalai H, Slingo J, Hodges K, Rupa Kumar K, Tschuck P (1998) SHIVA Atlas. http://www.met.rdg.ac.uk/shiva/monsoon_atlas/title.html

Bacher A, Oberhuber JM, Roeckner E (1998) ENSO dynamics and seasonal cycle in the tropical Pacific as simulated by the ECHAM4/OPYC3 coupled general circulation model. Clim Dyn 14: 431-450

Beersma JJ, Rider KM, Komen GJ, Kaas E, Kharin VV (1997) An analysis of extra-tropical storms in the North Atlantic region as simulated in a control and $2\times CO_2$ time-slice experiment with a high resolution atmospheric model. Tellus 49A: 347-361

Bengtsson L, Botzet M, Esch M (1995) Hurricane-type vortices in a general circulation model. Tellus 47A: 175-196

Bengtsson L, Botzet M, Esch M (1996) Will greenhouse gas-induced warming over the next 50 years lead to higher frequency and greater intensity of hurricanes? Tellus 48A: 57-73

Broccoli AJ, Manabe S (1990) Can existing climate models be used to study anthropogenic changes in tropical cyclone climate? Geophys Res Lett 17: 1917-1920

Cubasch U, Hasselmann K, Höck H, Maier-Reimer E, Mikolajewitz U, Santer BD, Sausen R (1992) Time-dependent greenhouse warming computations with a coupled ocean-atmosphere model. Clim Dyn 8: 55-69

Deser C, Blackmon ML (1993) Surface climate variations over the North Atlantic Ocean during winter: 1900-1989. J Climate 6: 1743-1753

DKRZ (1992) The ECHAM3 atmospheric general circulation model. Techn Report No. 6: 184 pp

Essenwanger OM (1986) Elements of statistical analysis. In Landsberg HE (ed) World Survey of Climatology, General Climatology Vol 1B, Elsevier Science Publishers, 424 pp

Folland CK, Sexton DMH, Karoly D, Johnson CE, Rowell DP, Parker DE (1998) Influences of anthropogenic and oceanic forcing on recent climate change. Geophys Res Lett 25: 353-356

Houghton JT, Jenkins GJ, Ephraums JJ (eds.) (1990) Climate Change. The IPCC scientific assessment. Cambridge University Press, 364 pp

Houghton JT, Meira Filho LG, Callandar BA, Harris N, Kattenberg A, Maskell K (eds.) (1996) Climate Change 1995. The science of climate change. Cambridge University Press, 572 pp

Hurrell JW (1995) Decadal trends in the North Atlantic Oscillation: Regional temperatures and precipitation. Science 269: 676-679

Lau N-C, Nath MJ (1994) A modelling study of the relative roles of tropical SST anomalies in the variability of the global atmosphere-ocean system. J Climate 7: 1184-1207.

Lohmann U, Feichter J (1997) Impact of sulfate aerosols on albedo and lifetime of clouds: A sensitivity study with the ECHAM4 GCM. J Geophys Res 102: 13685-13700

Manabe S, Stouffer RJ, Spelman MJ, Bryan K (1991) Transient responses of a coupled ocean-atmosphere model to gradual changes of atmospheric CO_2. Part I: annual mean response. J Climate 4: 785-818

May W, Bengtsson L (1998) The signature of ENSO in the Northern Hemisphere midlatitude seasonal mean flow and high-frequency intraseasonal variability. Met Atmos Phys 69: 81-100

May W, Shea DJ, Madden RA (1992) The annual variation of surface temperatures over the world. NCAR Technical Note NCAR TN-372+STR: 134 pp

Meehl GA, Washington WM (1996) El Niño-like climate change in a model with increased CO_2 concentrations. Nature 382: 56-60

Mitchell JFB, Davies RA, Ingram WJ, Senior CA (1995) On surface temperature, greenhouse gases and aerosols: models and observations. J Climate 8: 2364-2386

Mitchell JFB, Johns TC (1997) On modification of global warming by sulfate aerosols. J Climate 10: 245-267.

Oberhuber JM (1993) Simulation of the Atlantic circulation with a coupled sea-ice - mixed layer - isopycnal general circulation model. Part I: Model description. J Phys Oceanogr 22: 808-829

Palmer TN, Sun Z (1985) A modelling and observational study of the relationship between sea surface temperature anomalies in the northwest Atlantic and the atmospheric general circulation. Q J R Meteorol Soc 96: 226-246

Rider KM, Komen GM, Beersma JJ (1996) Simulations of the response of the ocean waves in the North Atlantic and North Sea to CO_2 doubling in the atmosphere. KNMI Science Report WR-9605

Roeckner E, Arpe K, Bengtsson L, Christoph M, Claussen M, Dümenil L, Esch M, Giorgetta M, Schlese U, Schulzweida U (1996a) The atmospheric general circulation model ECHAM-4: Model description and simulation of present-day climate. MPI-Report No. 218: 90 pp

Roeckner E, Bengtsson L, Feichter J, Lelieveld J, Rodhe H (1998) Transient climate change simulations with a coupled atmosphere-ocean GCM including the tropospheric sulfur cycle. MPI-Report No. 266: 48 pp

Roeckner E, Oberhuber JM, Bacher A, Christoph M, Kirchner I (1996b) ENSO variability and atmospheric response in a global coupled atmosphere-ocean GCM. Clim Dyn 12: 737-754

Stendel M, Roeckner E (1998) Impacts of horizontal resolution on simulated climate statistics in ECHAM4. MPI-Report No. 253: 57pp

Timmermann A, Oberhuber JM, Bacher A, Esch M, Latif M, Roeckner E (1998) ENSO response to greenhouse warming. MPI-Report No. 251: 13pp

Timmermann A, Latif M, Bacher A, Oberhuber JM, Roeckner E (1999) Increased El Niño frequency in a climate model forced by future greenhouse warming. Nature 398: 694-696

WASA Group (1998) Changing waves and storms in the Northeast Atlantic. Bull Amer Met Soc 79: 741-760

Zwiers FW, Kharin VV (1998) Changes in the extremes of the climate simulated by CCC GCM2 under CO_2 doubling. J Climate 11: 2200-2222

Table 1:

Area	TSL-1		TSL-2	
	Variability	Linear trend	Variability	Linear Trend
North Atlantic	0.37	0.52	0.32	1.01
North Pacific	0.31	1.16	0.32	0.98
Niño 1+2	0.42	0.58	0.93	1.28
Niño 3	0.81	0.74	1.21	1.20
Niño 3.4	0.74	0.67	0.90	0.73
Niño 4	0.44	0.61	0.54	0.66

Interannual variability and linear trends of the sea surface temperatures in various regions (see text). Units are [°C] for the interannual variability and [°C/(90 years)] for the linear trends, respectively.

Table 2:

Meteorological variable	Rms deviations			Ratio of deviations	
	Pr-day[1]	Future[2]	Change[3]	2/1	3/Ave(1,2)
Temperature in 2 m [°C]	1.44	1.29	0.33	0.80	0.06
Temperature at 850 hPa [°C]	0.89	0.83	0.38	0.88	0.19
Precipitation [mm/month]	23.85	24.13	11.45	1.02	0.23
Zonal wind at 850 hPa [m/s]	1.16	0.89	0.68	0.59	0.44
Zonal wind at 200 hPa [m/s]	3.35	2.83	1.32	0.71	0.18
Sea-level pressure [hPa]	2.18	1.78	0.95	0.67	0.23

Root-mean-square deviations between the time-slice and the climate change experiment for the present-day and the future climate as well as for the climate change signals. Also the ratio of the deviations for the future and the present-day climate ("2/1") and the ratio of the deviations for the climate change signals and the mean deviations for the present-day and the future climate ("3/Ave(1,2)").

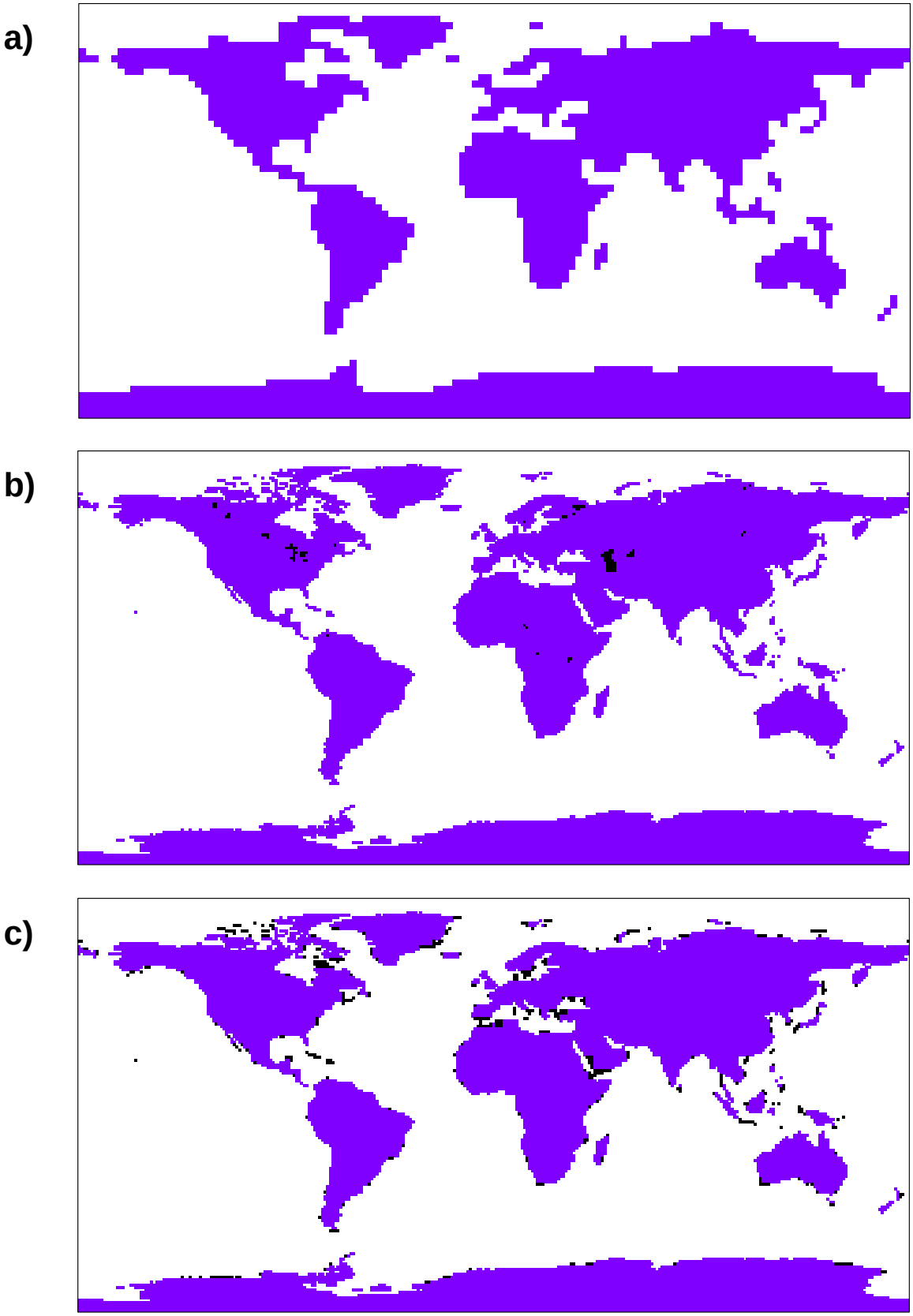

Fig. 1: Land-sea masks of ECHAM4 as used in the climate change experiment (a) and in the time-slice experiment (b, c). Marked in black are the large lakes, which have been transformed into land areas (b), and those areas, where the land-sea masks used in the climate change (a) and the time-slice experiment (b) do not overlap (c).

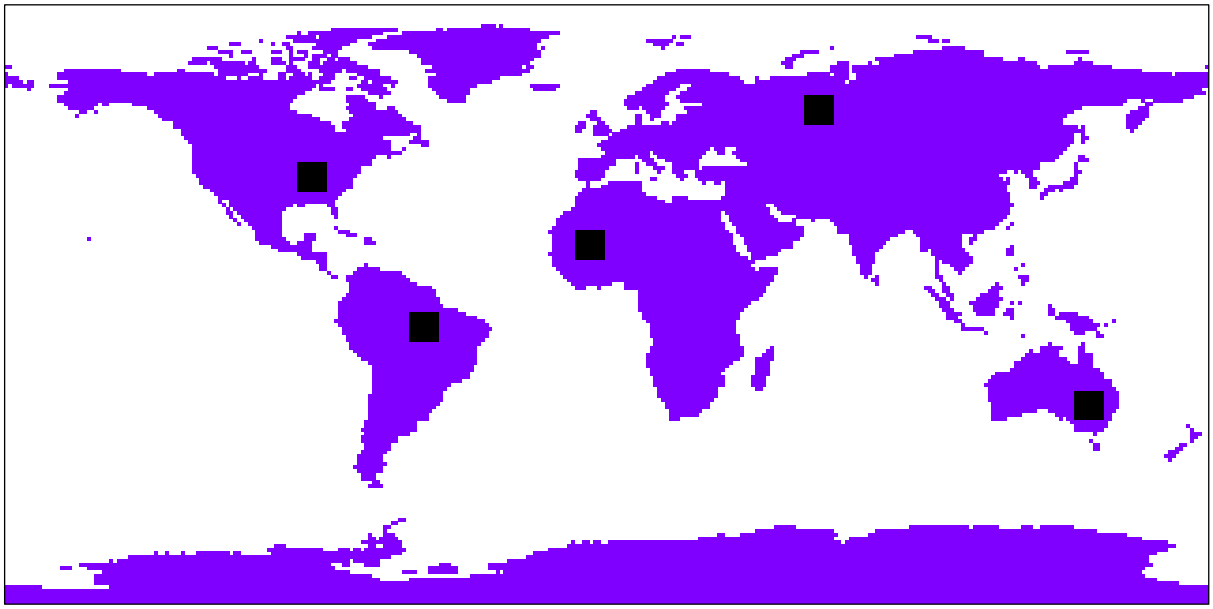

Fig. 2: Land-sea mask of ECHAM4 as used in the time-slice experiment with those five areas, where the soil temperatures have been analysed, marked in black: Central Eurasia, northwestern Africa, southeastern Australia, southeastern North America and northeastern South America.

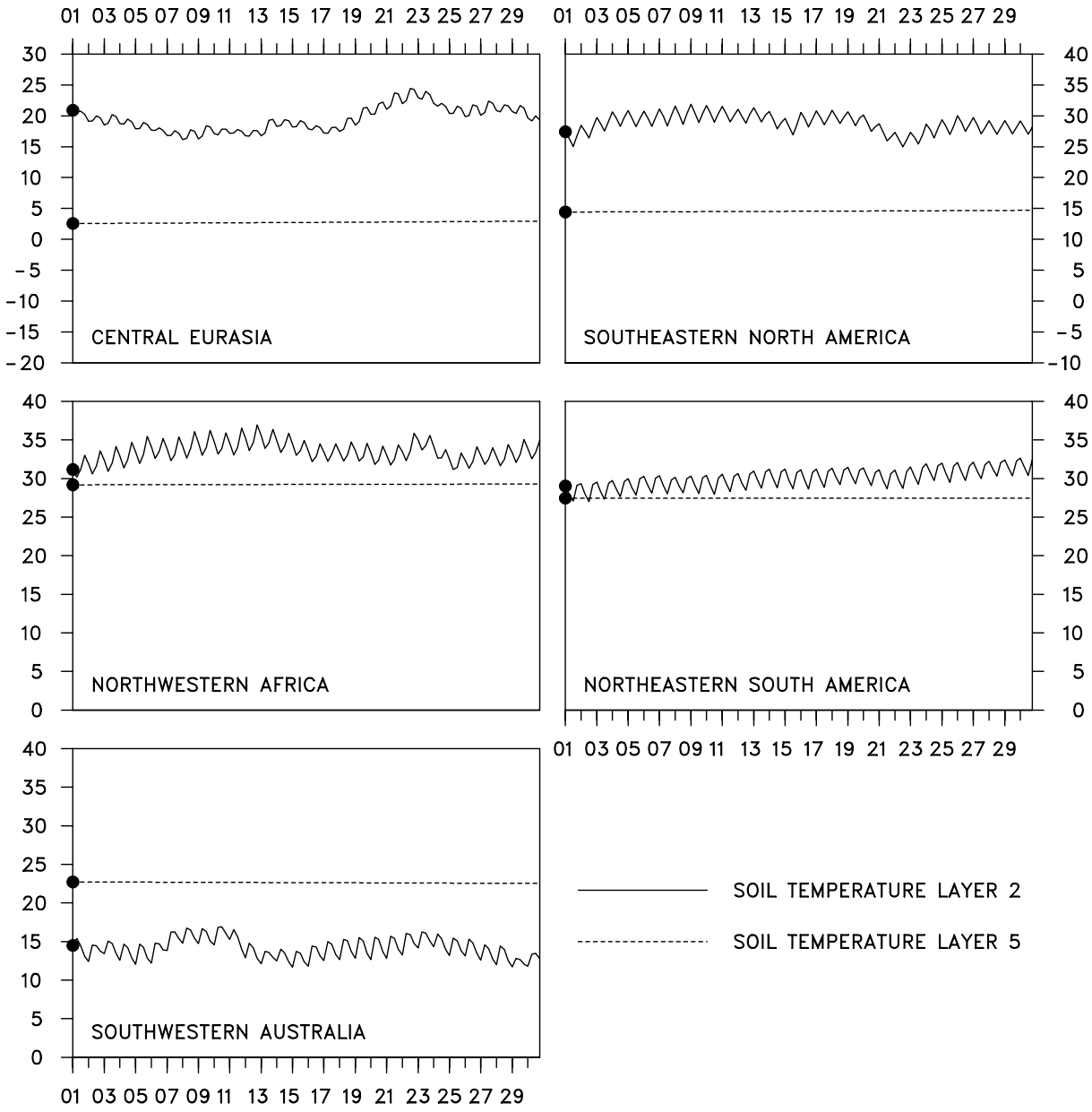

Fig. 3: Soil temperatures in two different layers for five different areas for the first month of TSL-1 (July 1968). Units are [°C]. Temperatures are given 4× daily, and the initial values are marked by dots.

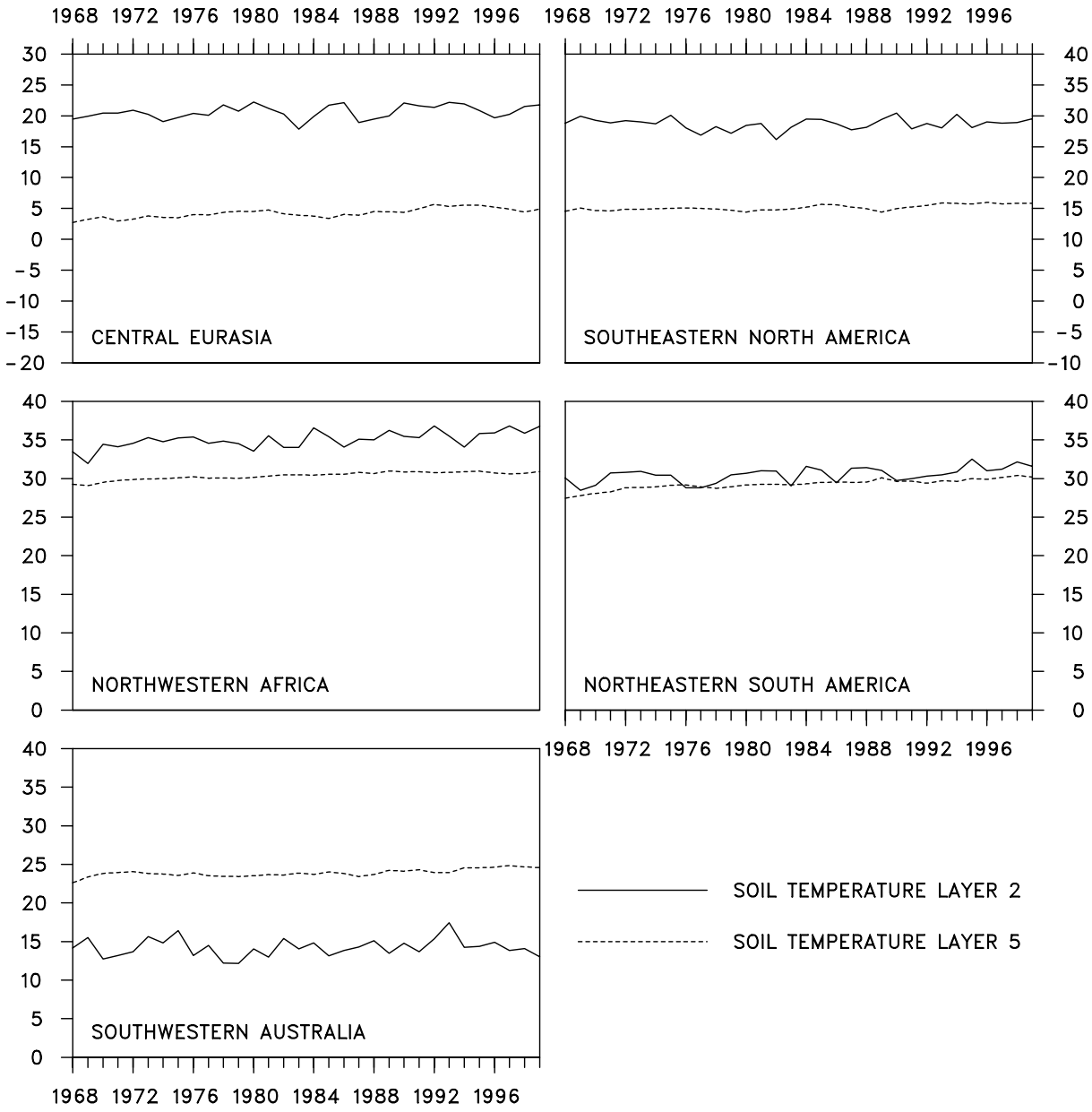

Fig. 4: Monthly mean (July) values of the soil temperature in two different layers for five different areas for TSL-1 and the two preceding years (spin-up). Units are [°C].

TSL-1

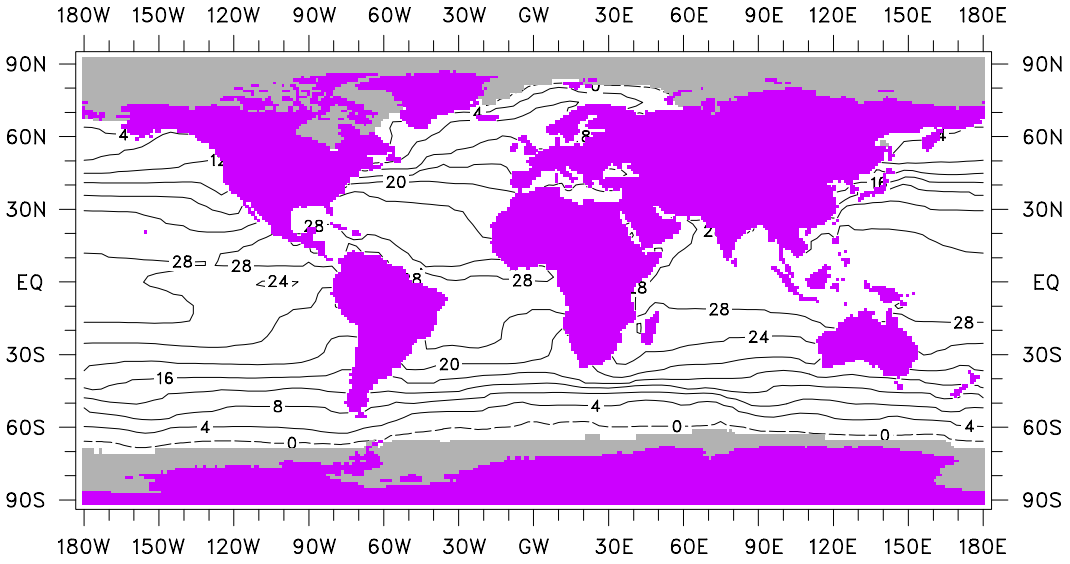

TSL-2

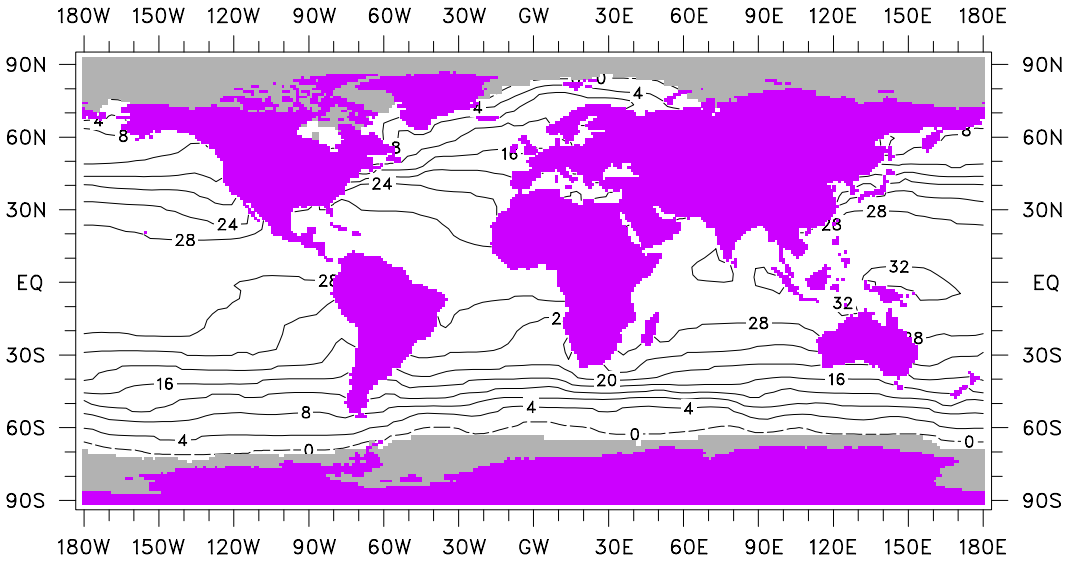

Fig. 5: Annual mean sea surface temperatures for TSL-1 and TSL-2. Units are [°C], the contour interval is 4 °C. Those areas that are covered by sea-ice for an extensive part of the year for the respective time-slice are marked by the light shading.

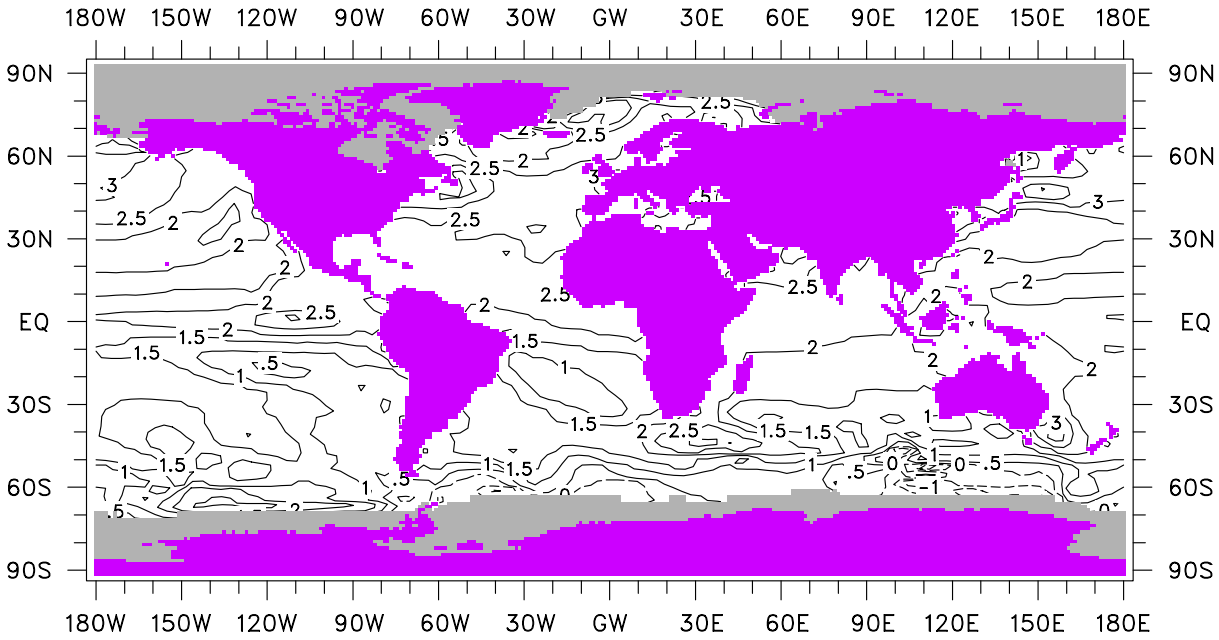

Fig. 6: Difference of the annual mean sea surface temperatures between TSL-2 and TSL-1. Units are [°C], the contour interval is 0.5 °C. Those areas that are covered by sea-ice for an extensive part of the year for either one of the time-slices are marked by the light shading.

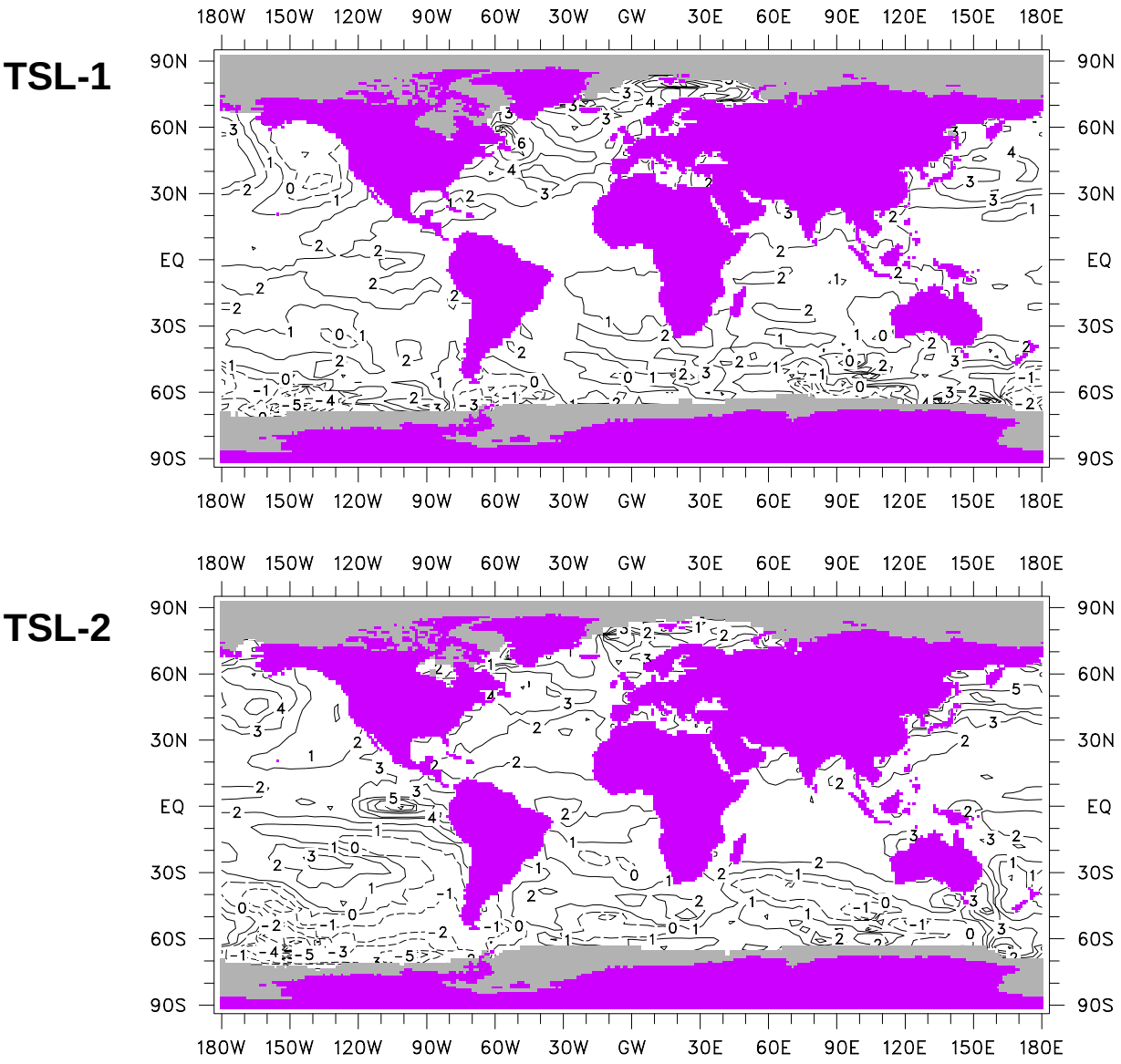

Fig. 7: Linear trend of the annual mean sea surface temperatures for TSL-1 and TSL-2. Units are [°C/(90 years)], the contour interval is 1 °C/(90 years). 90 years is the distance between TSL-2 and TSL-1. Those areas that are covered by sea-ice for an extensive part of the year for the respective time-slice are marked by the light shading.

TSL-1

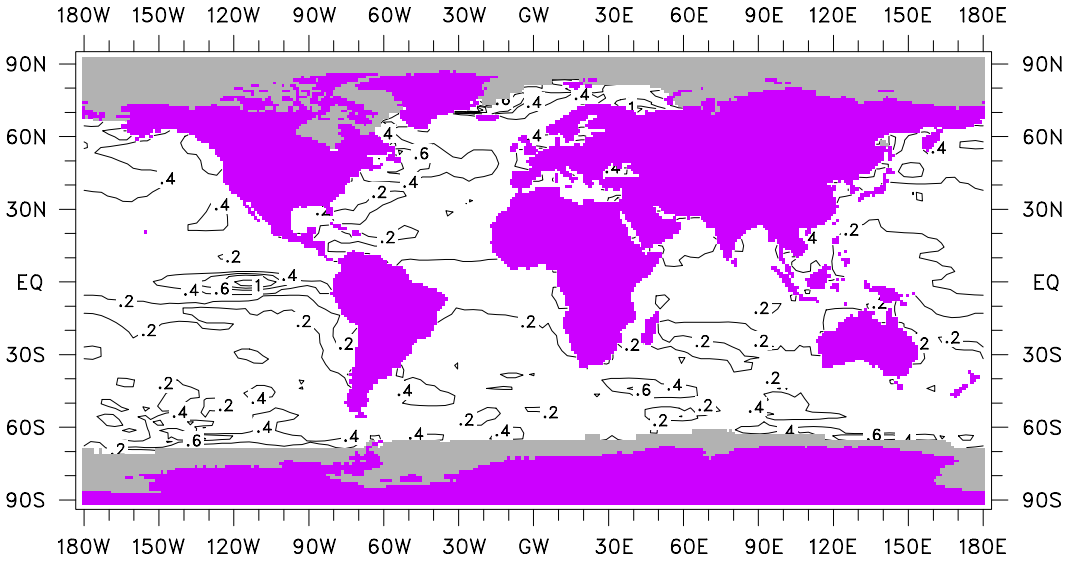

TSL-2

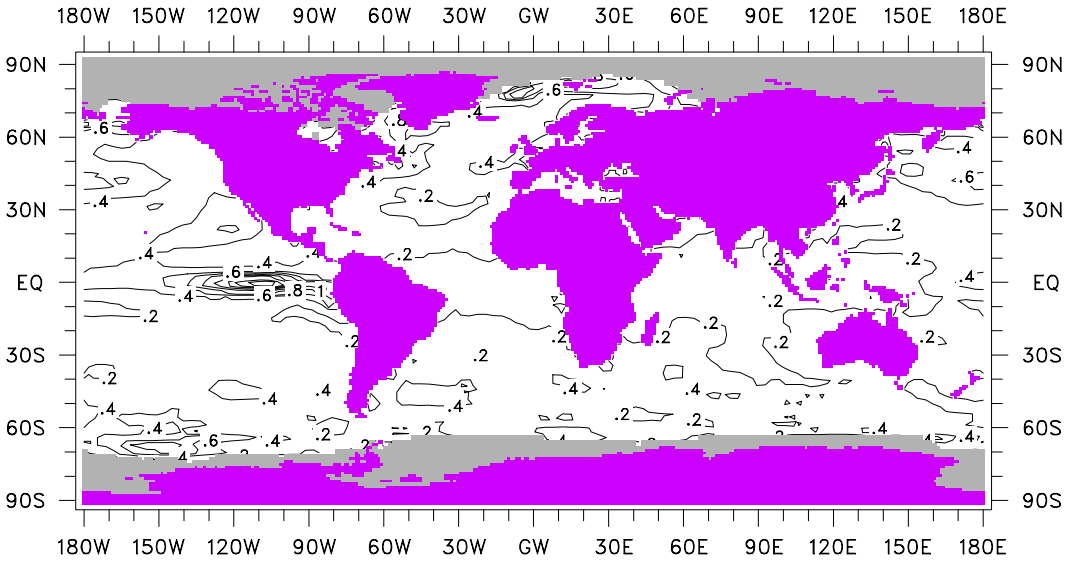

Fig. 8: Interannual standard deviation of the annual mean sea surface temperatures for TSL-1 and TSL-2. Units are [°C], the contour interval is 0.1 °C. Those areas that are covered by sea-ice for an extensive part of the year for the respective time-slice are marked by the light shading.

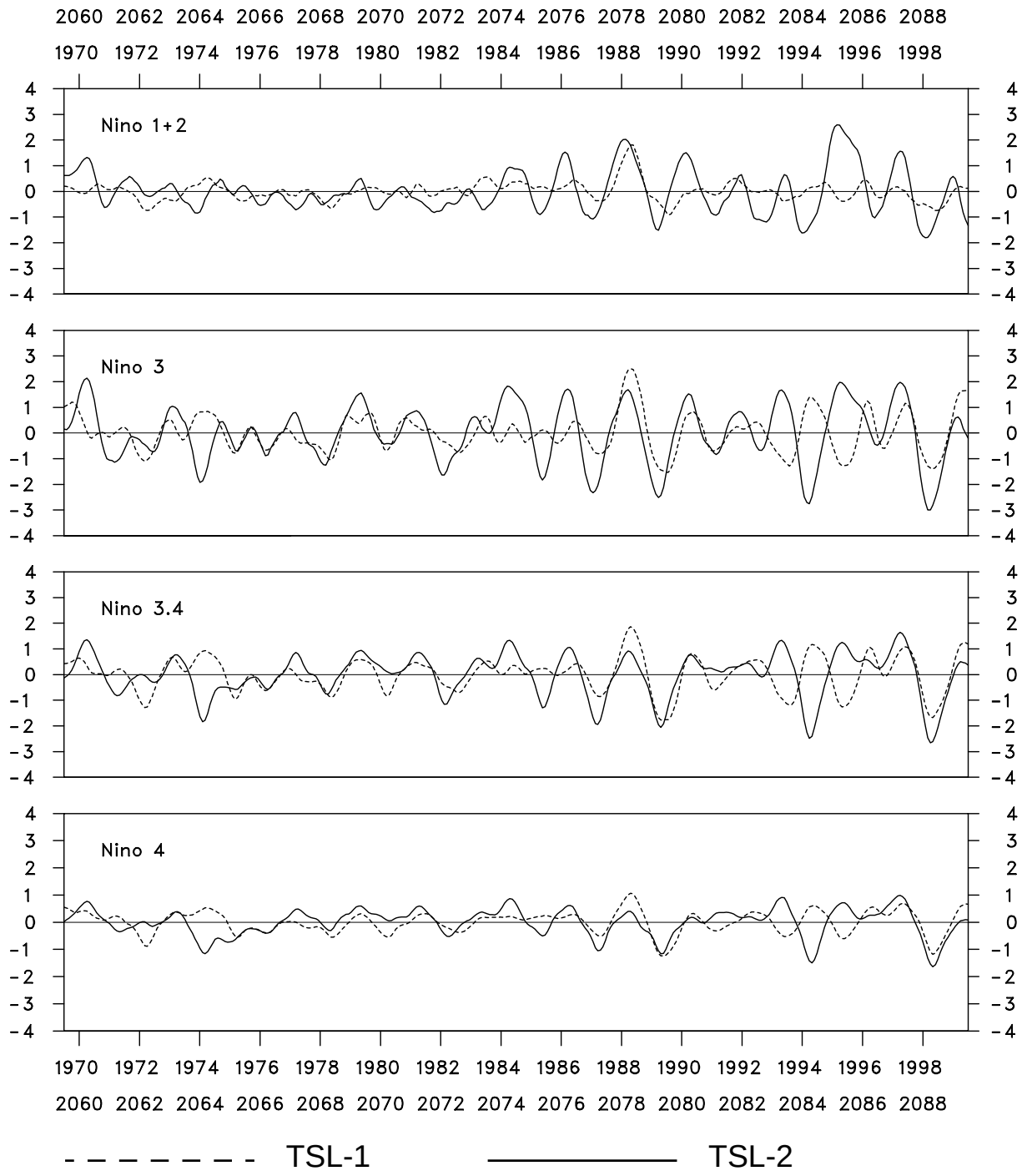

Fig. 9: Monthly mean sea surface temperature anomalies (with the mean annual cycle and a linear trend removed) for four different regions in the tropical Pacific for TSL-1 and TSL-2. A 5-month running mean filter has been applied. Units are [°C].

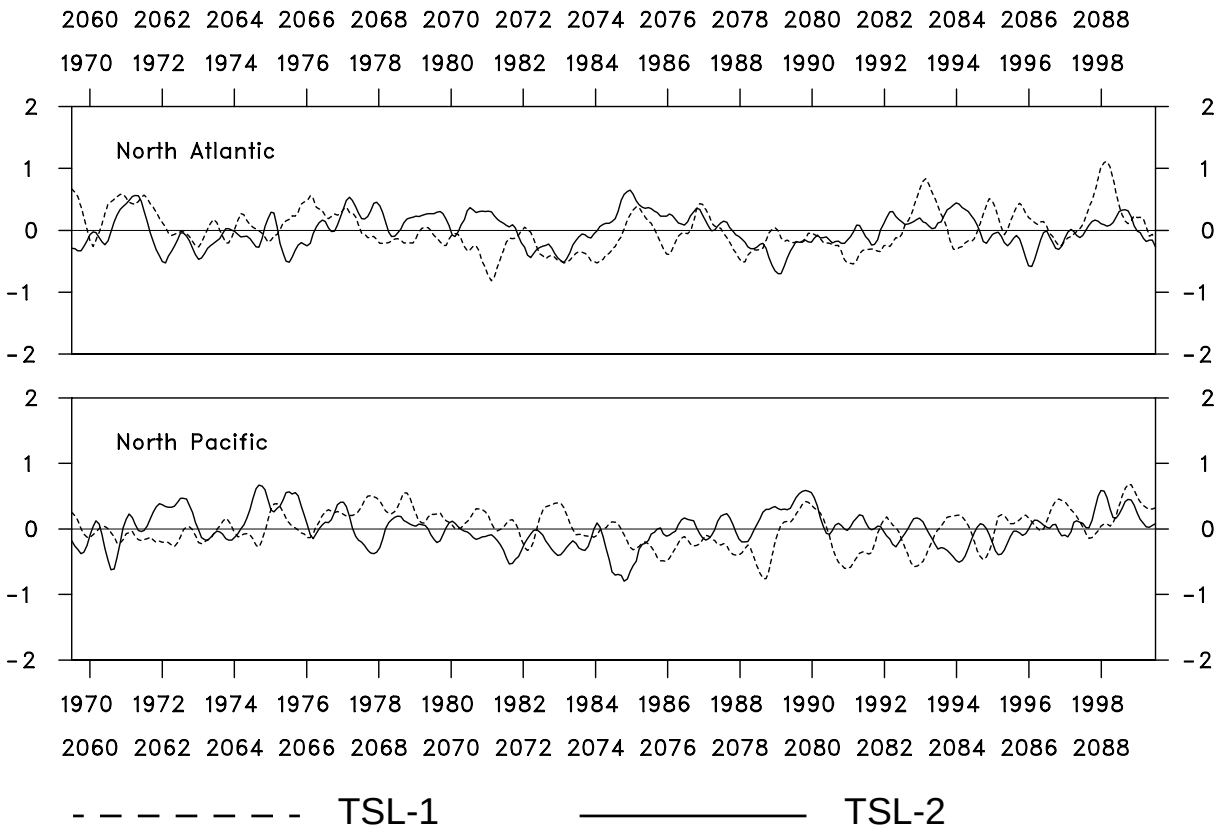

Fig. 10: As Fig. 9, but for two regions in the North Atlantic and the North Pacific, respectively.

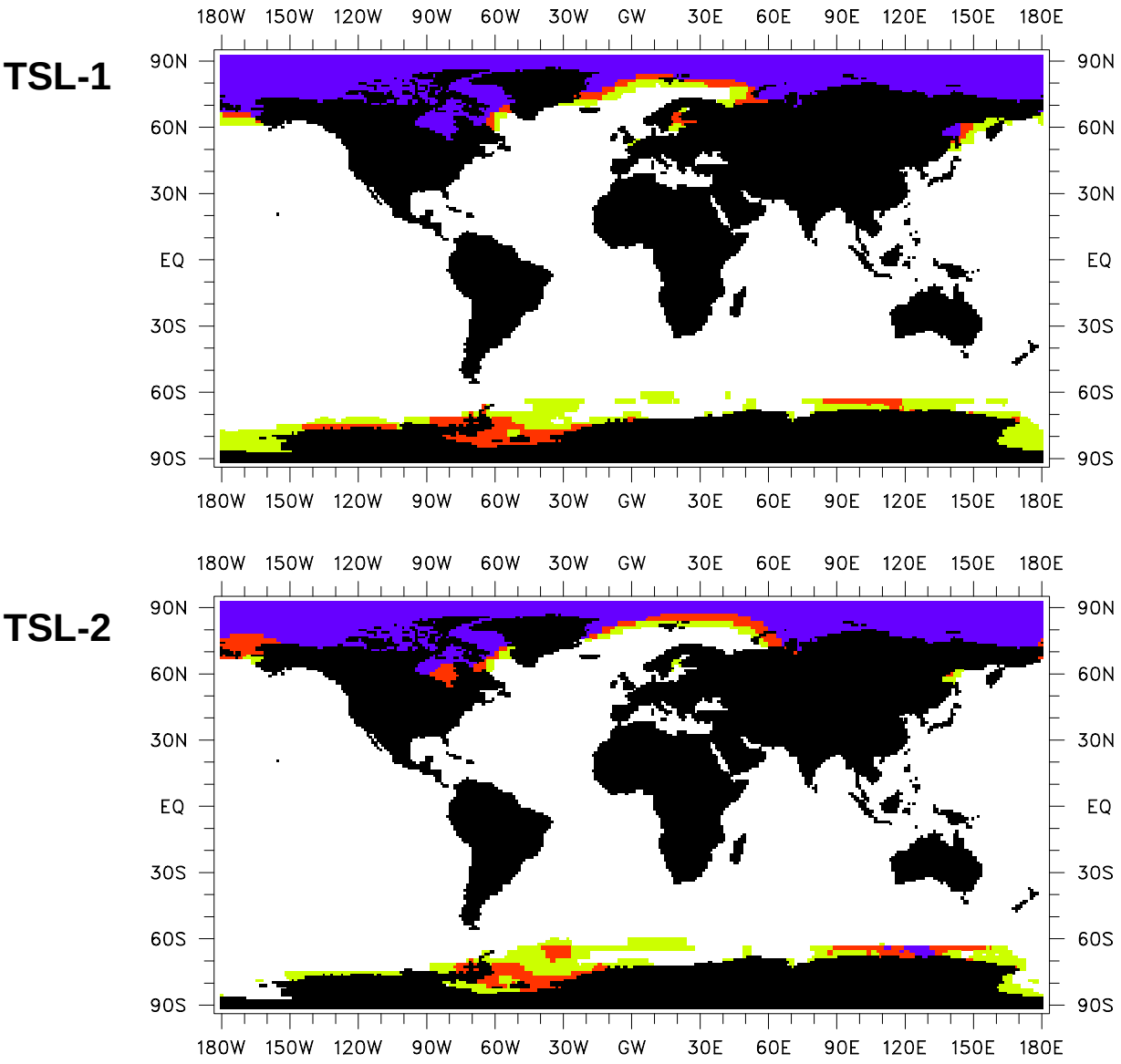

Fig. 11: Seasonal mean values (January to March) of the sea-ice extent for TSL-1 and TSL-2. Those areas that are covered by sea-ice in all years are marked by the dark shading, those areas that are covered more than half of the time but not permanently by the medium shading and those areas that are covered at least one year but not more than half of the time by the light shading.

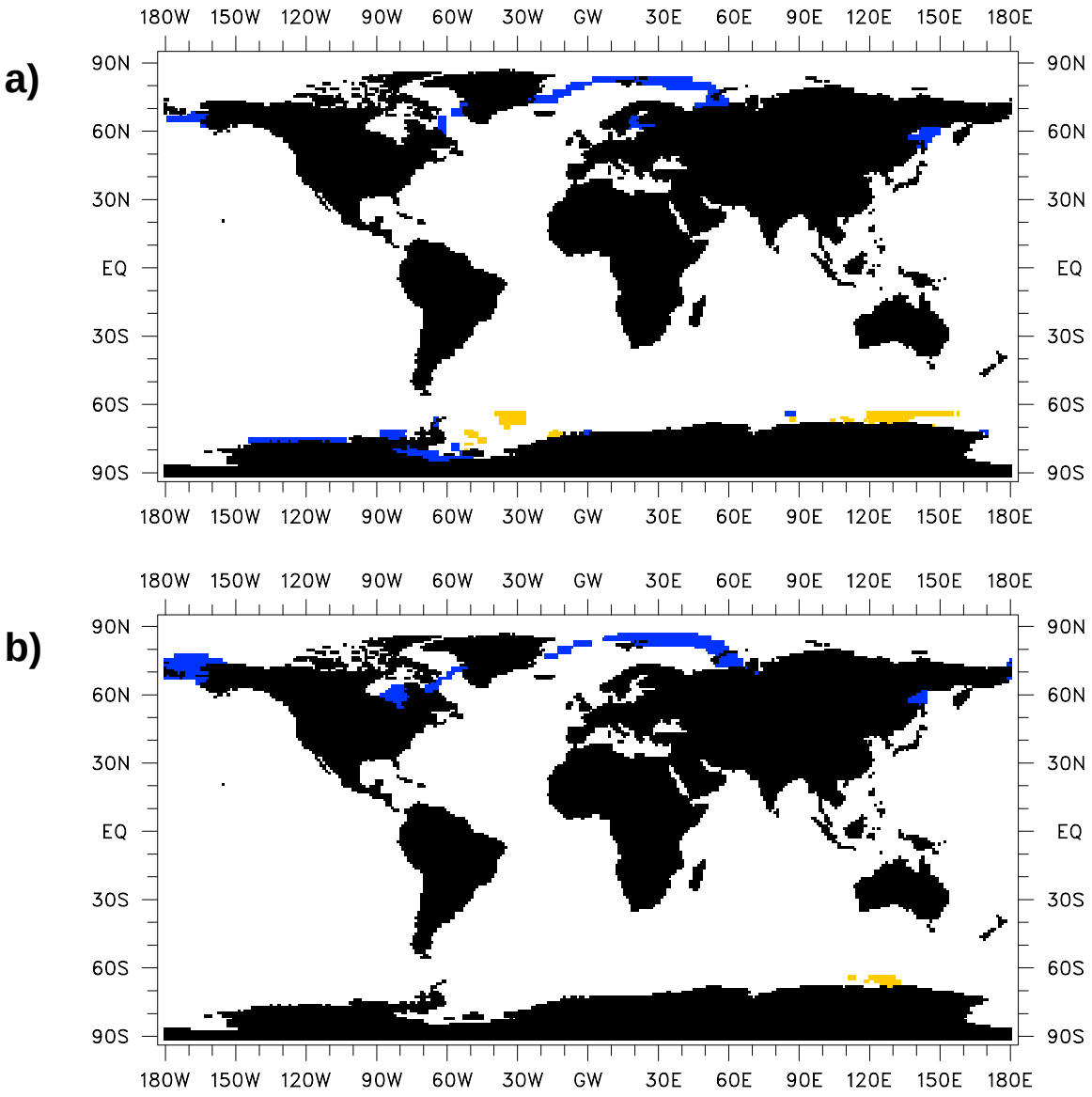

Fig. 12: Difference of the seasonal mean values (January to March) of the sea-ice extent between TSL-2 and TSL-1 distinguishing between those areas that are covered occasionally, i.e., more than 50% of the time (a) and permanently with sea-ice (b). The dark shading indicates those areas, where the sea-ice has vanished in TSL-2, the light shading the areas with additional sea-ice in TSL-2.

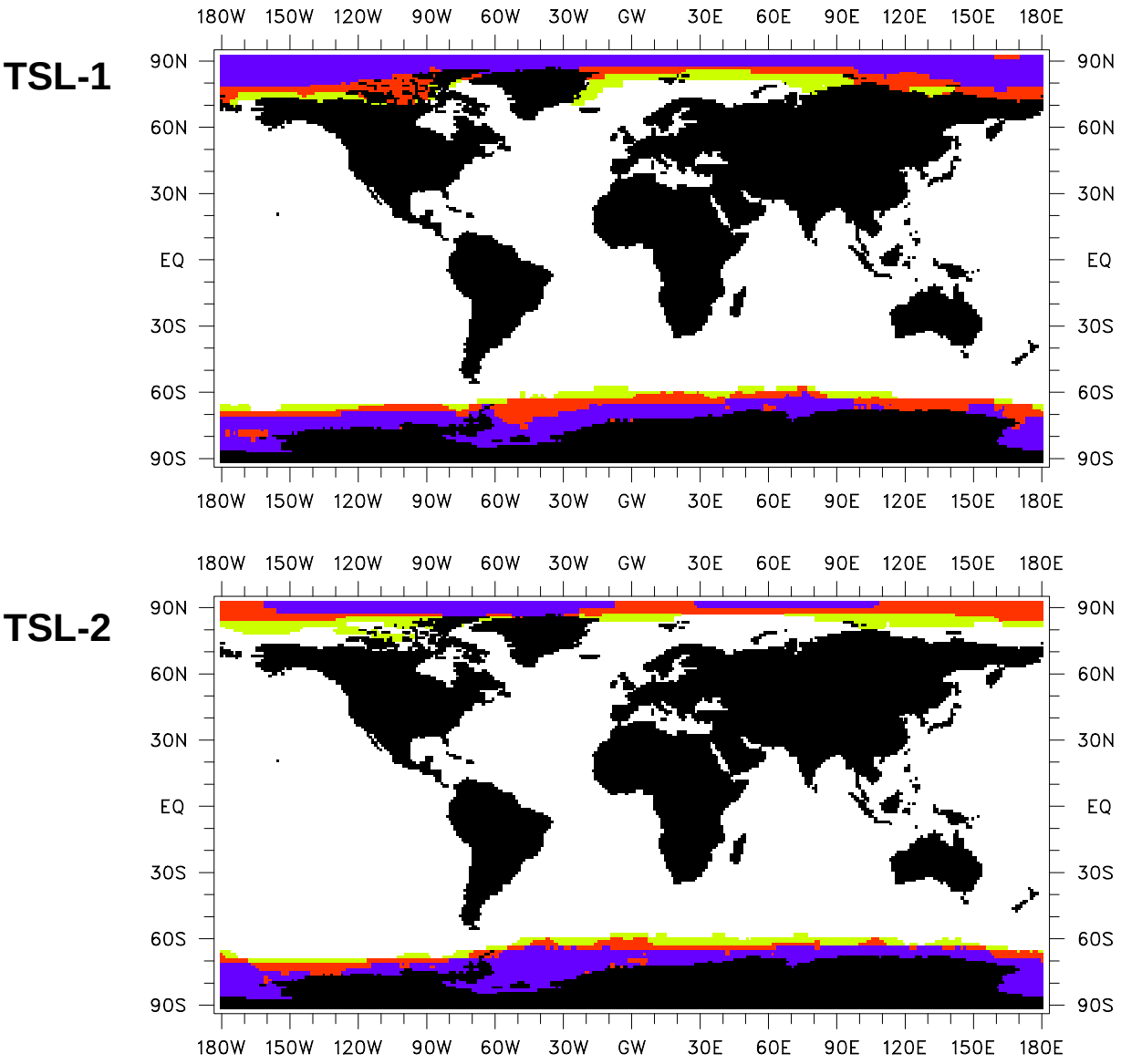

Fig. 13: As Fig. 11, but for the austral winter season (July to September).

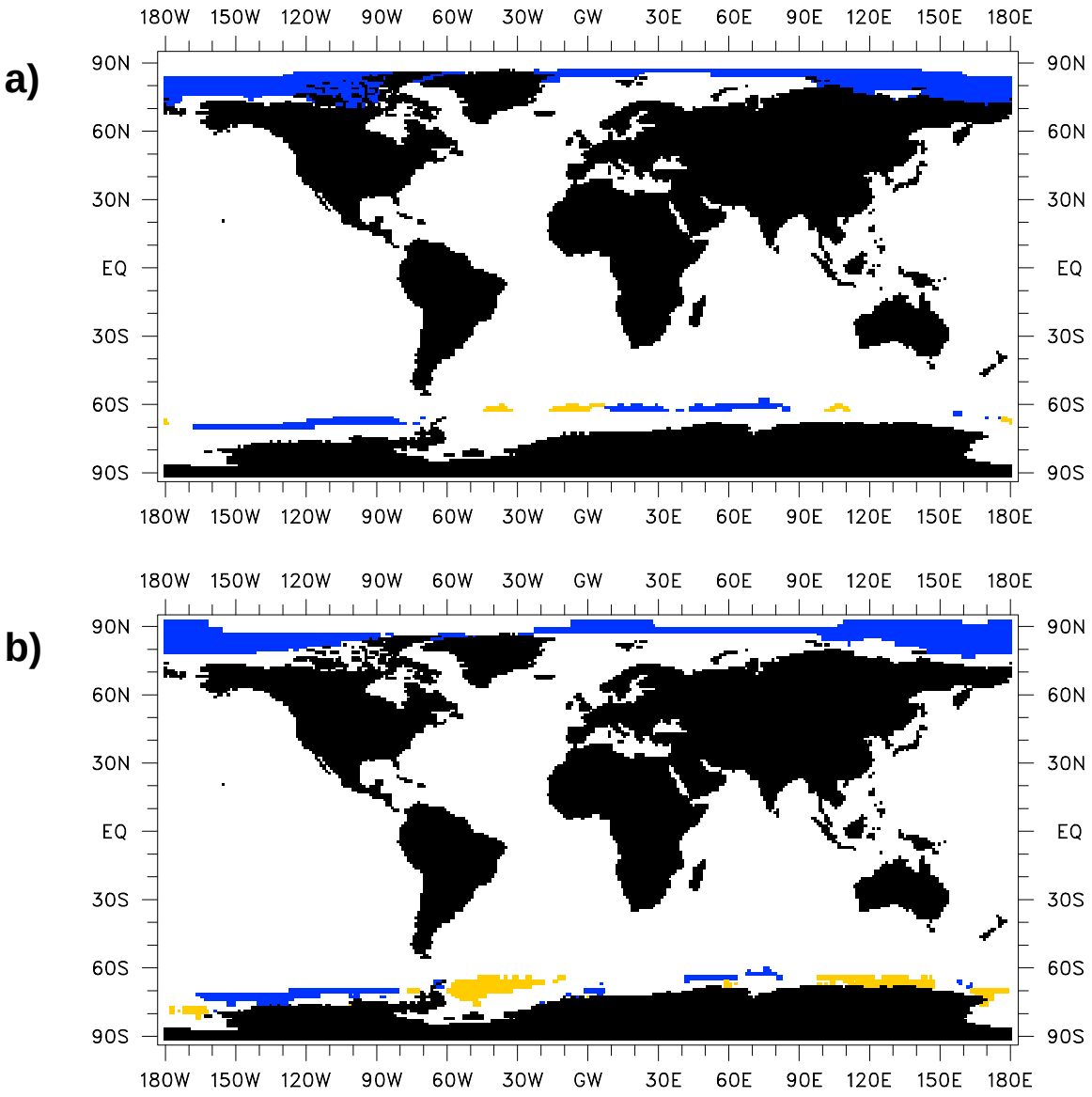

Fig. 14: As Fig. 12, but for the austral winter season (July to September).

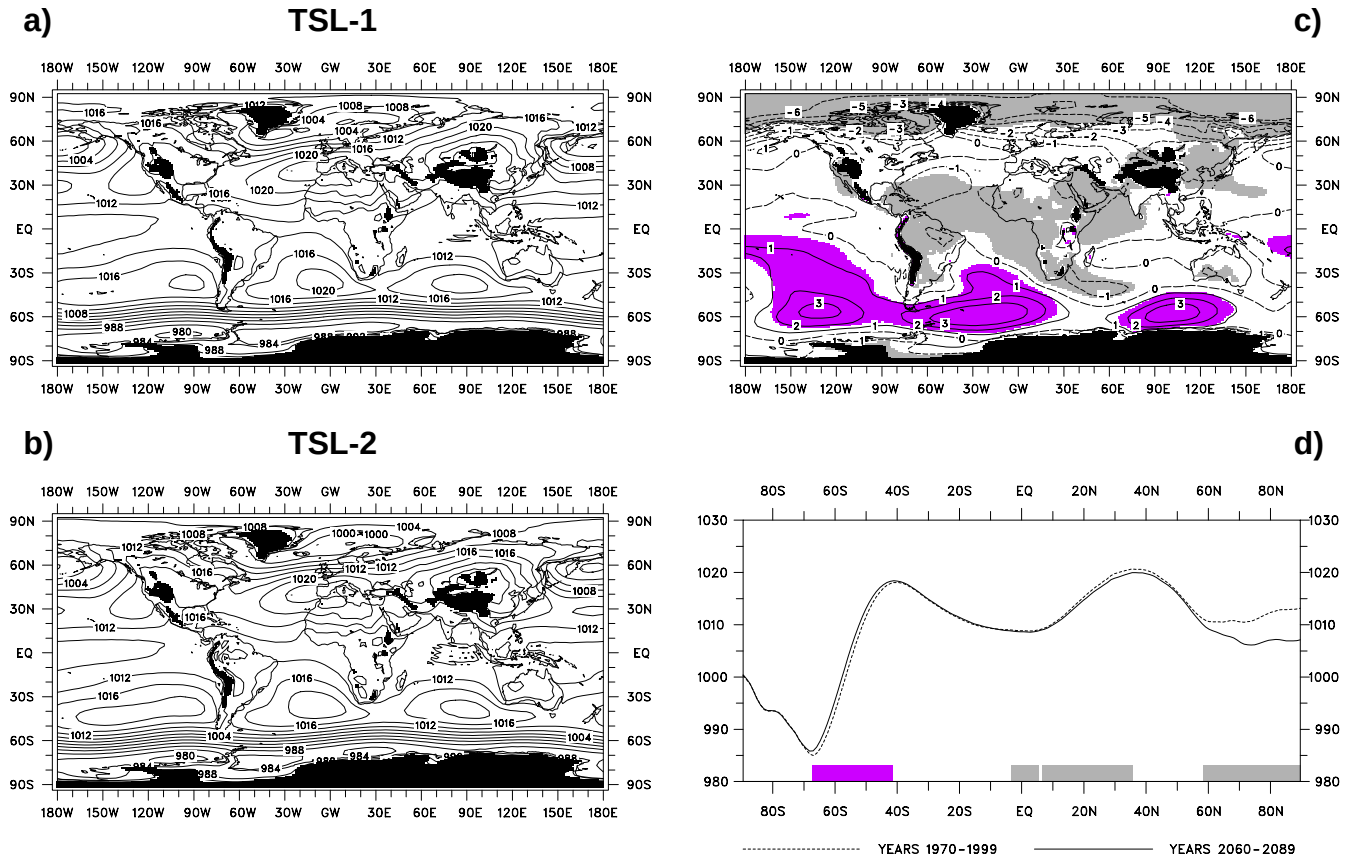

Fig. 15: Seasonal mean (December, January and February) sea-level pressure for TSL-1 (a) and TSL-2 (b). Units are [hPa], the contour interval is 4 hPa. Terrain higher than 1500 m is blanked out. Difference of the seasonal mean sea-level pressure between TSL-2 and TSL-1 (c). The contour interval is 1 hPa. The significance of positive (negative) differences at the 99%-level is marked by the dark (light) shading. Zonal mean values of the seasonal mean sea-level pressure for TSL-1 and TSL-2 (d). The significance of the positive (negative) differences of the zonal mean values between TSL-2 and TSL-1 at the 99%-level is indicated by the dark (light) bars at the bottom of the respective figure.

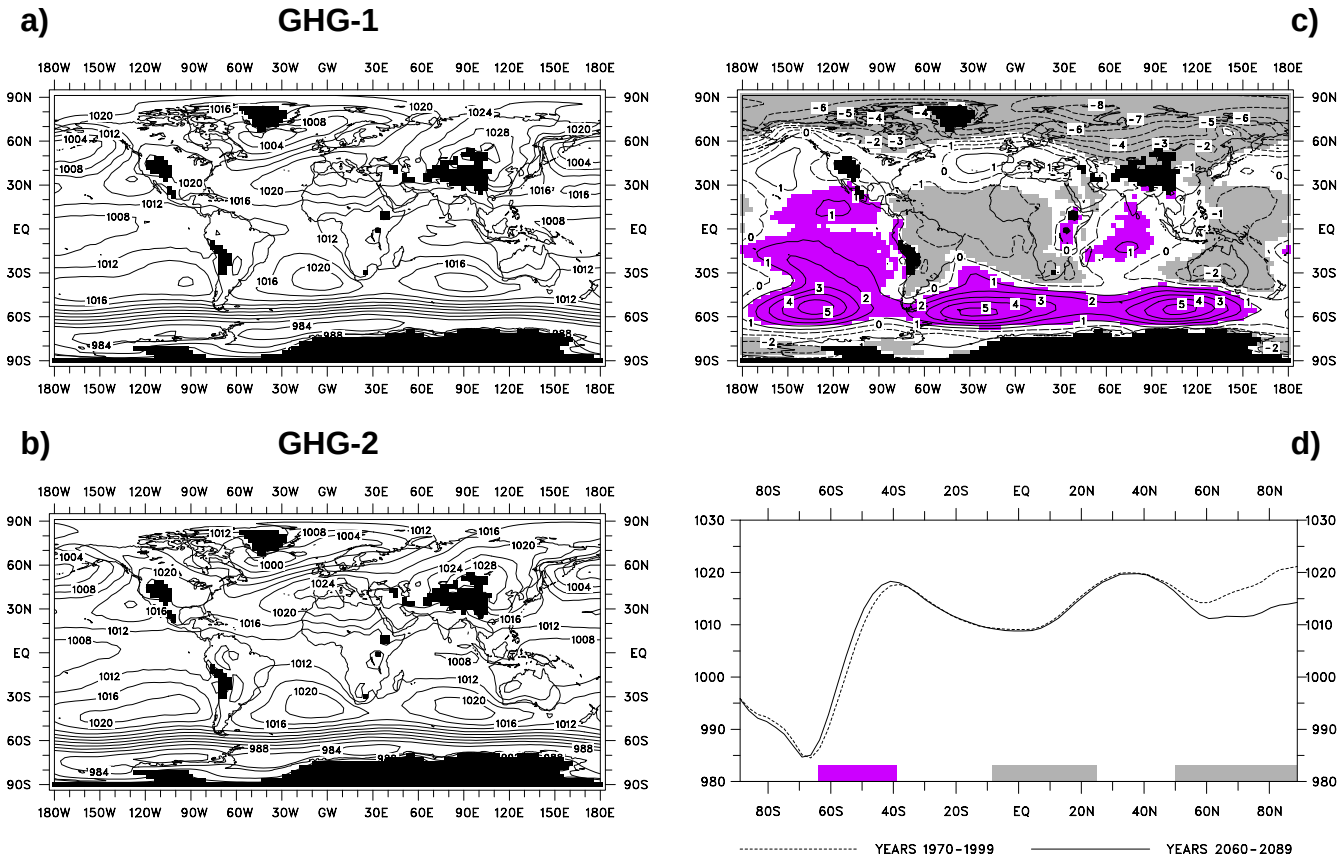

Fig. 16: As Fig. 15, but for GHG.

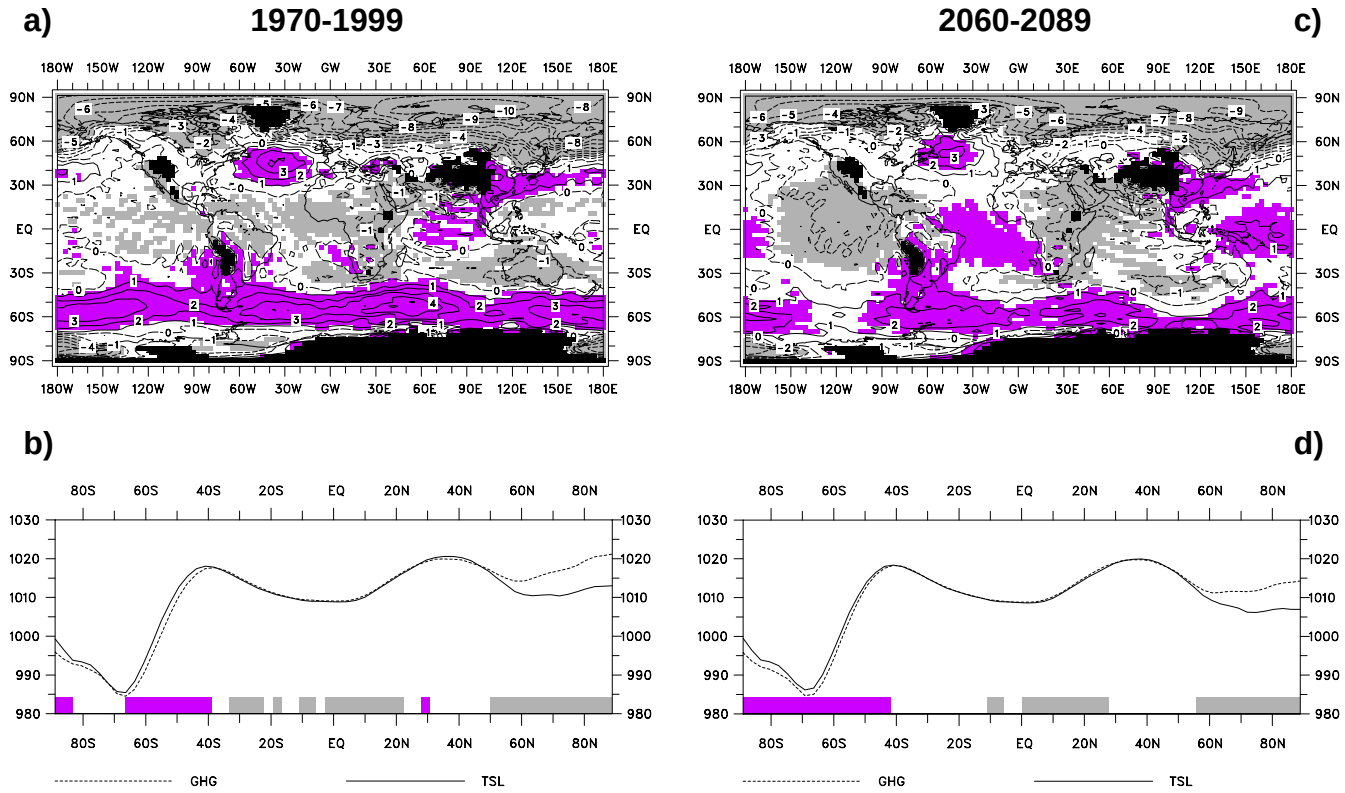

Fig. 17: Difference of seasonal mean sea-level pressure between TSL and GHG for the first (a) and the second period of the experiment (c). Units are [hPa], the contour interval is 1 hPa. The significance at the 97.5%-level is marked by the shading. Zonal mean values of the seasonal mean sea-level pressure for the first (c) and the second period of the experiment (d). The significance of the differences of the zonal mean values between TSL and GHG at the 97.5%-level is indicated by the bars at the bottom of the respective figures.

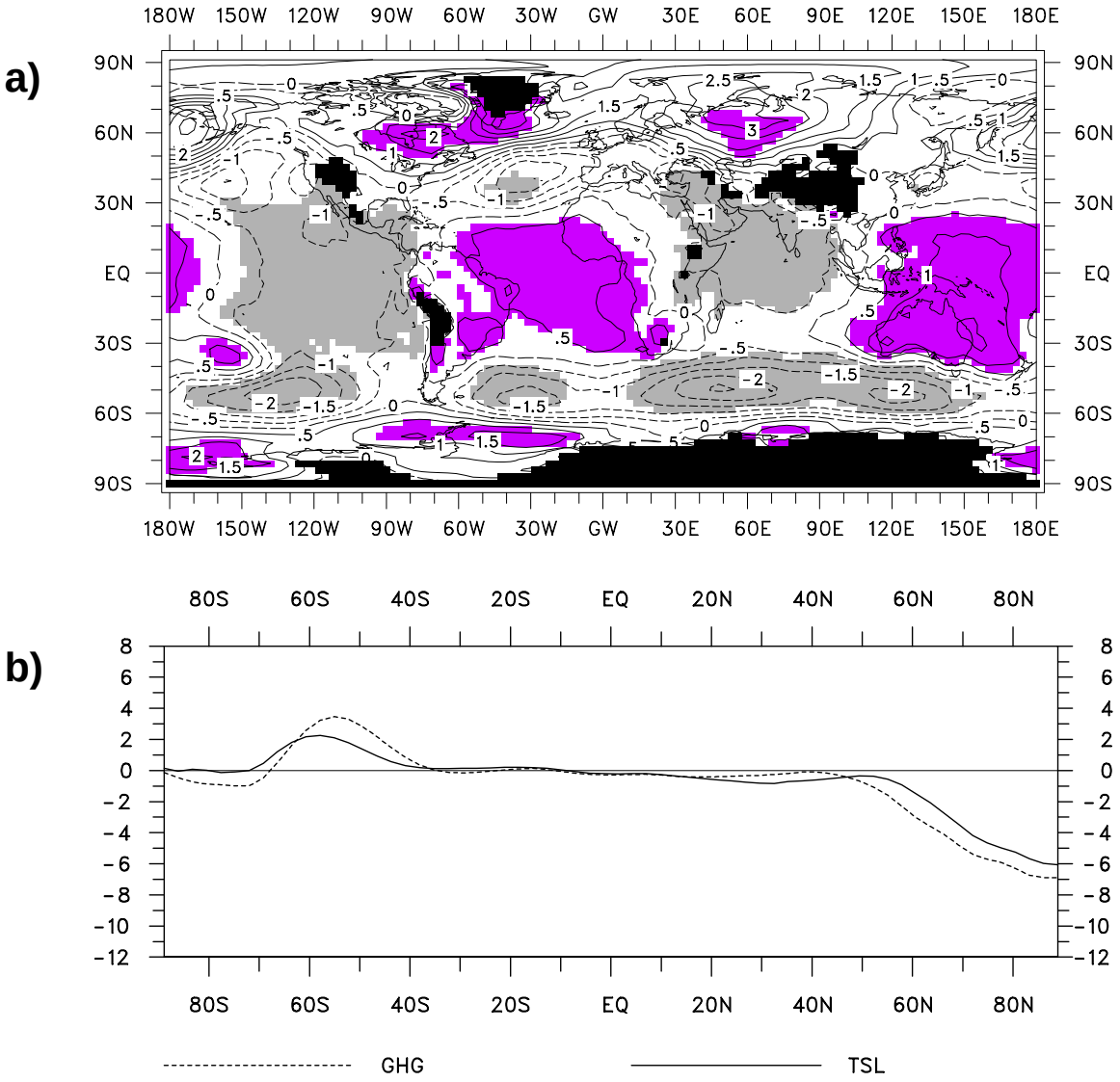

Fig. 18: Difference of the climate change signals for the seasonal mean sea-level pressure between TSL and GHG (a). Units are [hPa], the contour interval is 0.5 hPa. The significance at the 97.5%-level is marked by the shading. Climate change signals for the zonal mean values of the seasonal mean sea-level pressure for TSL and GHG (b).

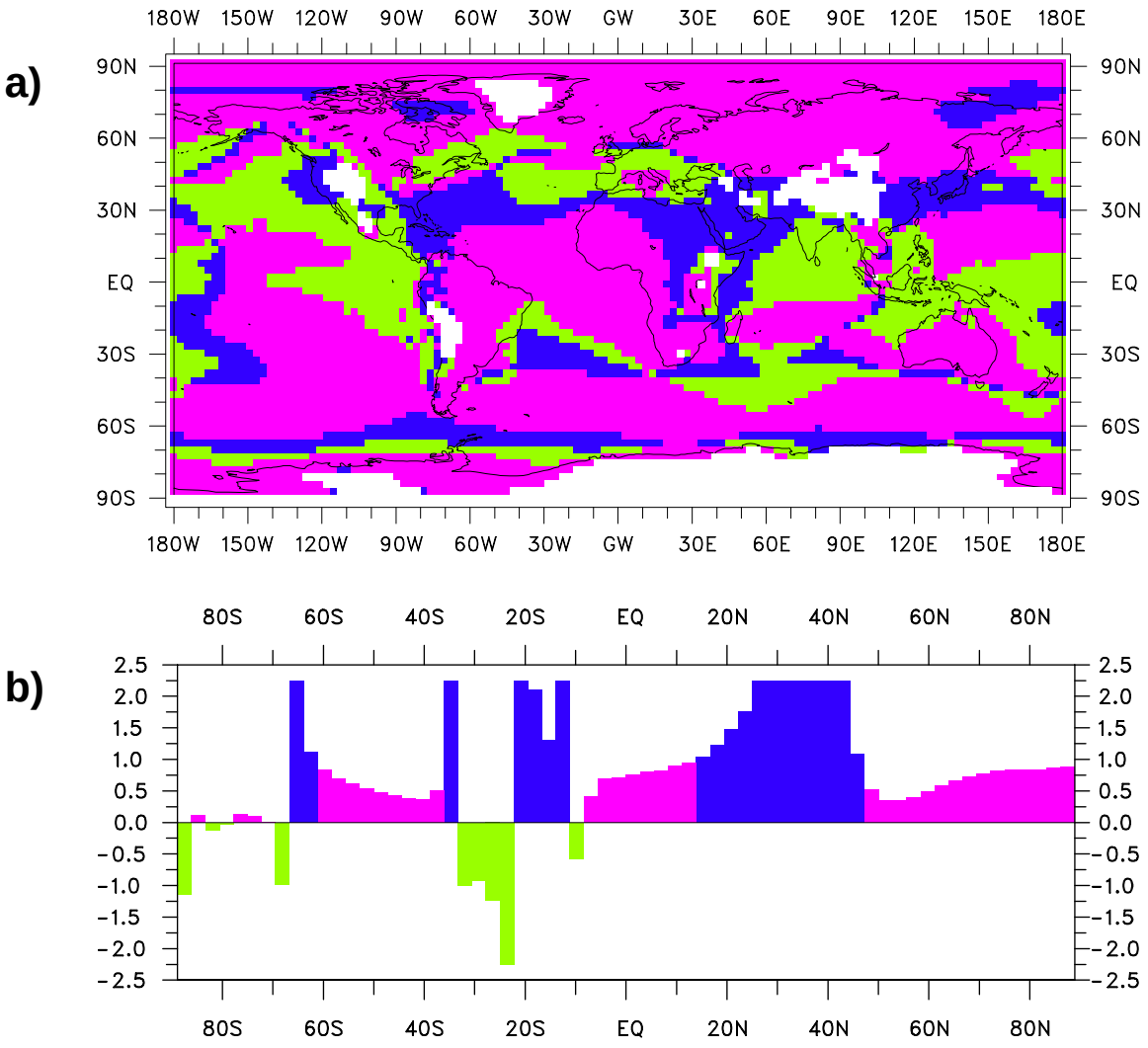

Fig. 19: Ratio of the climate change signals for the seasonal mean sea-level pressure between TSL and GHG (a). Areas, where the ratio exceeds a value of 1, are marked by the dark shading, areas, where the ratio is between 0 and 1 and where it is negative, are indicated by the medium and the light shading, respectively. Ratio of the climate change signals for the zonal mean values of the seasonal mean sea-level pressure (b). Values exceeding ±2.25 are set to 2.25.

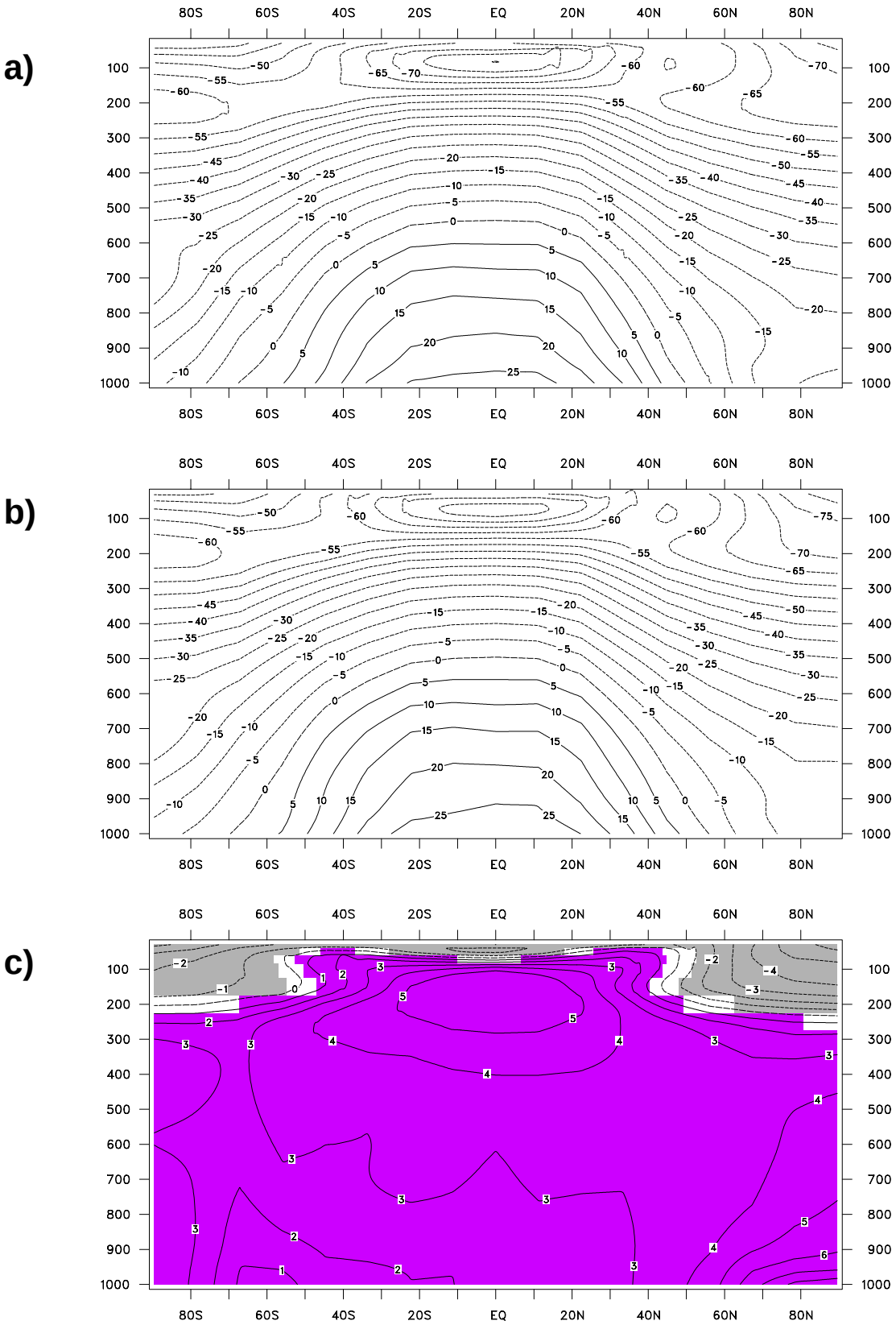

Fig. 20: Zonal mean values of the seasonal mean temperature as a function of height (hPa) and latitude for TSL-1 (a) and TSL-2 (b). Units are [°C], the contour interval is 5 °C. Difference of the zonal mean values of the seasonal mean temperature (c). The contour interval is 1 °C. The significance at the 99.9%-level is marked by the shading.

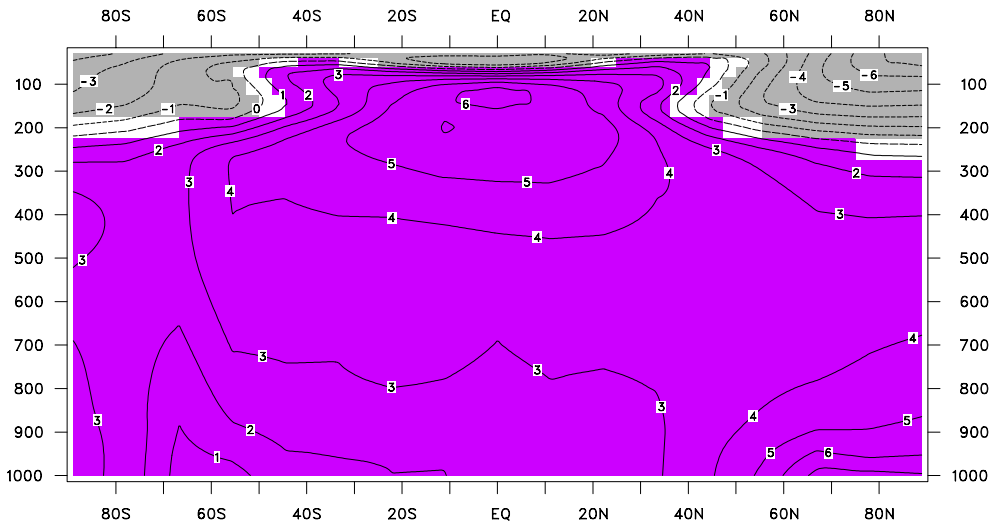

Fig. 21: As Fig. 20c, but for GHG.

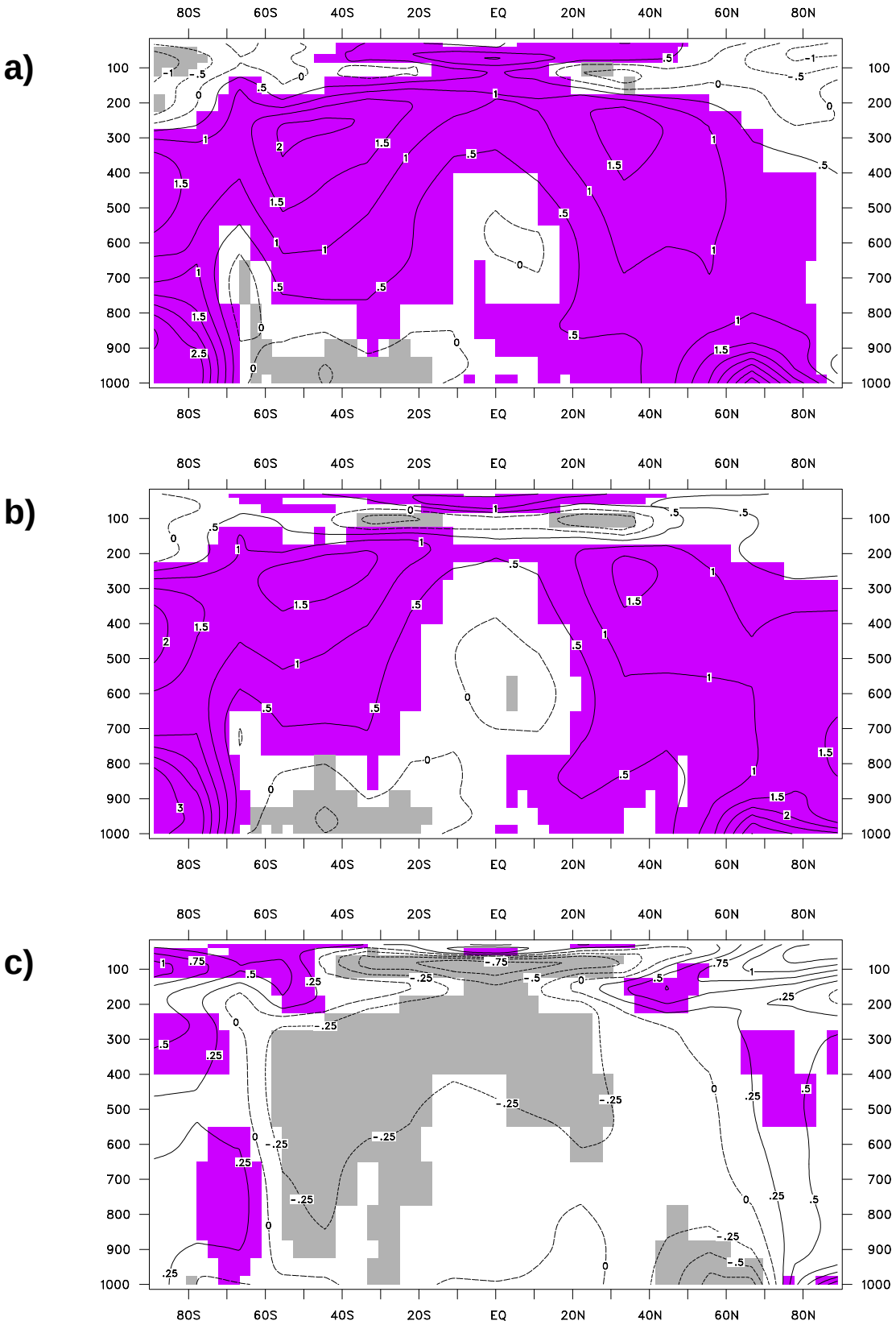

Fig. 22: Difference of the zonal mean values of the seasonal mean temperature between TSL and GHG for the first (a) and the second period of the experiment (b). Units are [°C], the contour interval is 0.5 °C. Difference of the climate change signals for the zonal mean values of the seasonal mean temperature (c). The contour interval is 0.25 °C. The significance at the 99%- (a, b) and at the 97.5-level (c), respectively, is marked by the shading.

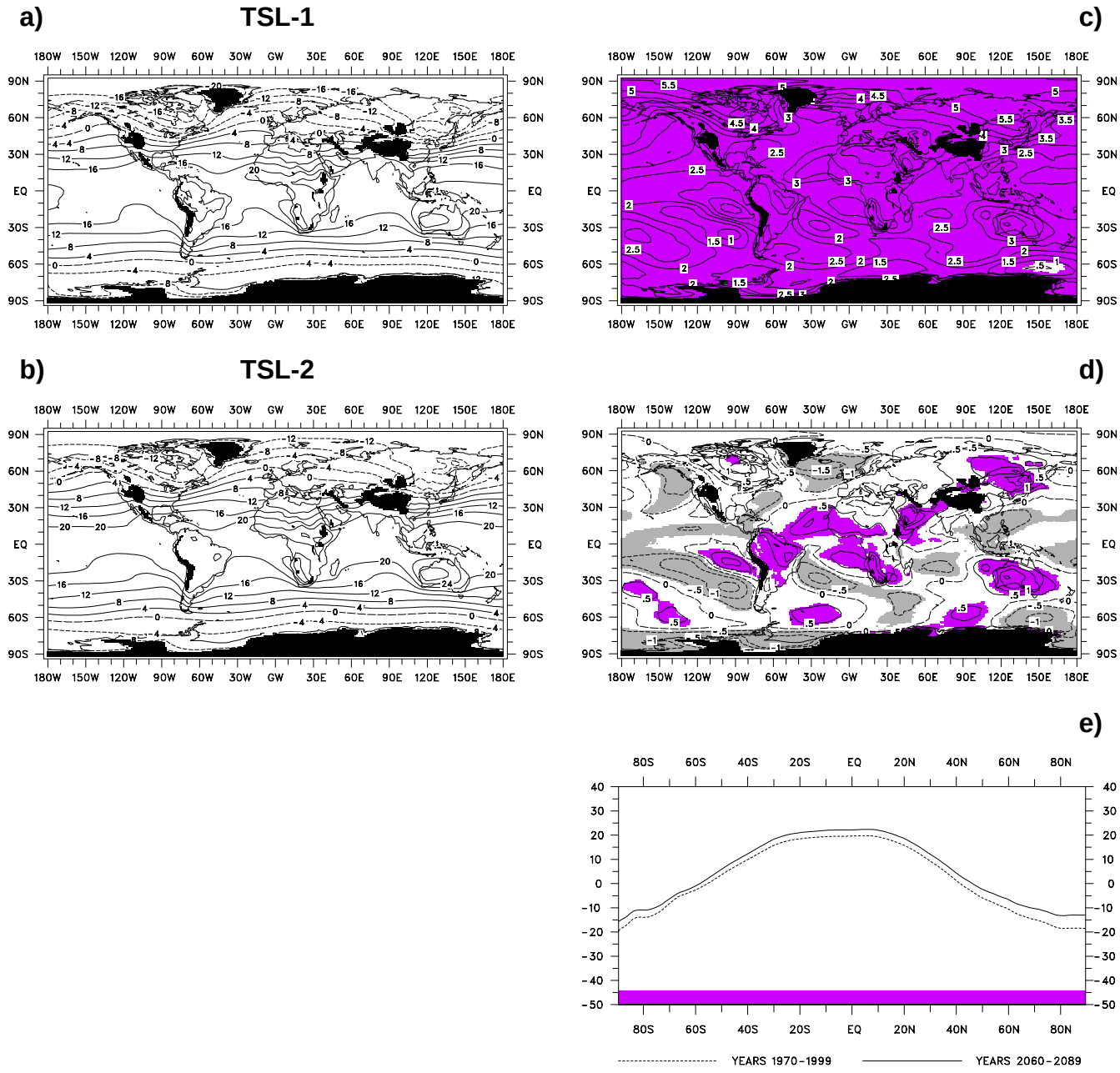

Fig. 23: Seasonal mean temperature at 850 hPa for TSL-1 (a) and TSL-2 (b). Units are [°C], the contour interval is 4 °C. Difference of the seasonal mean temperature at 850 hPa between TSL-2 and TSL-1 (c), also with the zonal mean values removed (d). The contour interval is 0.5 °C. The significance at the 99.9%- (c) and at the 99%-level (d), respectively, is marked by the shading. Zonal mean values of the seasonal mean temperature at 850 hPa for TSL-1 and TSL-2 (e). The significance of the differences of the zonal mean values between TSL-2 and TSL-1 at the 99.9%-level is indicated by the bars at the bottom of the respective figure.

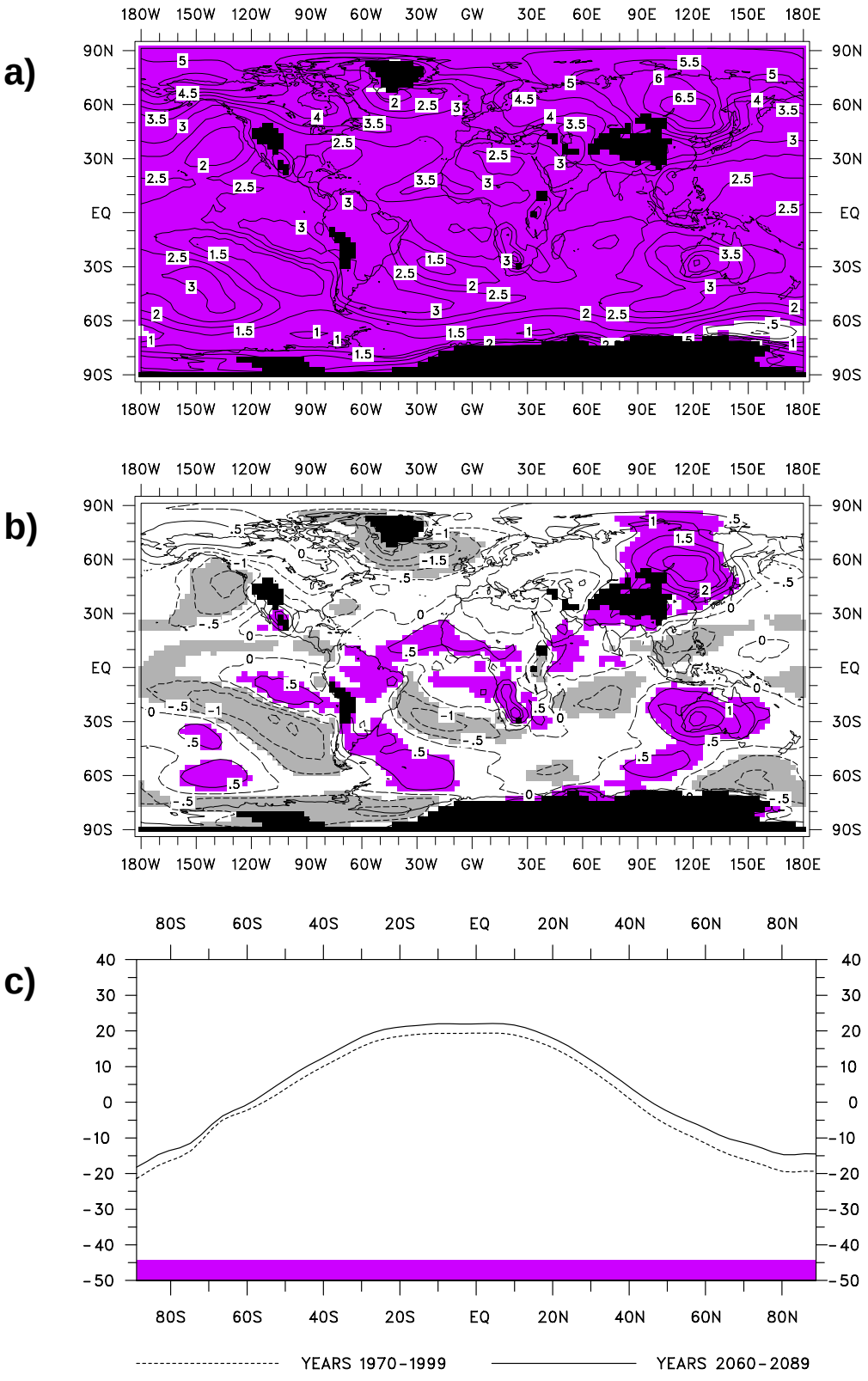

Fig. 24: As Figs. 23c-e, but for GHG.

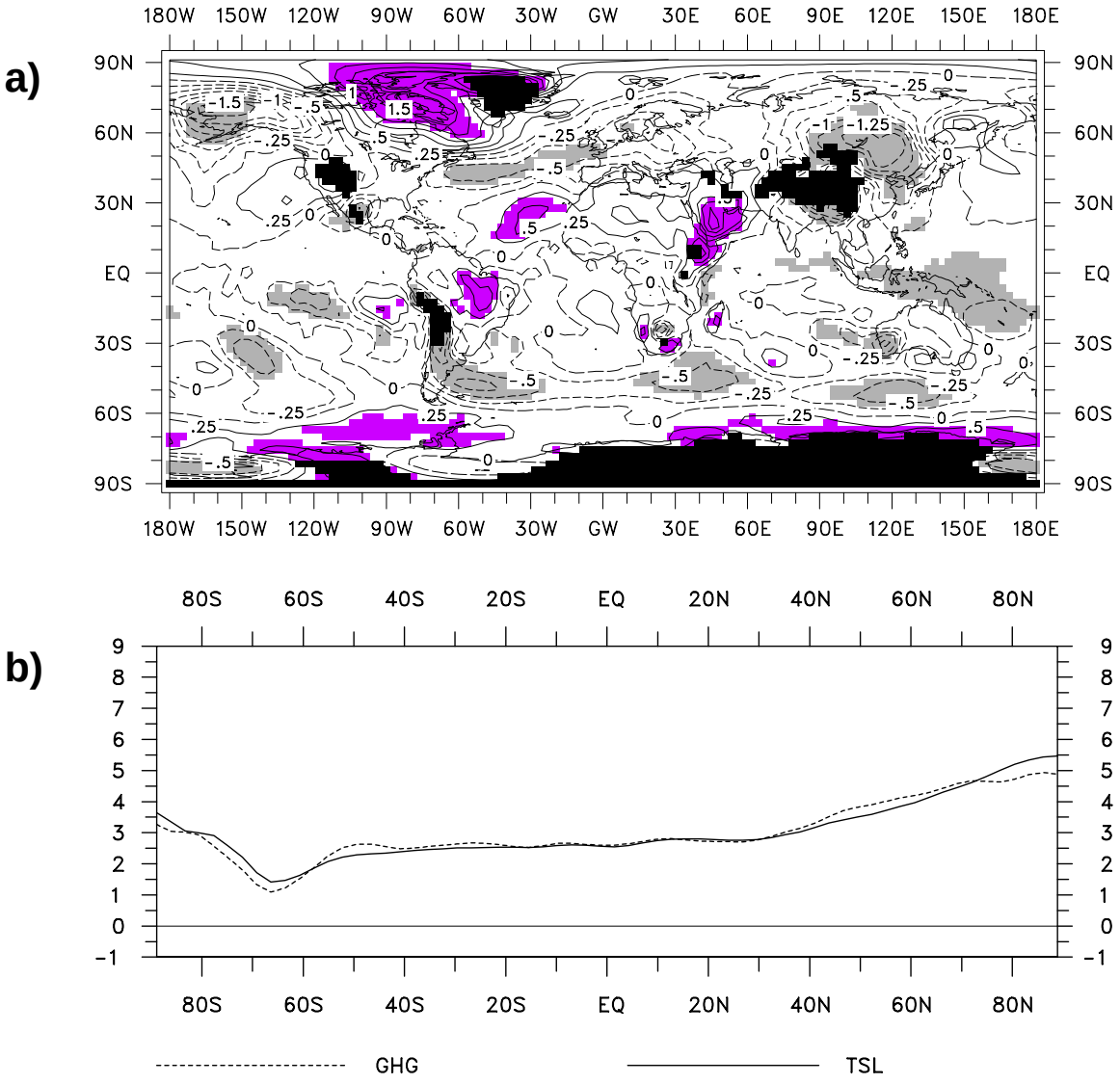

Fig. 25: As Fig. 18, but for the temperature at 850 hPa. Units are [°C], the contour interval is 0.25 °C.

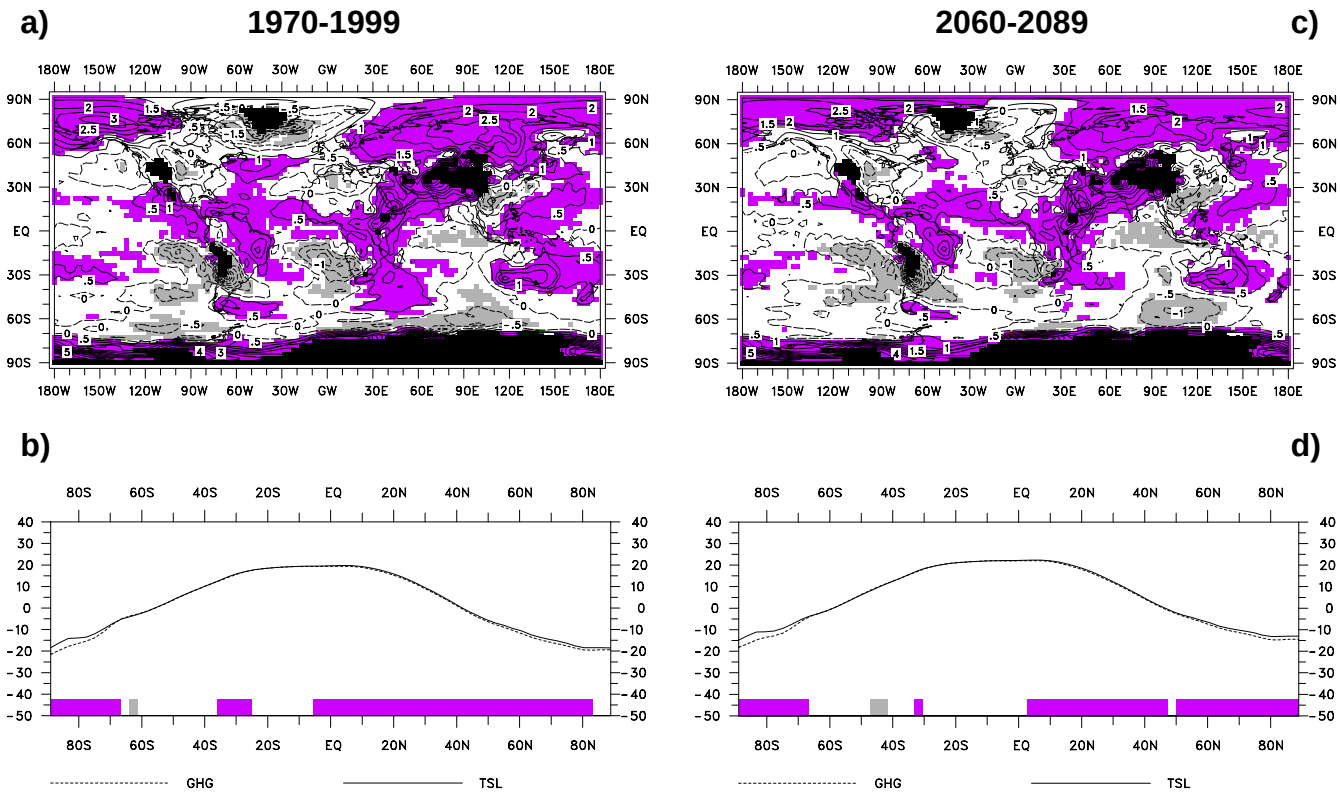

Fig. 26: As Fig. 17, but for the temperature at 850 hPa. Units are [°C], the contour interval is 0.5 °C. The significance at the 97.5%-level is marked by the shading (a, c), and the significance of the differences of the zonal mean values at the 99%-level is indicated by the bars at the bottom of the respective figures (b, d).

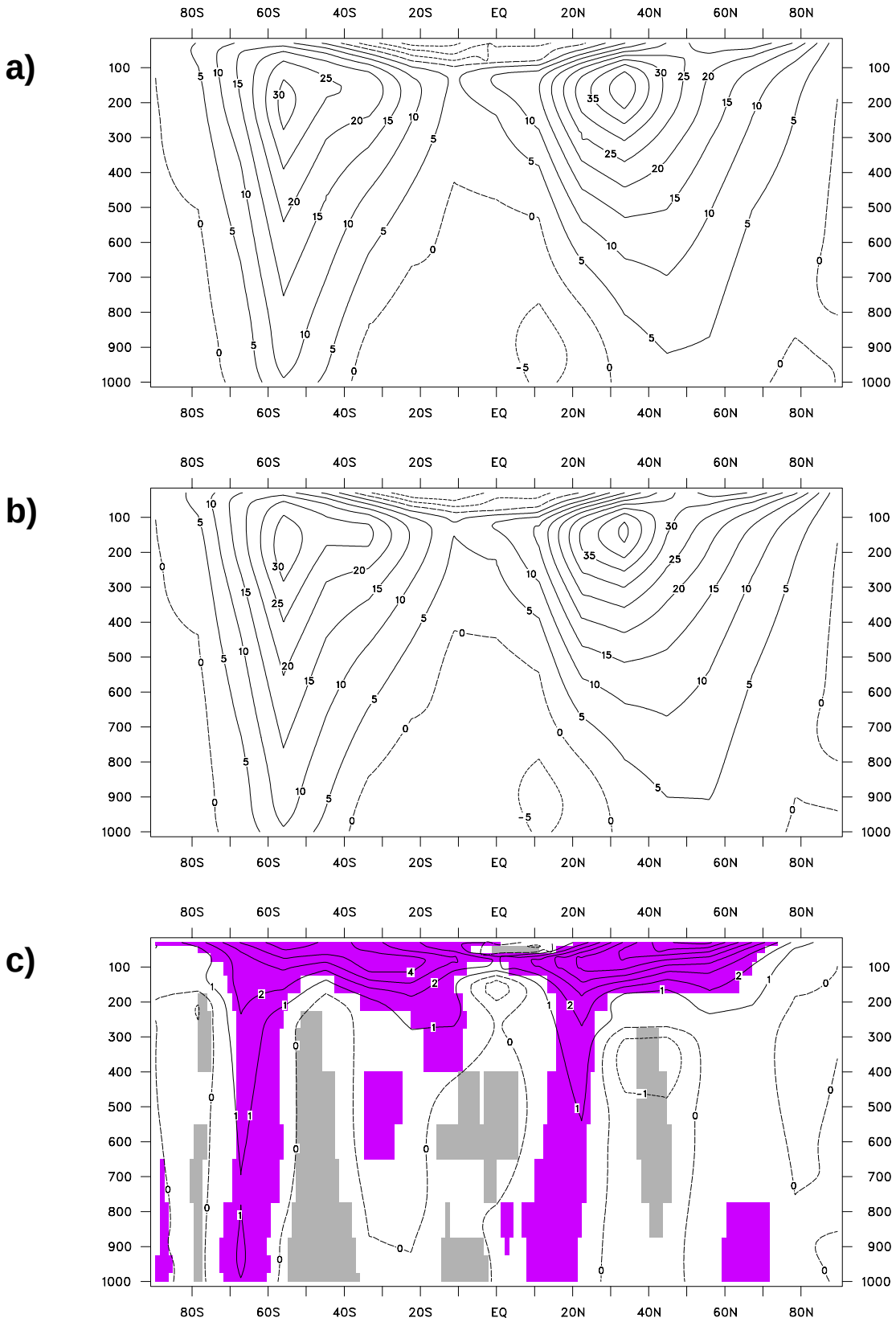

Fig. 27: As Fig. 20, but for the zonal wind component. Units are [m/s], the contour interval is 5 m/s (a, b) and 1 m/s (c), respectively. The significance at the 99%-level is marked by the shading.

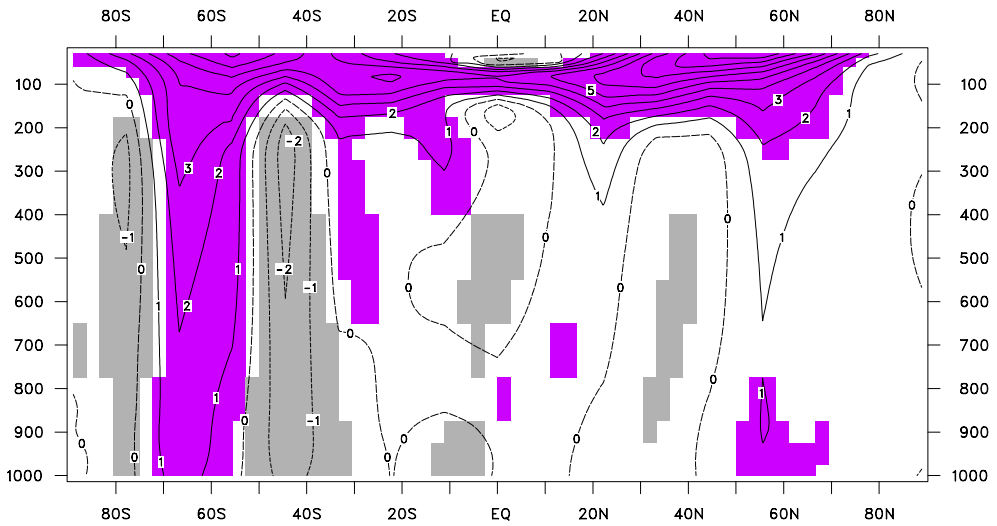

Fig. 28: As Fig. 27c, but for GHG.

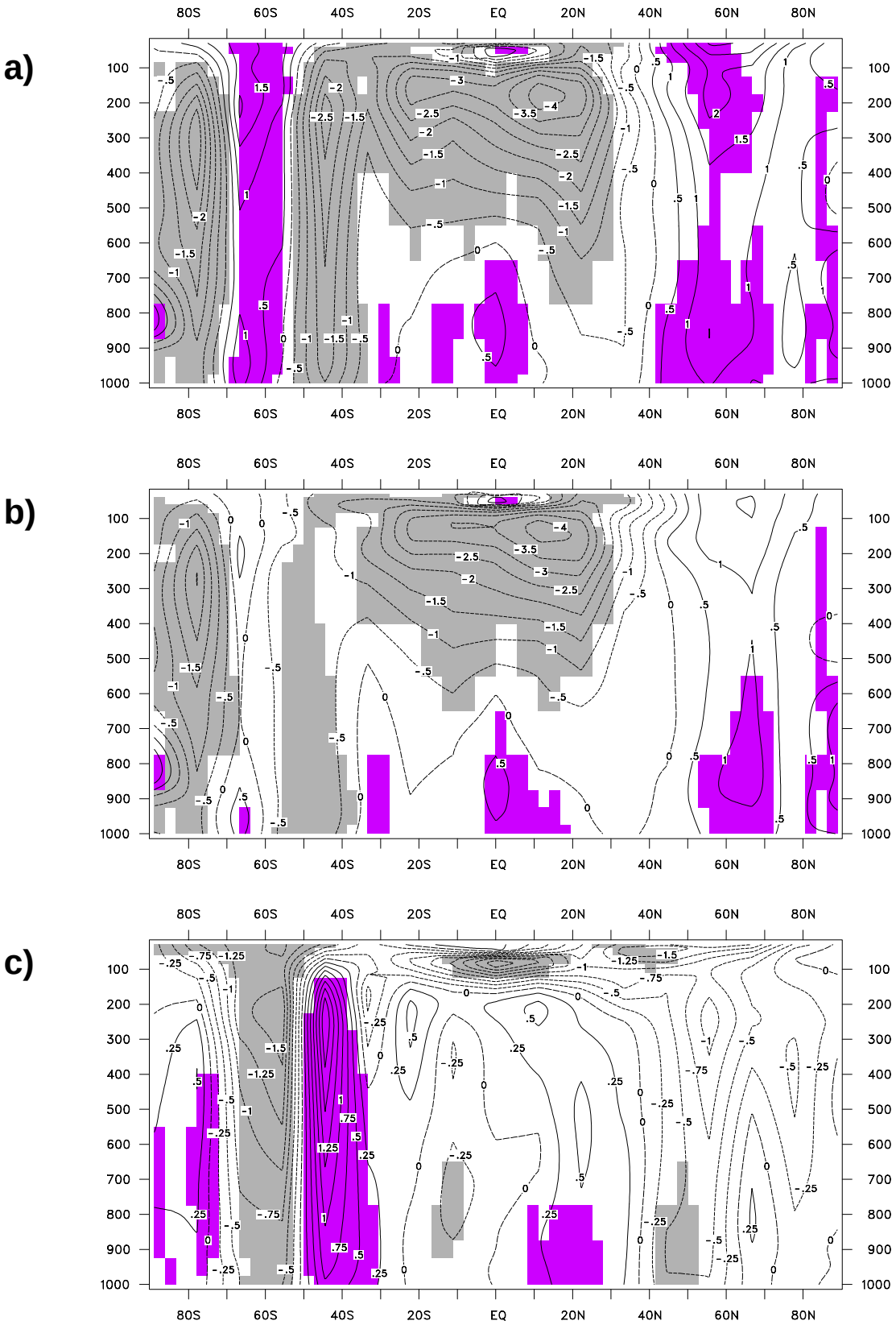

Fig. 29: As Fig. 22, but for the zonal wind component. Units are [m/s], the contour interval is 0.5 m/s (a, b) and 0.25 m/s (c), respectively.

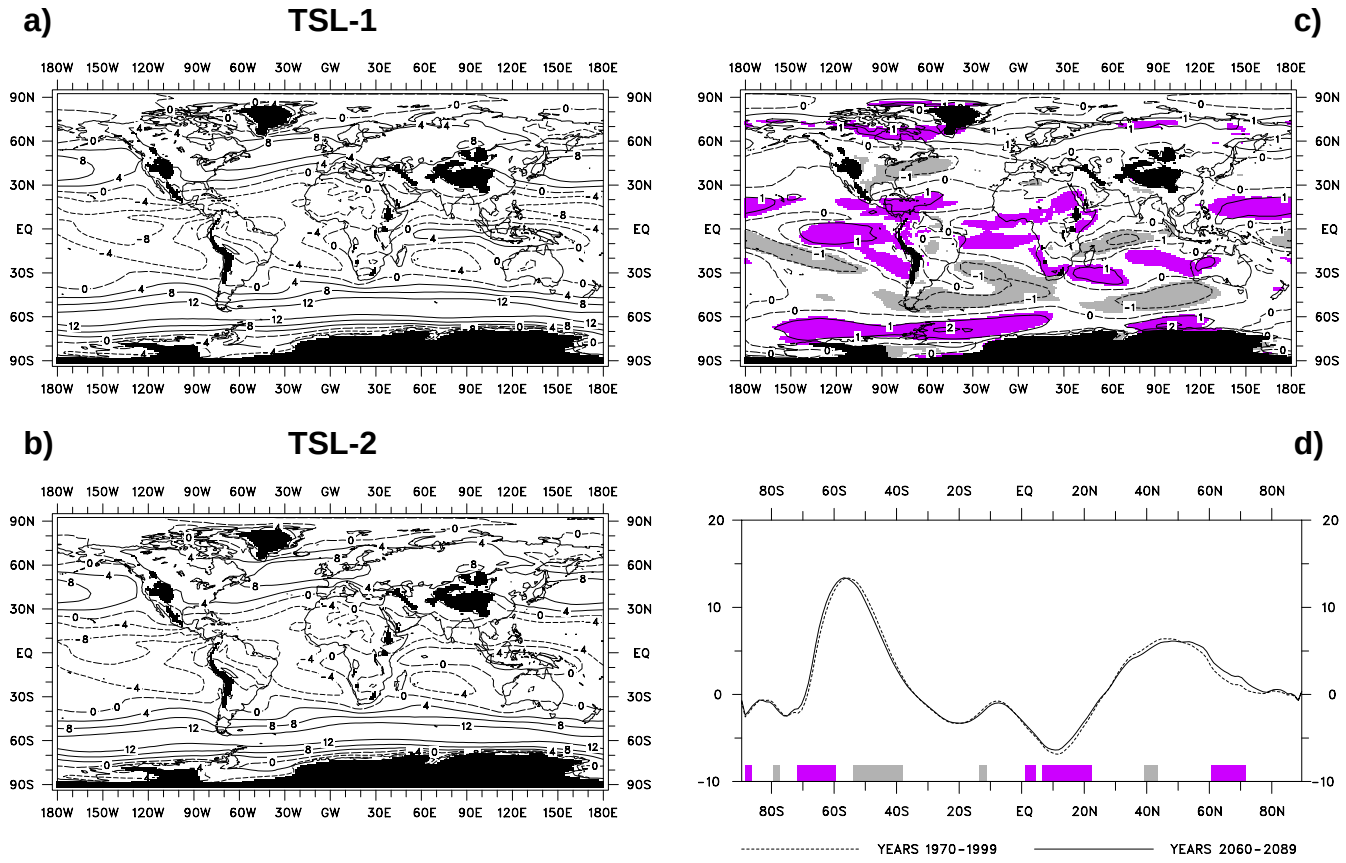

Fig. 30: As Fig. 15, but for the zonal wind component at 850 hPa. Units are [m/s], the contour interval is 4 m/s (a, b) and 1 m/s (c), respectively.

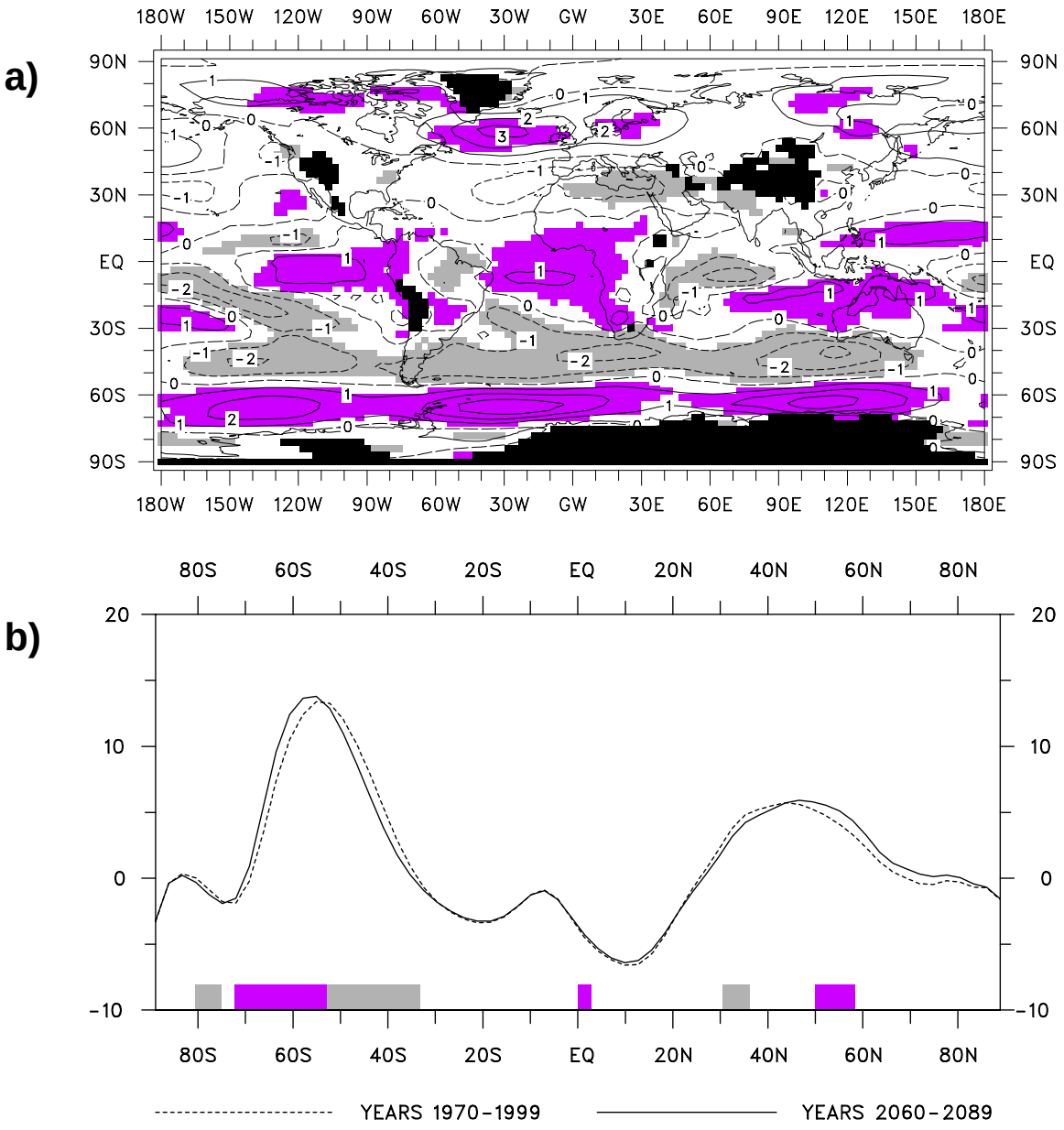

Fig. 31: As Figs. 30c, d, but for GHG.

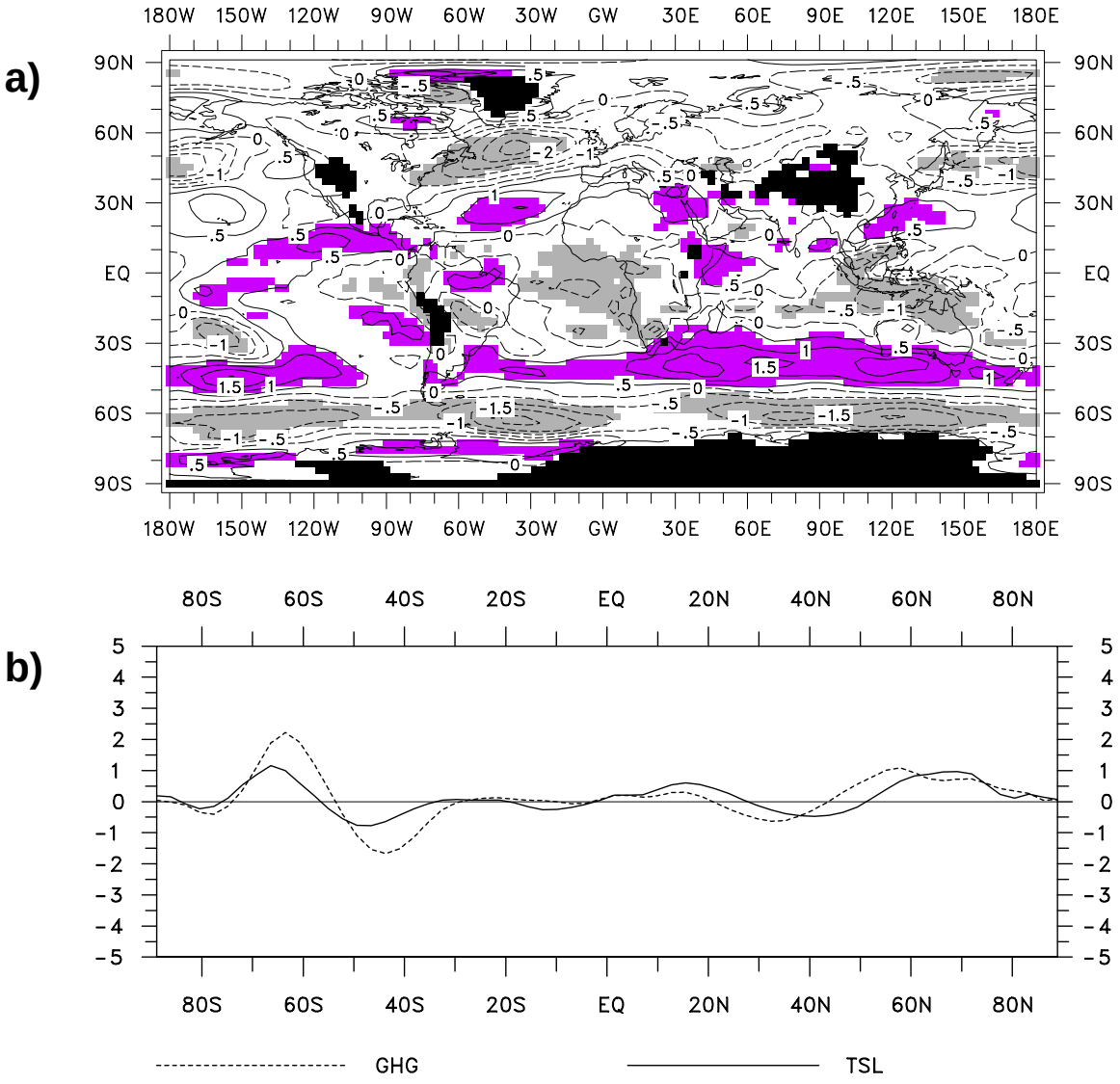

Fig. 32: As Fig. 18, but for the zonal wind component at 850 hPa. Units are [m/s], the contour interval is 0.5 m/s.

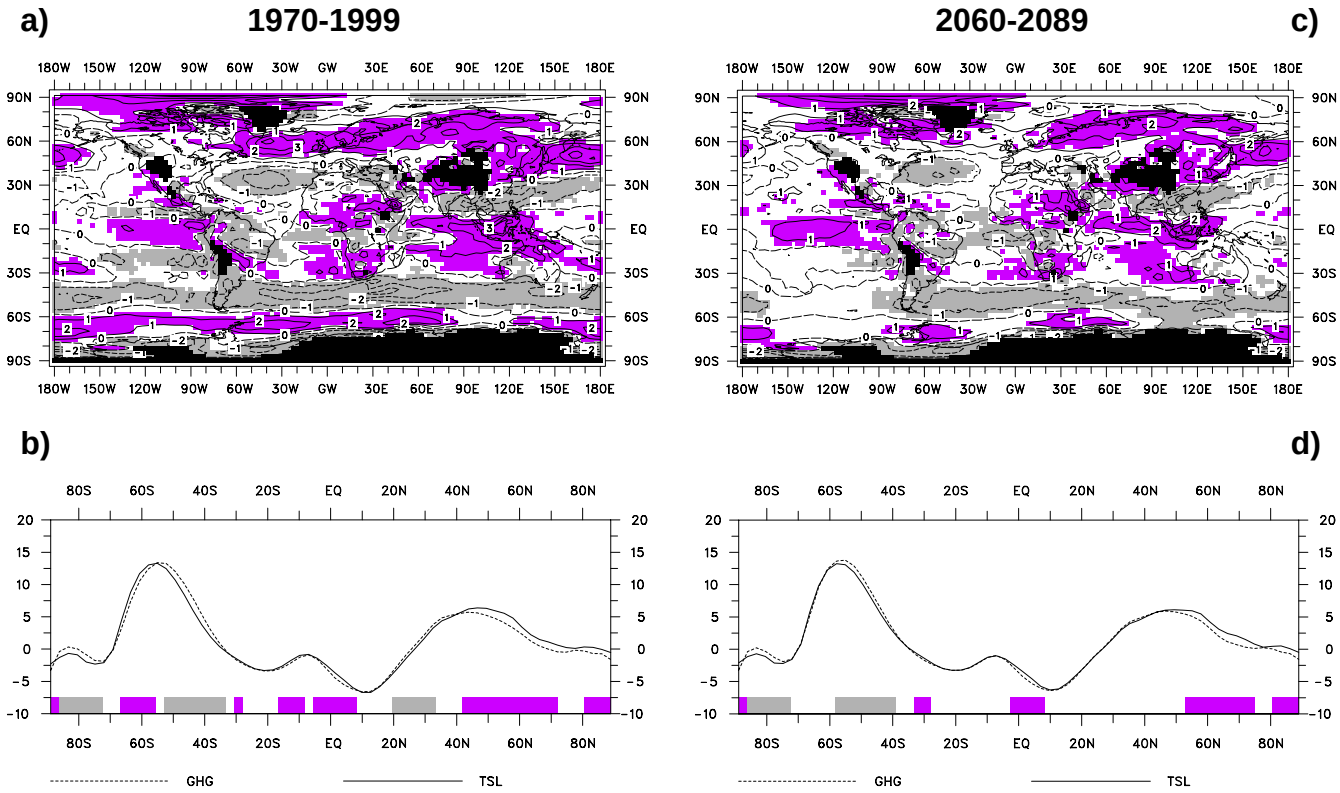

Fig. 33: As Fig. 17, but for the zonal wind component at 850 hPa. Units are [m/s], the contour interval is 1 m/s.

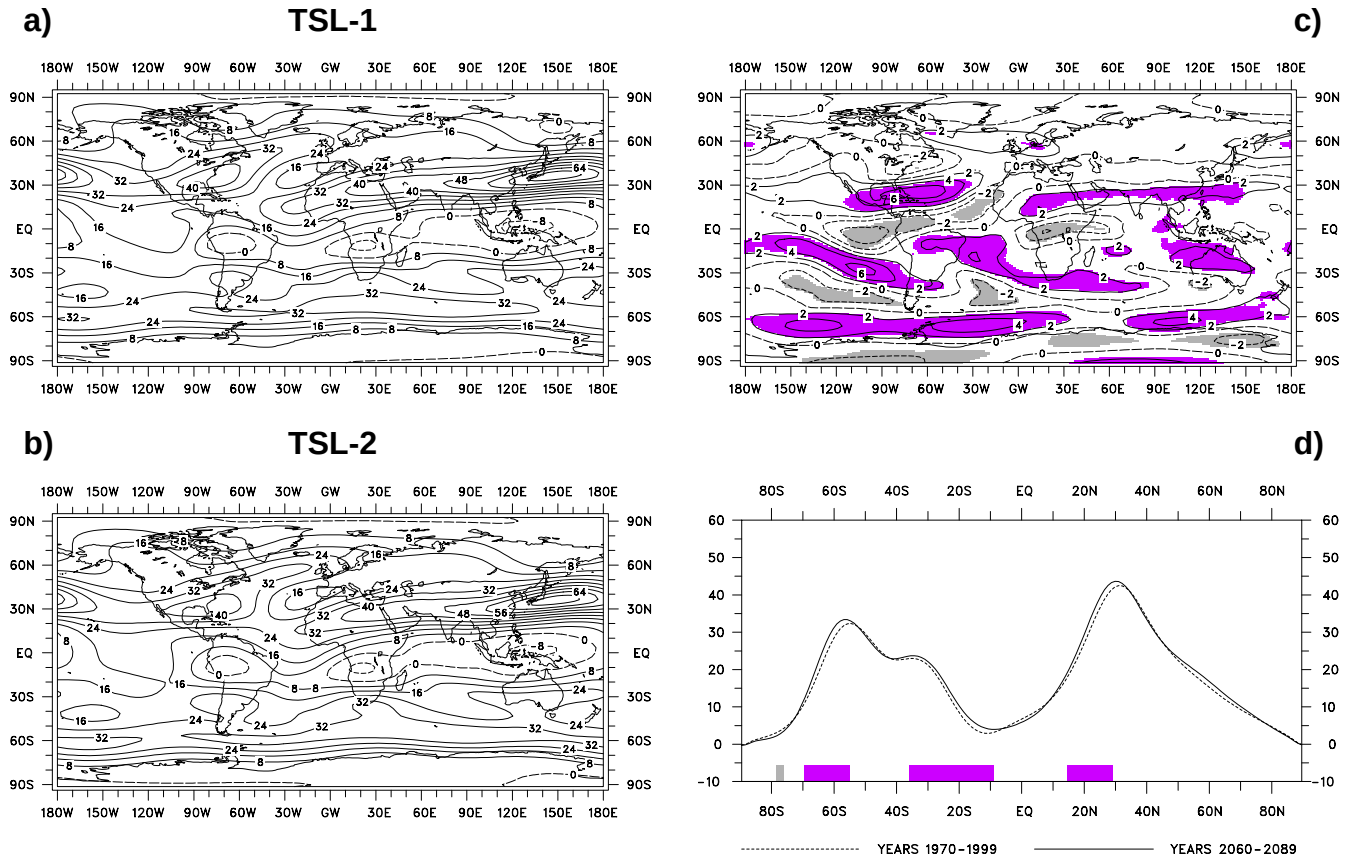

Fig. 34: As Fig. 15, but for the zonal wind component at 200 hPa. Units are [m/s], the contour interval is 8 m/s (a, b) and 2 m/s (c), respectively.

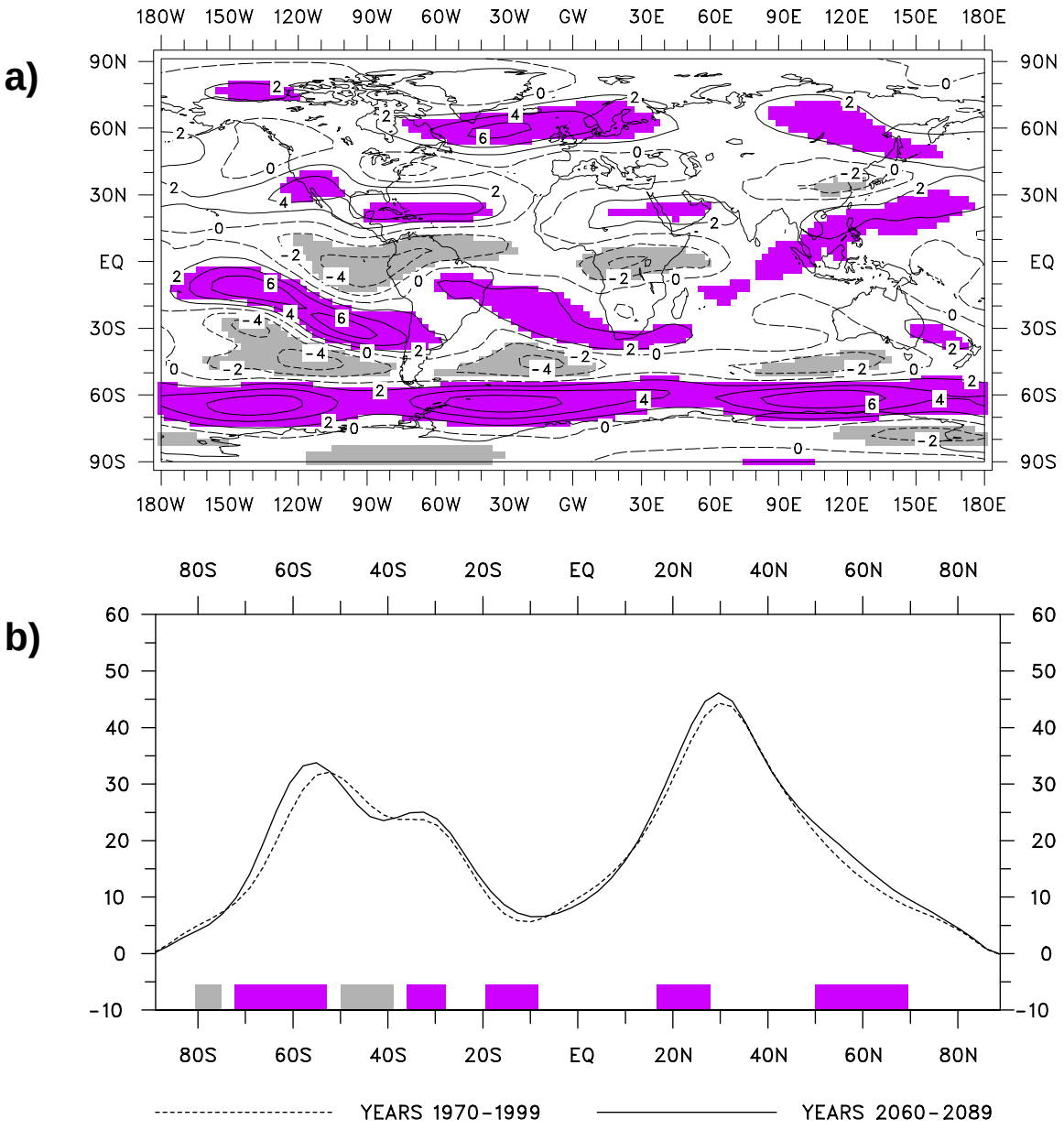

Fig. 35: As Figs. 34c, d, but for GHG.

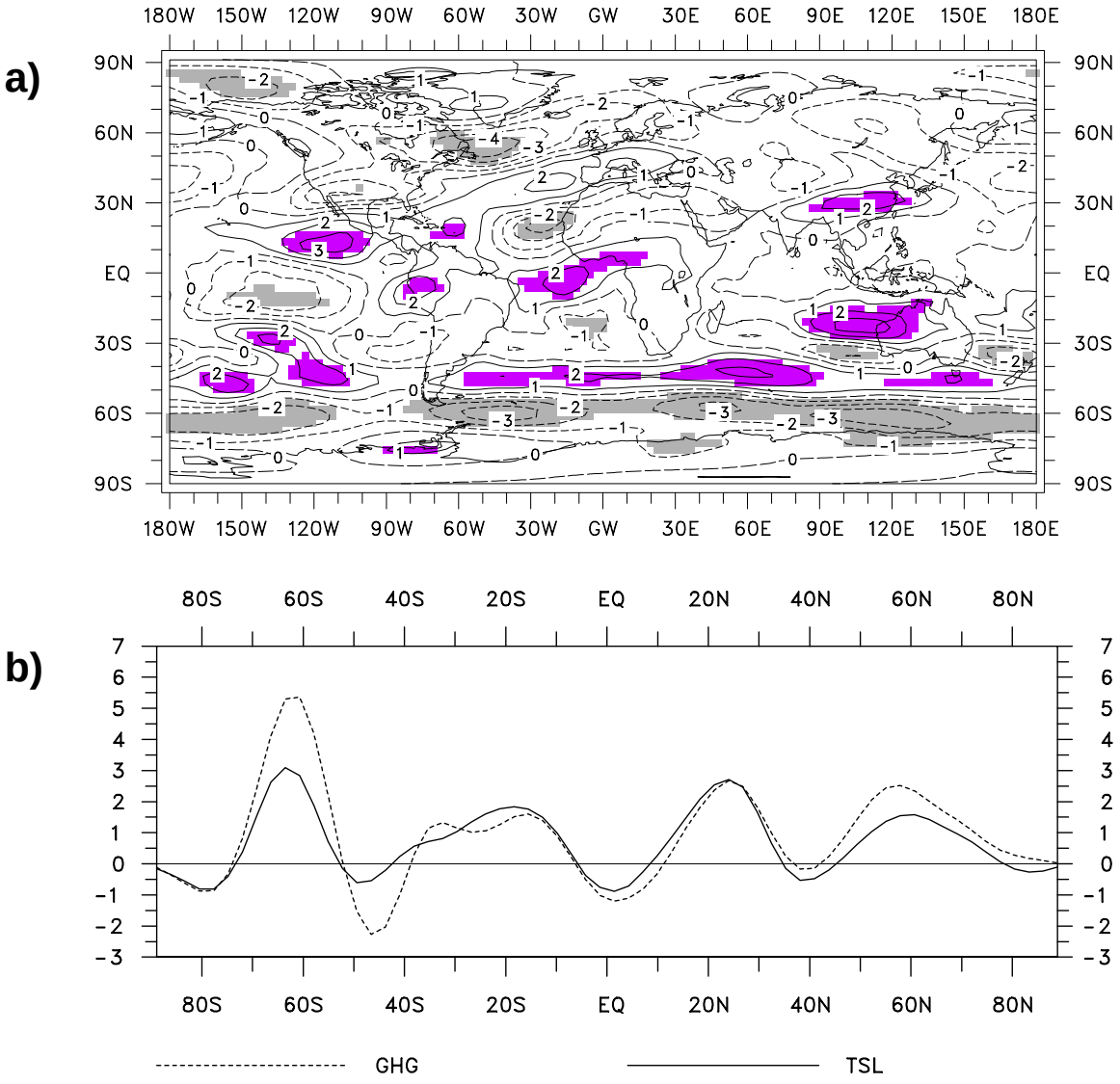

Fig. 36: As Fig. 18, but for the zonal wind component at 200 hPa. Units are [m/s], the contour interval is 1 m/s.

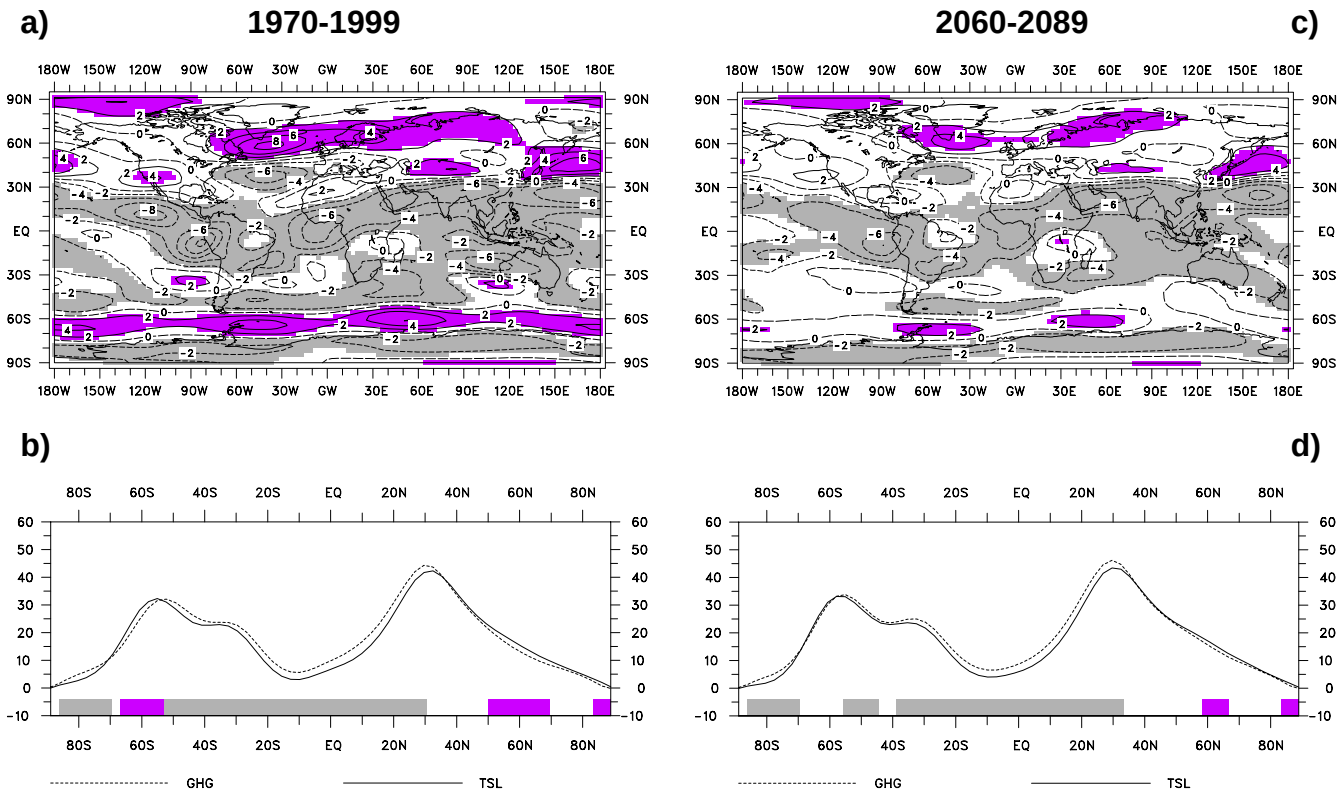

Fig. 37: As Fig. 17, but for the zonal wind component at 200 hPa. Units are [m/s], the contour interval is 2 m/s.

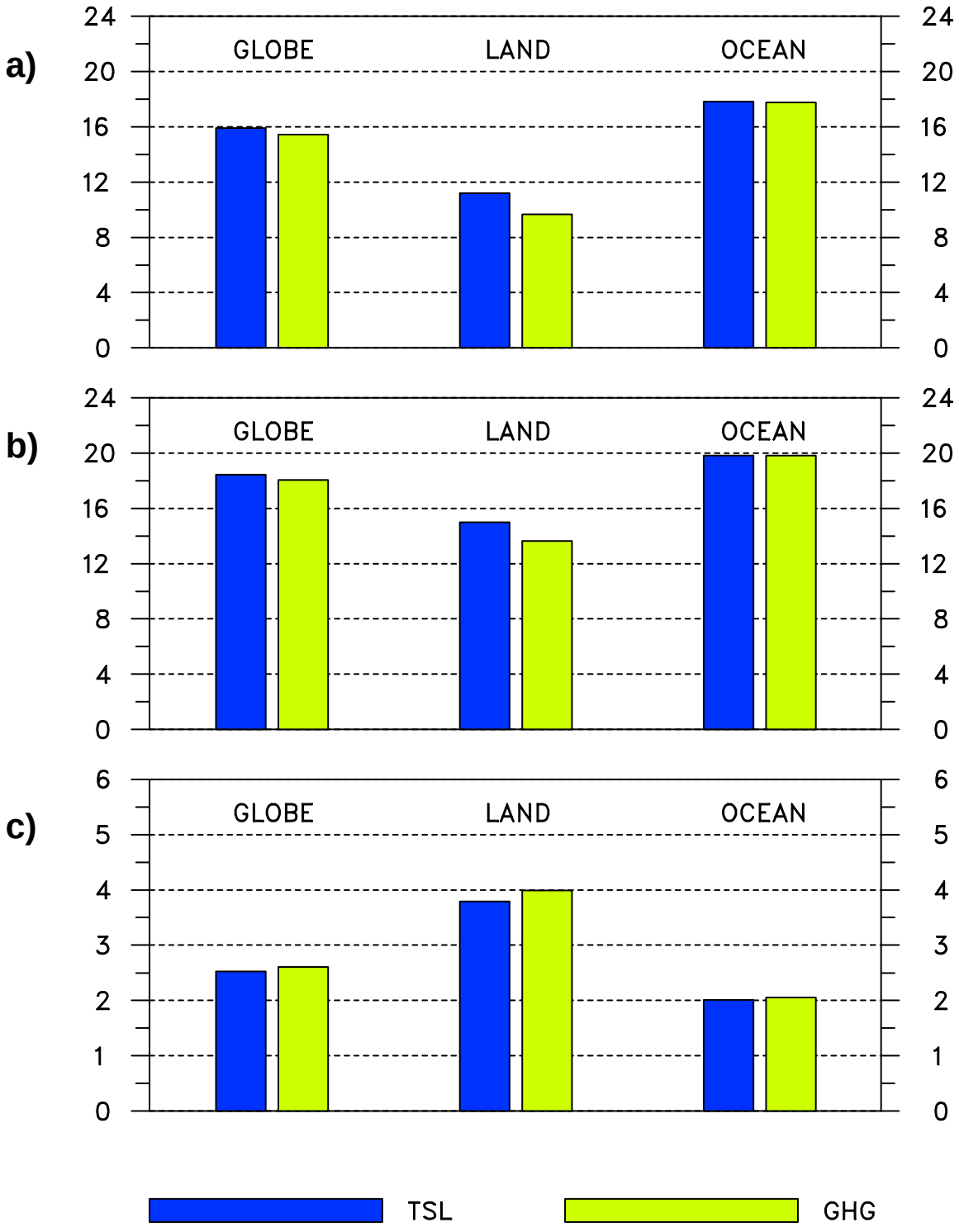

Fig. 38: Long-term annual means of the temperature in 2 m distinguishing between the whole globe, land and ocean areas for TSL and GHG for the first (a) and the second period of the experiment (b) and for the climate change signal (c). Units are [°C].

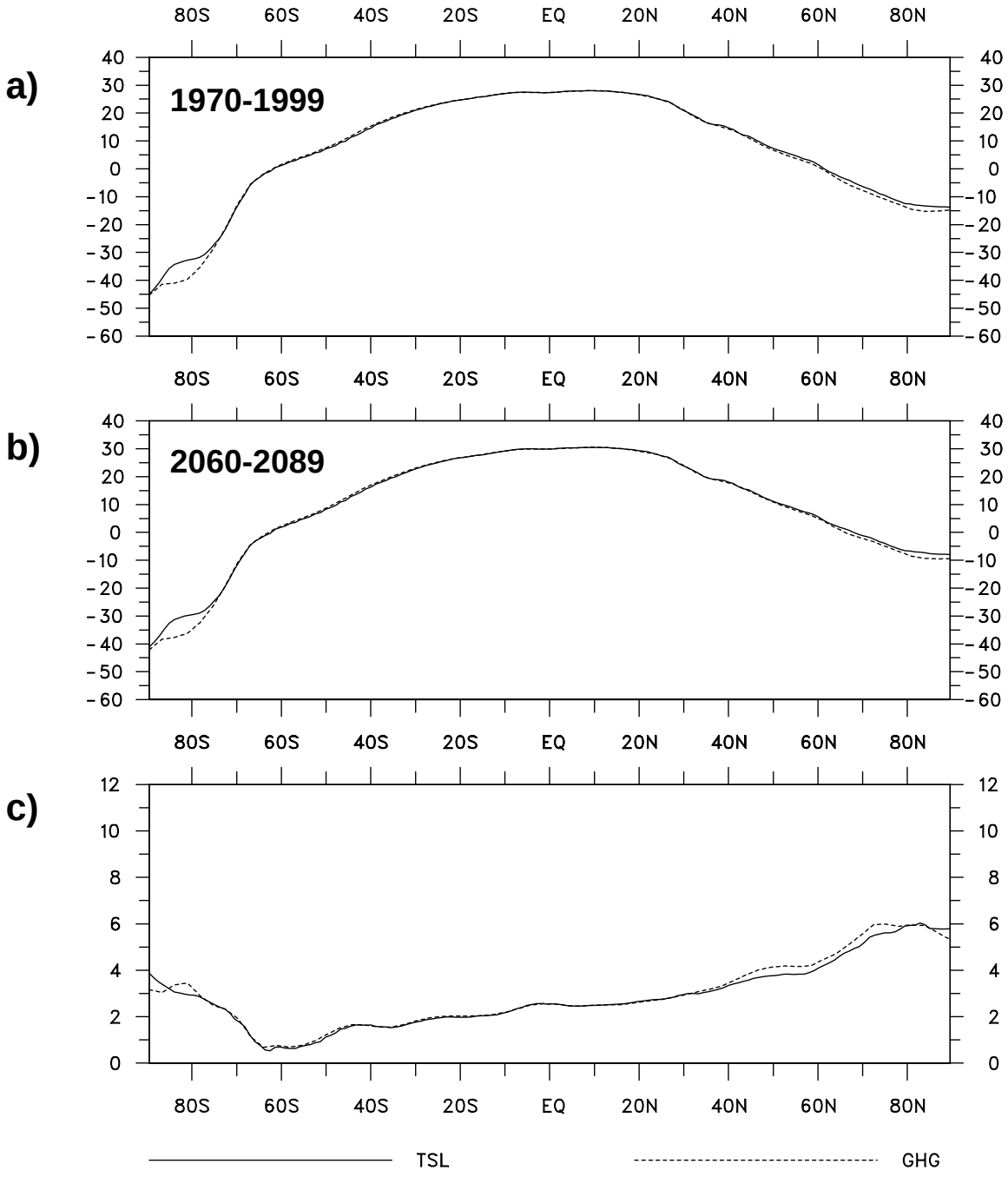

Fig. 39: Zonal mean values of the long-term annual mean temperature in 2 m for the whole globe for TSL and GHG for the first (a) and the second period of the experiment (b) and for the climate change signal (c). Units are [°C].

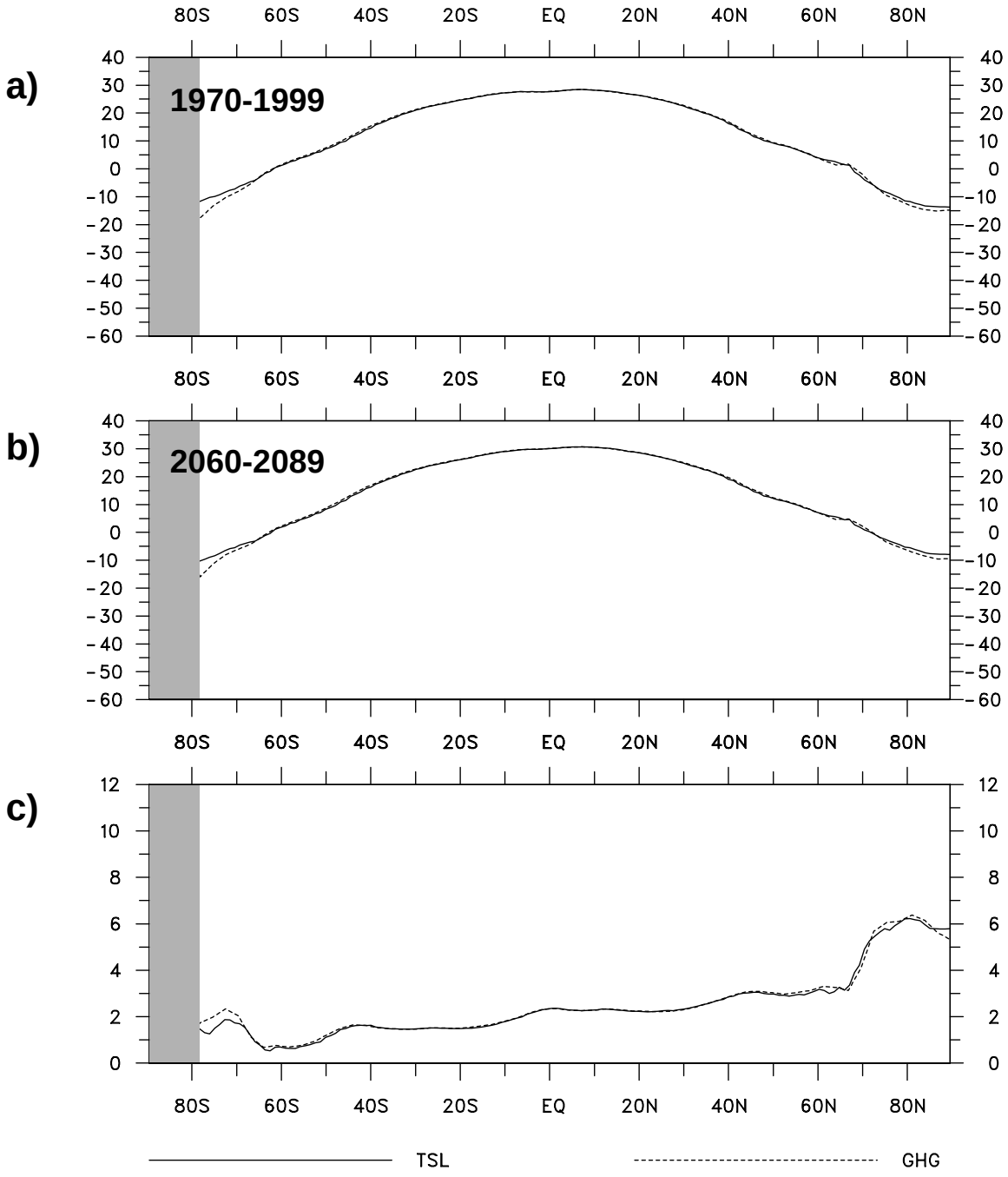

Fig. 40: As Fig. 39, but for the ocean areas only.

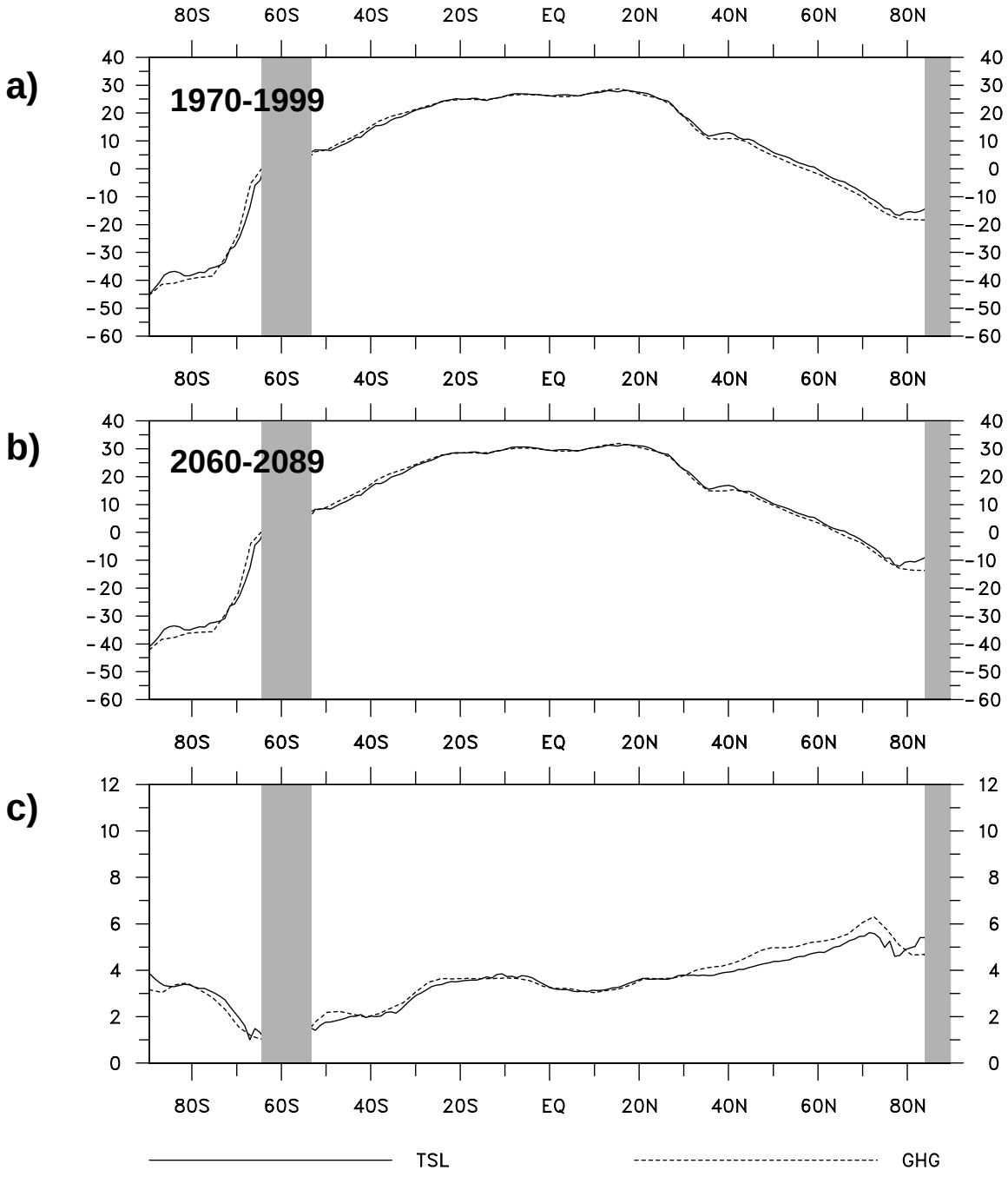

Fig. 41: As Fig. 39, but for the land areas only.

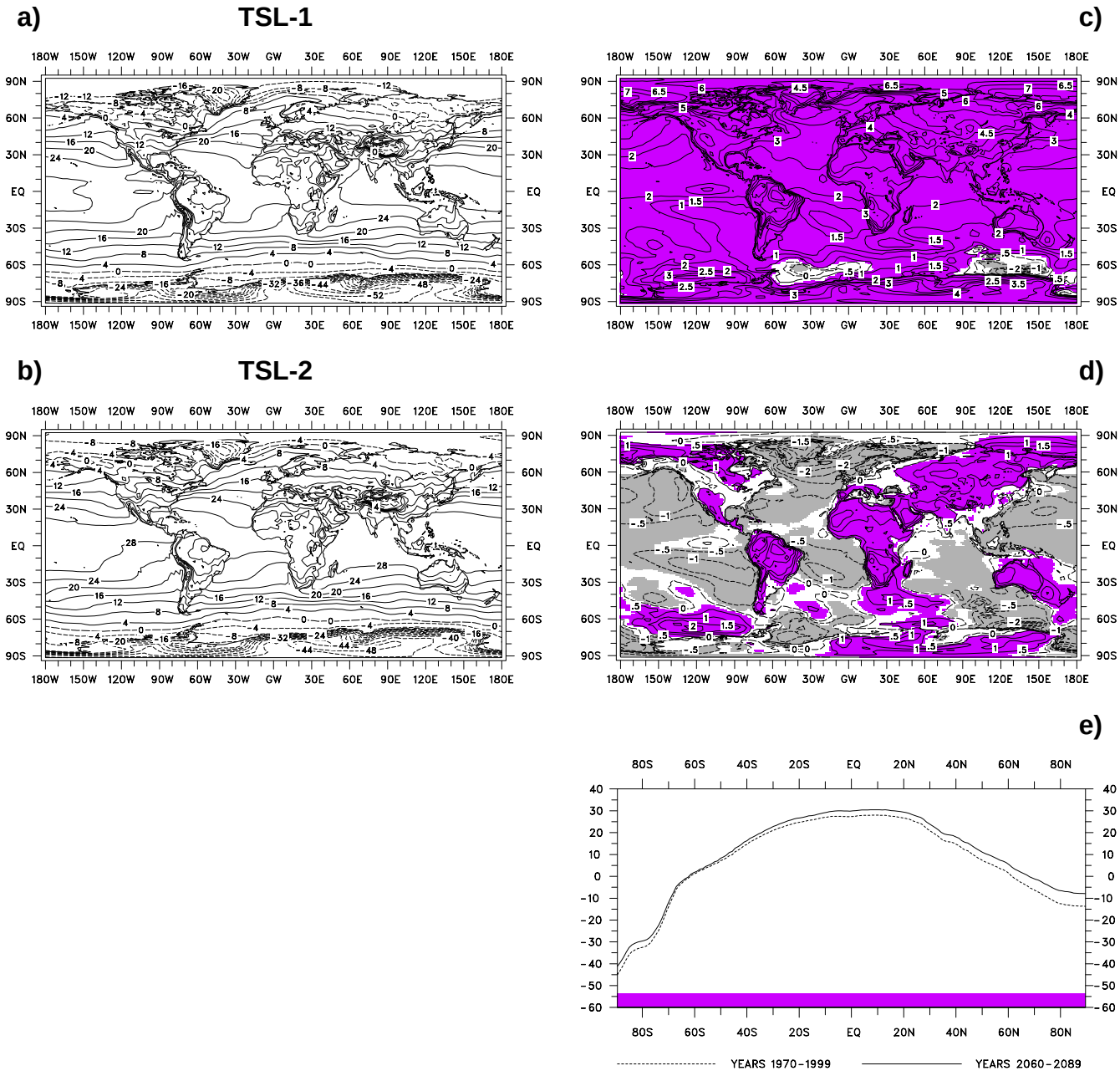

Fig. 42: As Fig. 23, but for the annual mean temperature in 2 m.

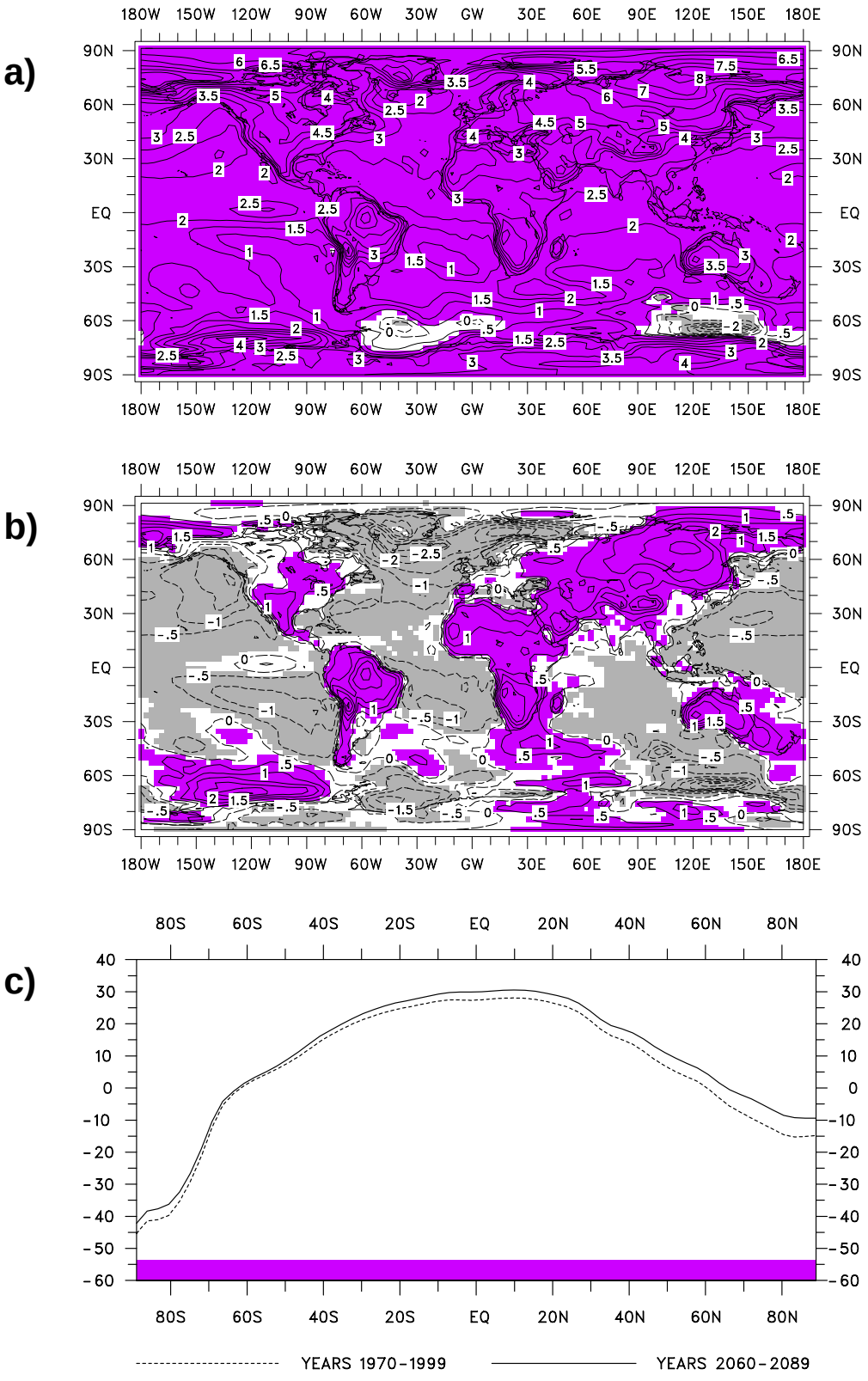

Fig. 43: As Figs. 42c-e, but for GHG.

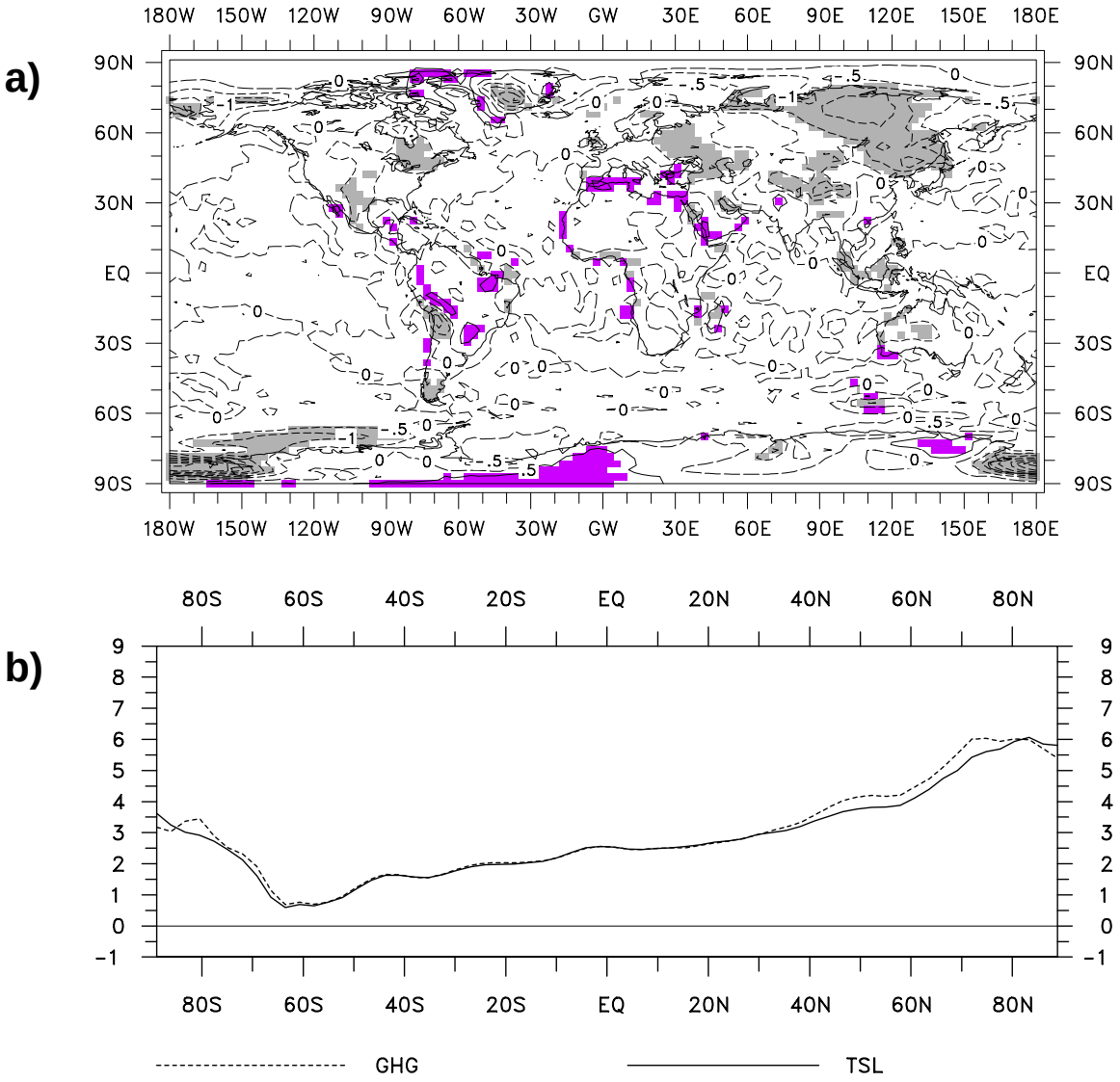

Fig. 44: As Fig. 18, but for the annual mean temperature in 2 m. Units are [°C], the contour interval is 0.5 °C.

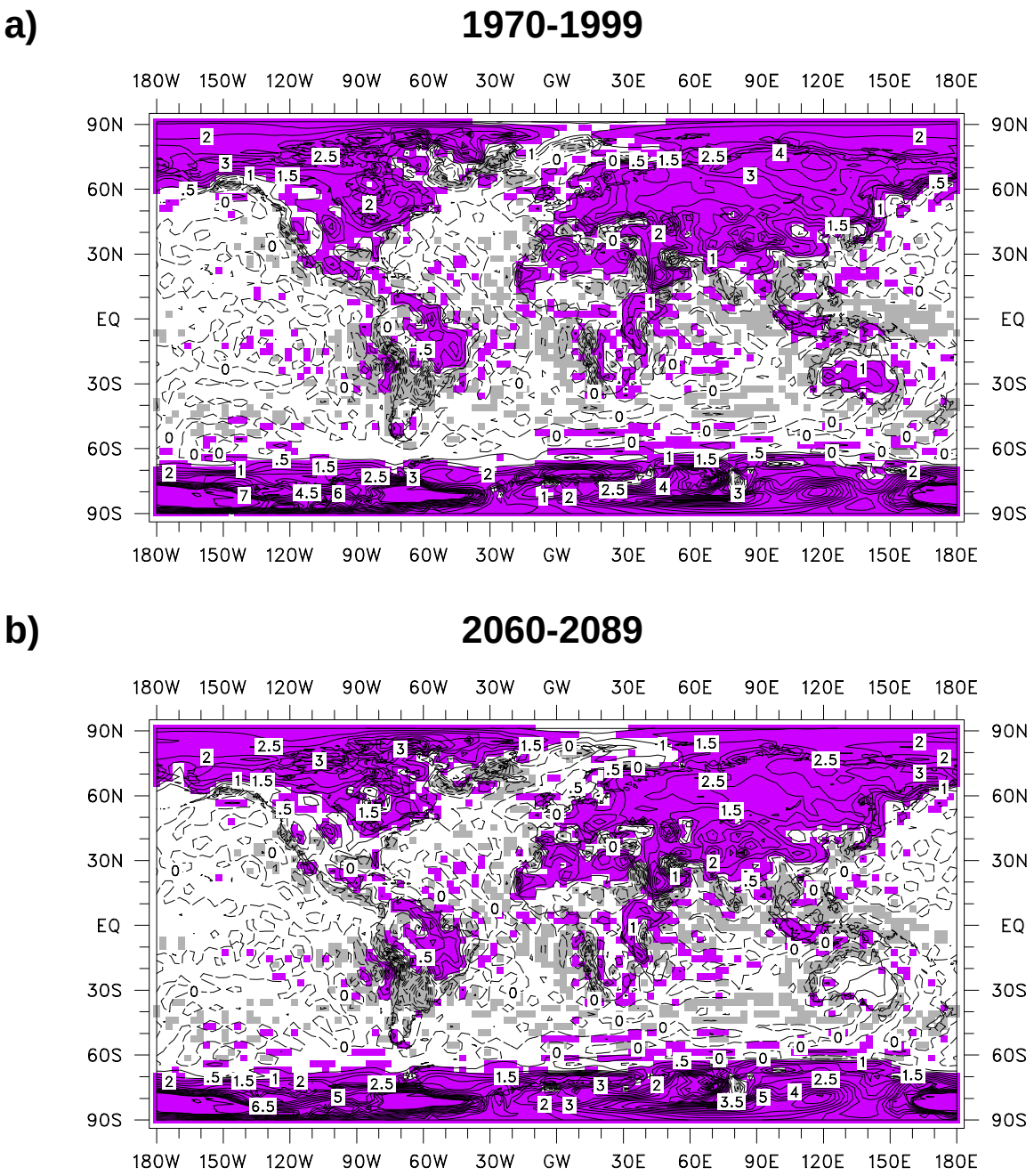

Fig. 45: As Fig. 26a, c, but for the annual mean temperature in 2 m.

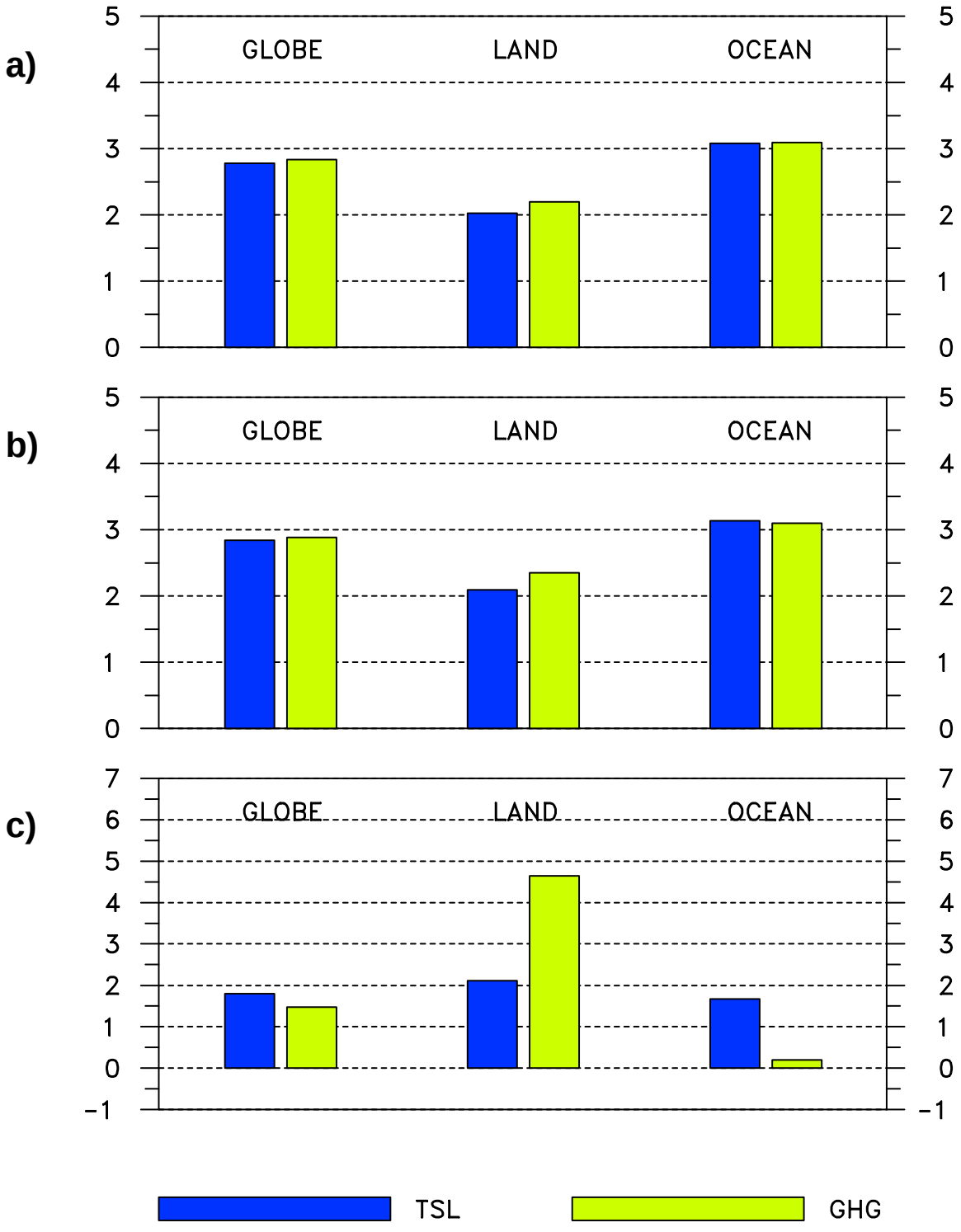

Fig. 46: As Fig. 38, but for daily precipitation. Units are [mm/day] (a, b) and [mm/month] (c), respectively.

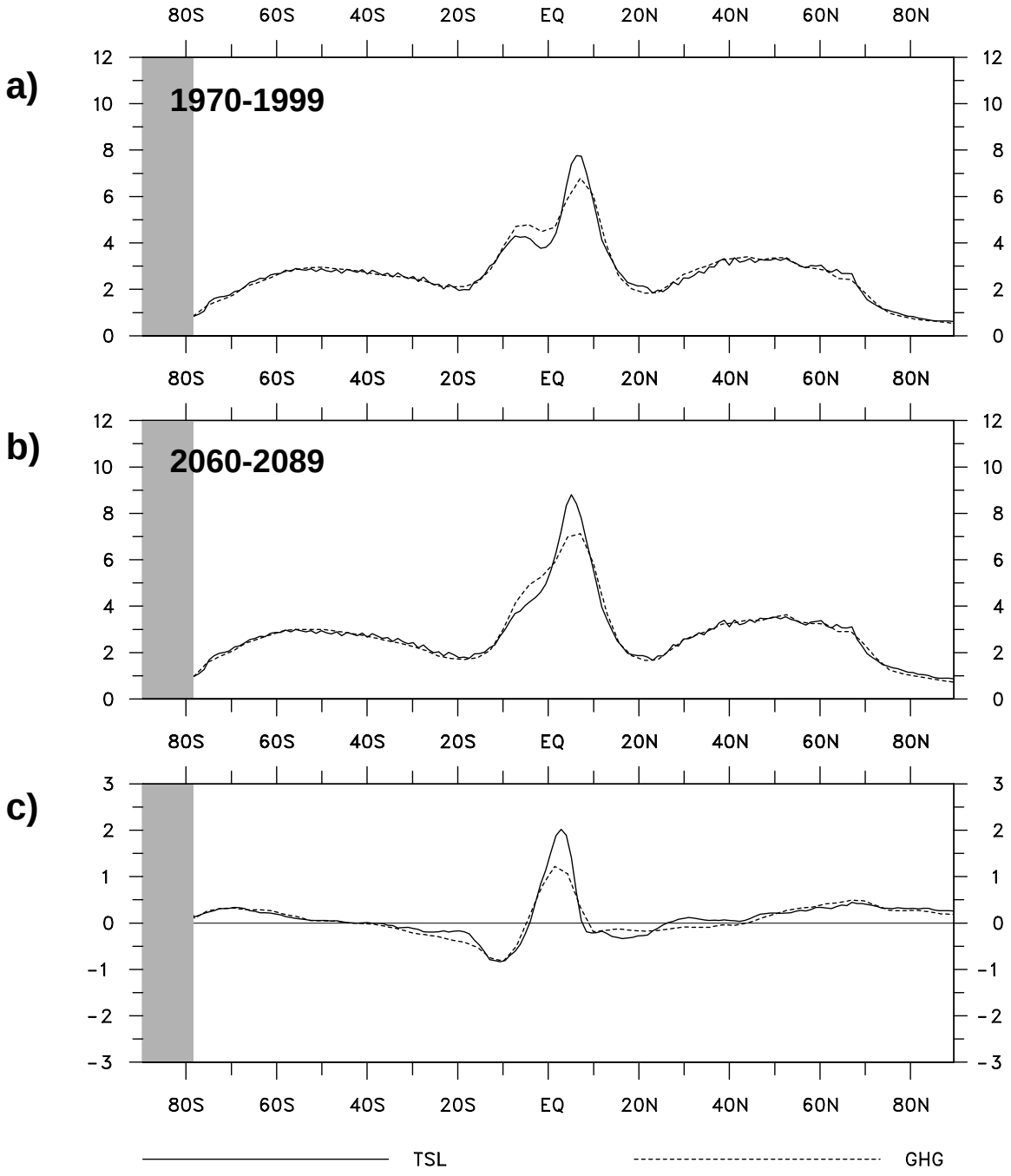

Fig. 47: As Fig. 40, put for daily precipitation. Units are [mm/day].

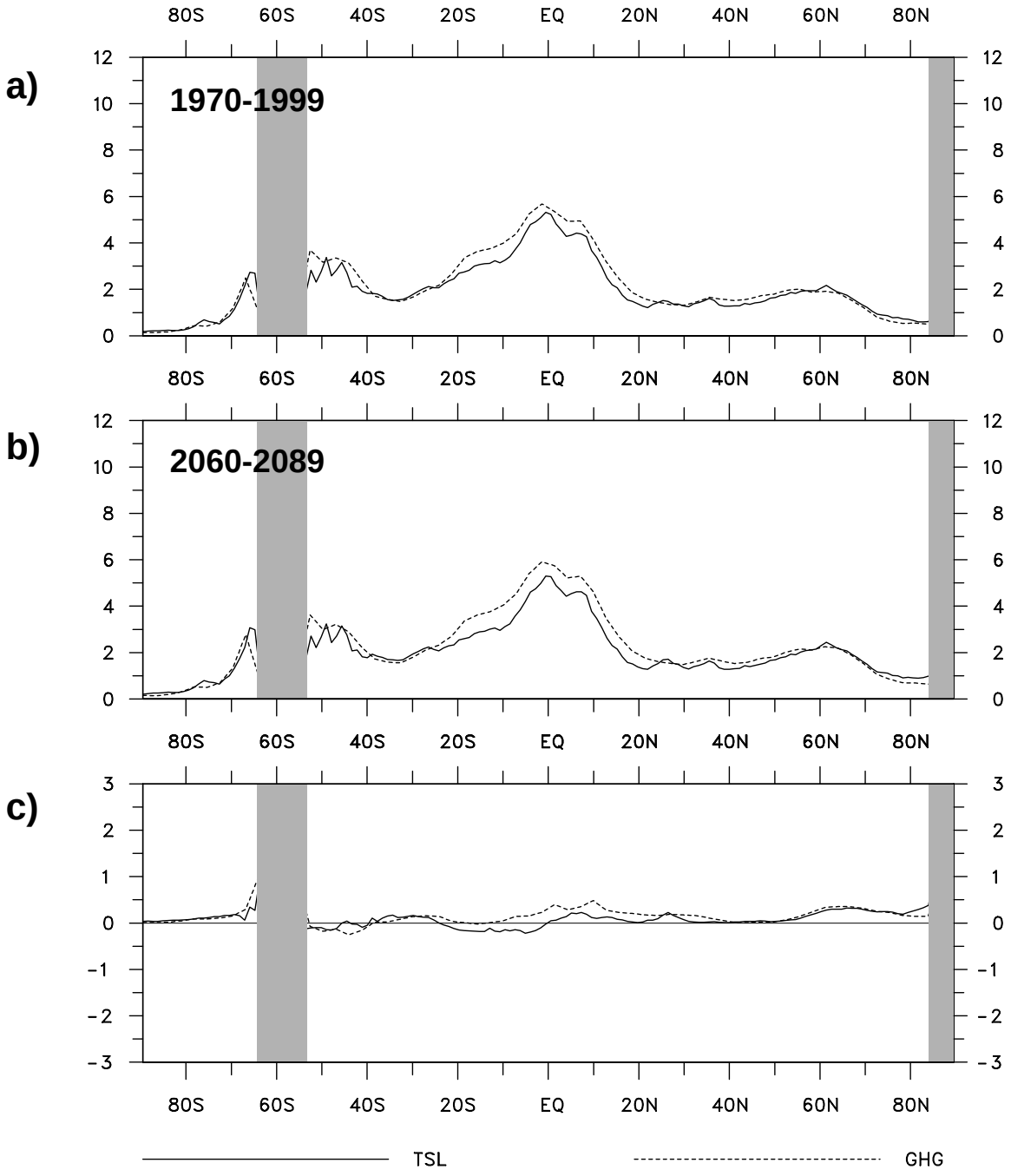

Fig. 48: As Fig. 46, put for precipitation. Units are [mm/day].

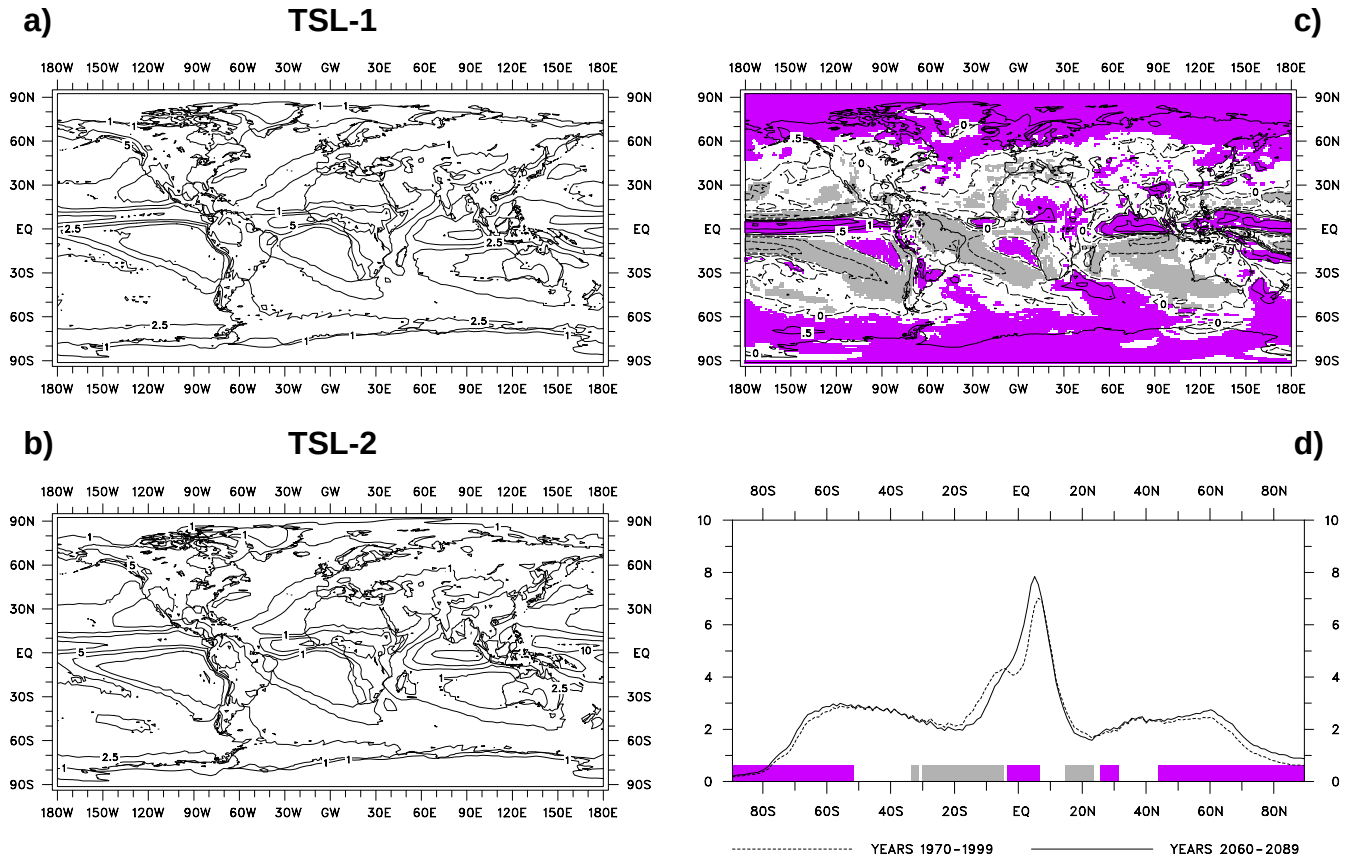

Fig. 49: As Fig. 15, but for the annual mean daily precipitation. Units are [mm/day]. The contour lines shown are at 1, 2.5, 5, 10, 15, 20 etc. mm/day (a, b) and at 0, ±0.5, ±1, ±2.5, ±5, ±10, ±20 etc. mm/day (c), respectively.

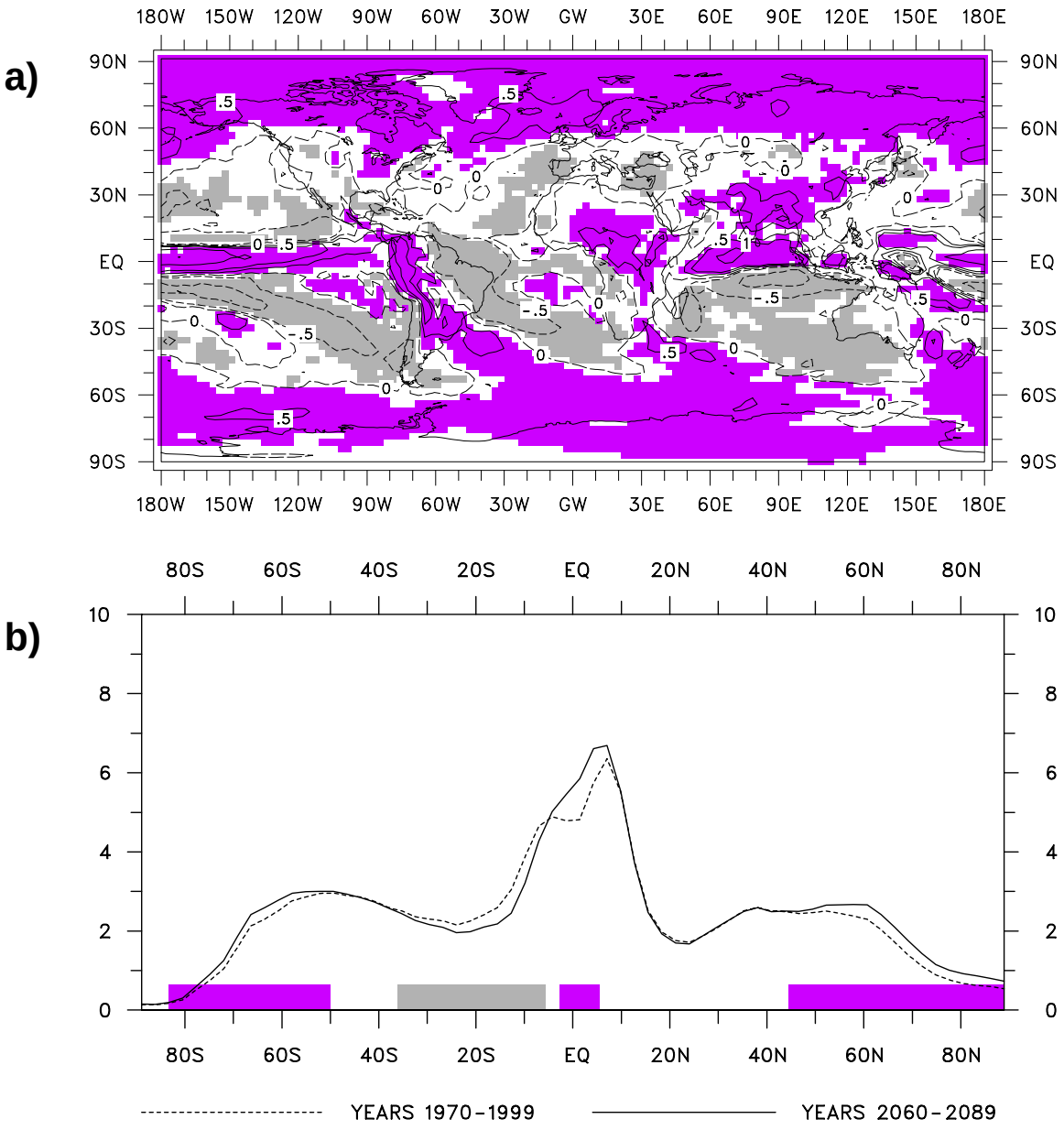

Fig. 50: As Figs. 49c, d, but for GHG.

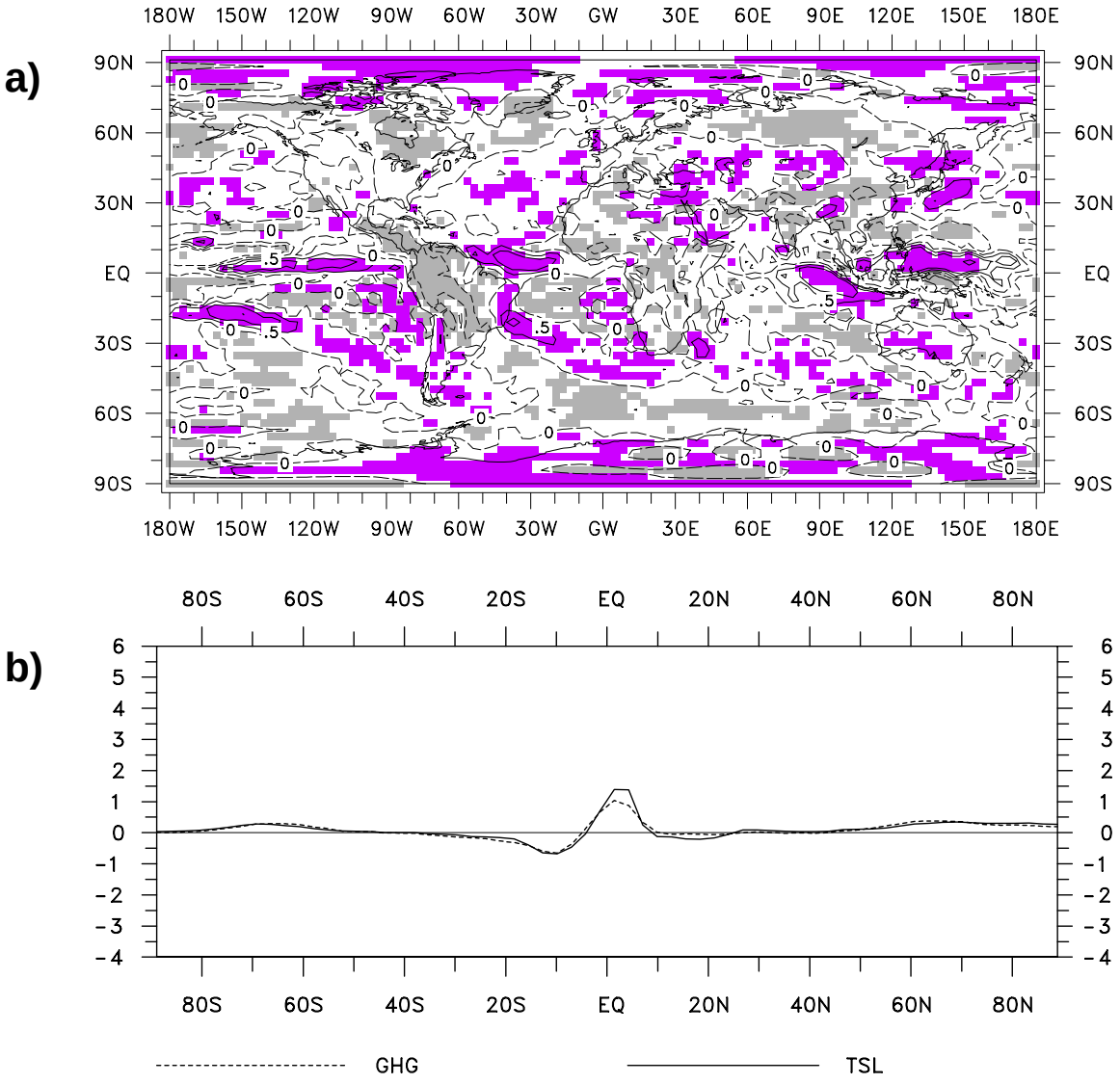

Fig. 51: As Fig. 18, but for the annual mean daily precipitation. Units are [mm/day]. The contour lines shown are at 0, ±0.5, ±1, ±2.5, ±5, ±10, ±20 etc. mm/day.

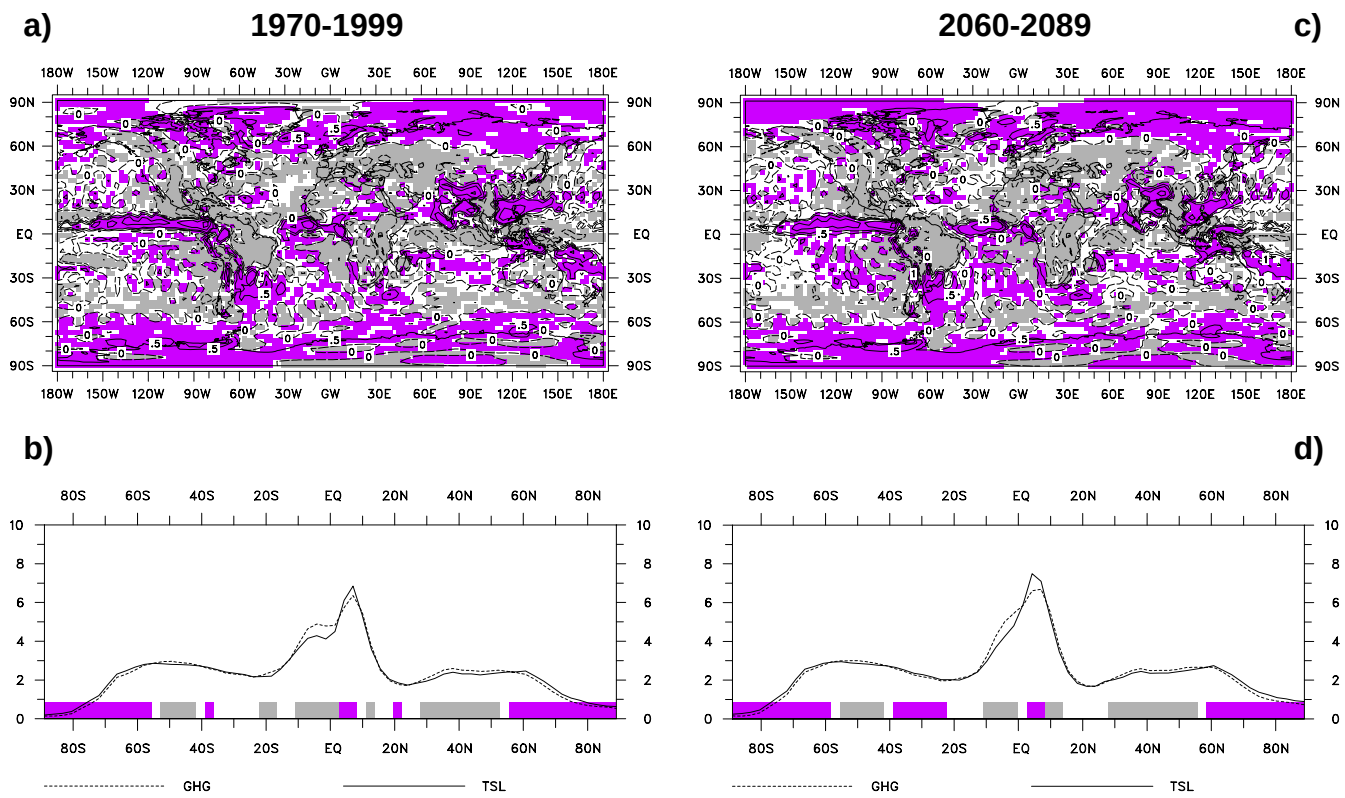

Fig. 52: As Fig. 17, but for the annual mean daily precipitation. Units are [mm/day]. The contour lines shown are at 0, ±0.5, ±1, ±2.5, ±5, ±10, ±20 etc. mm/day.

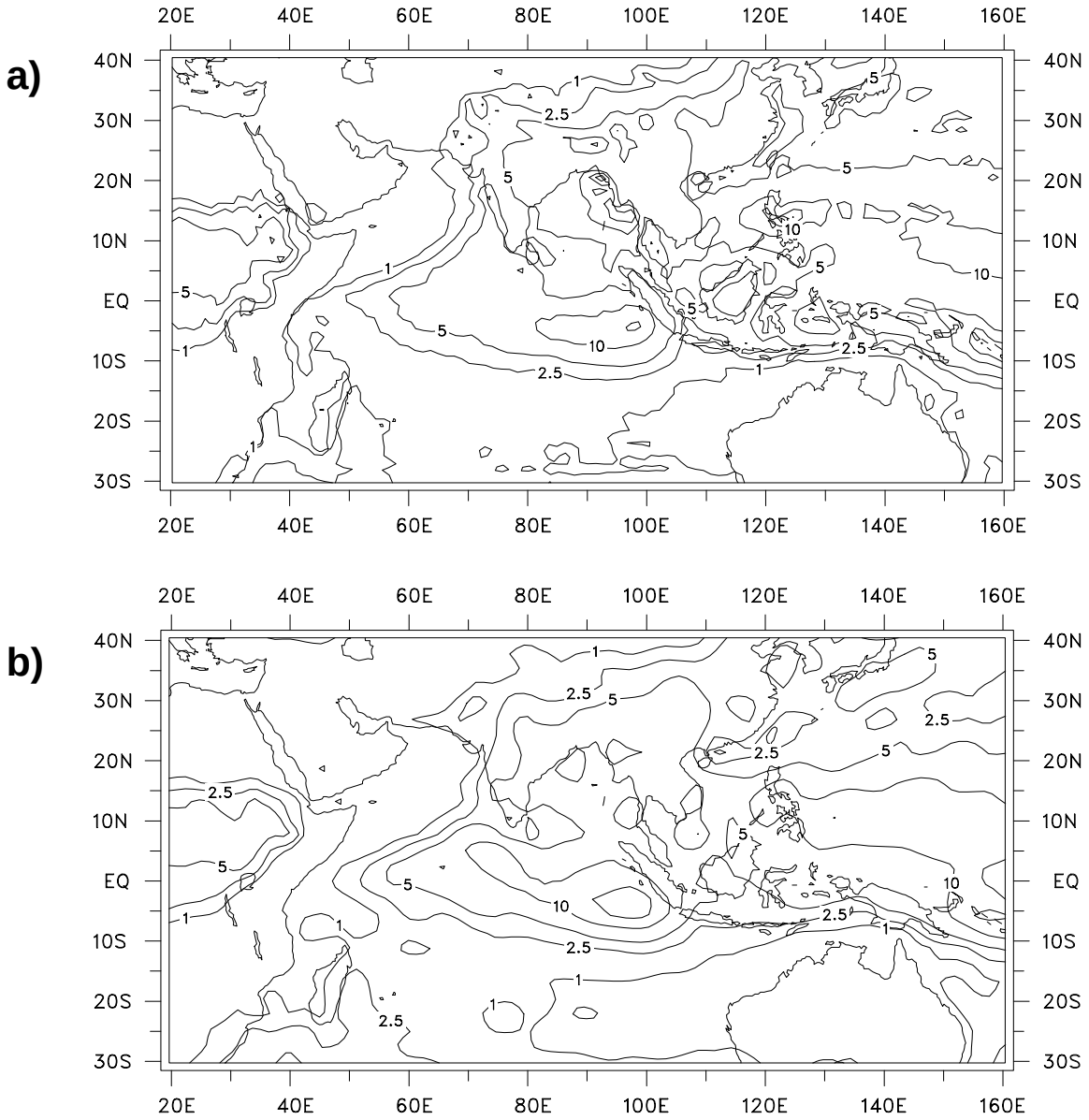

Fig. 53: Seasonal mean (June, July, August and September) daily precipitation for TSL-1 (a) and GHG-1 (b). Units are [mm/day]. The contour lines shown are at 1, 2.5, 5, 10, 15, 20 etc. mm/day.

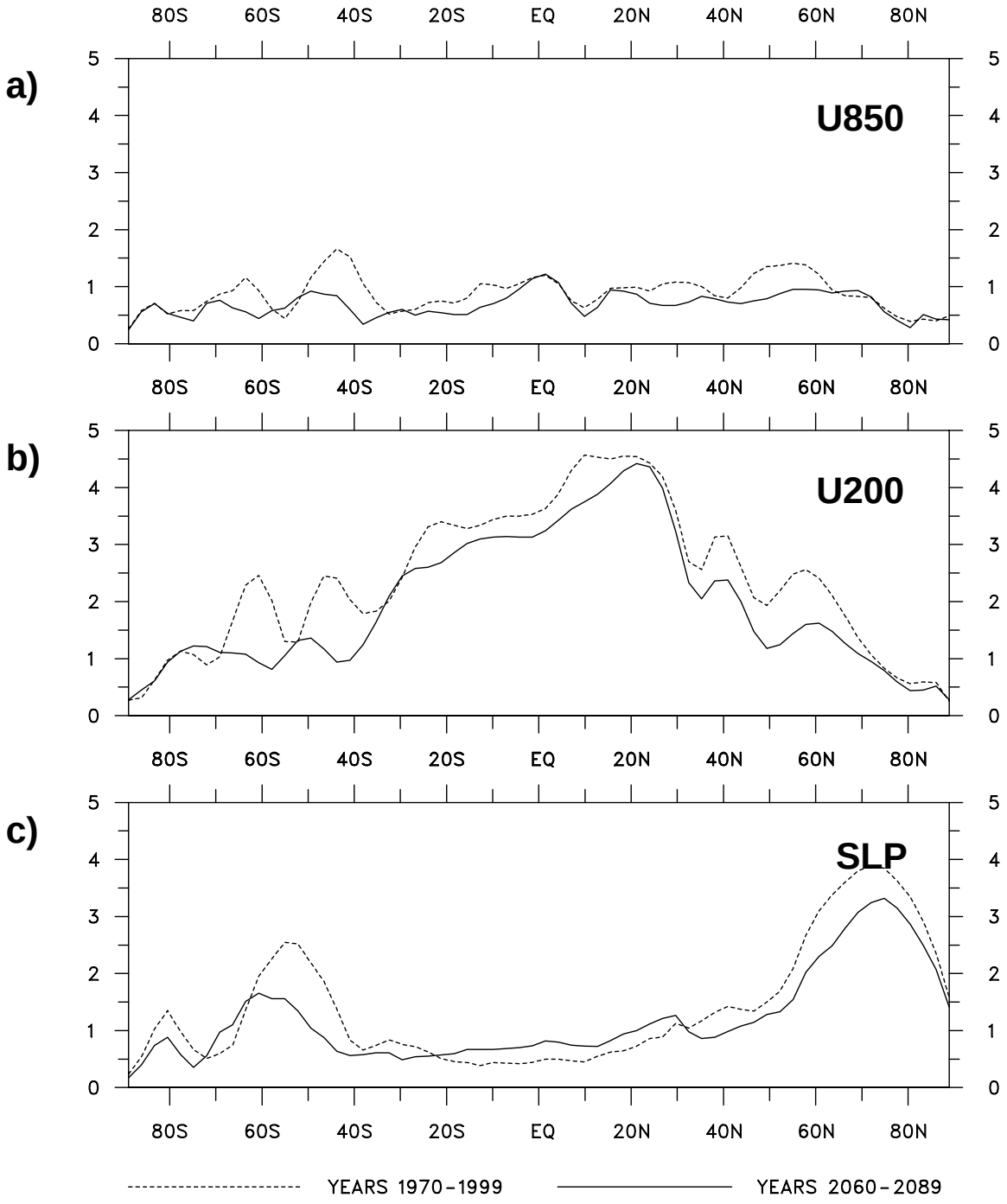

Fig. 55: As Fig. 54, but for the seasonal mean values of the zonal wind component at 850 and 200 hPa (a, b) and the sea-level pressure (c). Units are [m/s] (a, b) and [hPa] (c), respectively.